

First Order Methods for Geometric Optimization of Crystal Structures

Antonia Tsili¹, Matthew Dyer², Vladimir Gusev³, Piotr Krysta⁴, and Rahul Savani⁵

¹Department of Computer Science, University of Liverpool, Liverpool, UK.
a.tsili@liverpool.ac.uk.

²Department of Chemistry, University of Liverpool, Liverpool, UK.
msd30@liverpool.ac.uk.

³Department of Computer Science, University of Liverpool, Liverpool, UK.
vladimir.gusev@liverpool.ac.uk.

⁴Department of Computer Science, University of Liverpool, Liverpool, UK.
pkrysta@liverpool.ac.uk.

⁵Department of Computer Science, University of Liverpool, Liverpool, UK.
rahul.savani@liverpool.ac.uk.

December 20, 2023

Abstract

The geometric optimisation of crystal structures is a procedure widely used in Chemistry that changes the geometrical placement of the particles inside a structure. It is called structural relaxation and constitutes a local minimization problem with a non-convex objective function whose domain complexity increases along with the number of particles involved. In this work we study the performance of the two most popular first order optimisation methods, Gradient Descent and Conjugate Gradient, in structural relaxation. The respective pseudocodes can be found in Section 6. Although frequently employed, there is a lack of their study in this context from an algorithmic point of view. In order to accurately define the problem, we provide a thorough derivation of all necessary formulae related to the crystal structure energy function and the function's differentiation. We run each algorithm in combination with a constant step size, which provides a benchmark for the methods' analysis and direct comparison. We also design dynamic step size rules and study how these improve the two algorithms' performance. Our results show that there is a trade-off between convergence rate and the possibility of an experiment to succeed, hence we construct a function to assign utility to each method based on our respective preference. The function is built according to a recently introduced model of preference indication concerning algorithms with deadline and their run time. Finally, building on all our insights from the experimental results, we provide algorithmic recipes that best correspond to each of the presented preferences and select one recipe as the optimal for equally weighted preferences.

Keywords: continuous optimisation, local minimum, gradient methods, structural relaxation, crystal structure prediction.

1 Introduction

Crystal structures and their properties play an important role in understanding our world. The study of their properties and structure is a major component of materials discovery, whose applications impact all aspects of life. Crystal structures are periodic formations, meaning they can be represented as tilings expanding towards all 3 dimensions of Euclidean space. Since each tile is identical to the rest, it suffices to define one “central” tile to which changes are applied, so as to amend the whole structure. Each such tile is called a unit cell and can be represented by a parallelepiped. The unit cell comprises an arrangement of ions which determines the properties of the crystal and, given the ions’ number and element type, we seek to find their optimal geometrical placement in the \mathbb{R}^3 space spanned by the unit cell. This is a hard optimization problem [30]. In fact, it is a minimization problem of a function Φ with $3N+9$ variables, when N is the number of the ions in the unit cell and Φ is the objective function. We search for the function’s approximate local minimum, which corresponds to bringing the crystal to an energy equilibrium. In practice this is achieved by procedures such as heat application, hence, this geometric optimisation is also called structural relaxation in a Chemistry context and constitutes a frequently employed procedure with many applications in Computational Chemistry. For example, it is a particularly important part of Crystal Structure Prediction, for which it can take up to 90% of the computation time in experiments. The problem of geometric optimisation of crystal structures can be defined as

$$\begin{aligned} \min \Phi(x) \\ x = (r_1, r_2, \dots, r_N, l_1, l_2, l_3), \\ r_i, l_\lambda \in \mathbb{R}^3, \quad i \in [N], \lambda \in \{1, 2, 3\} \text{ s.t. } r_{ij} > 0 \text{ where } r_{i,j} = \|r_i - r_j\| \end{aligned} \quad (\text{P})$$

in which r_i denotes the position of ion i , N is the number of the ions in a unit cell and l_λ , denotes a lattice vector, as illustrated in Figure (1). We call x a minimiser of Φ when $g(x) < \epsilon$ for some small $\epsilon > 0$, in which g is the average component value of the gradient norm $\|\nabla\Phi\|$.

Φ is a nonlinear, non-convex function with a complicated domain called Potential Energy Surface (PES). The complexity of PES increases along with the number of ions N included in the calculation, as the number of local minima also increases. Φ is locally C^2 -smooth for $r_{i,j} > 0$ but is not continuous in areas where ions i, j are separated by a pairwise distance approaching 0 Angstroms. We study the application of two standard unconstrained continuous optimization algorithms, Gradient Descent and Conjugate Gradient, in finding an approximate the local minimum of the energy potential function Φ through structural relaxation. For our experiments we use structures that include ions of Sr, Ti and O randomly placed in the unit cell, so that the expected minimum of the function is represented by the structure $\text{Sr}_3\text{Ti}_3\text{O}_9$, a commonly used crystal for benchmarking in Crystal Structure Prediction. In spite of the fact that the mentioned algorithms are widely employed, they are not systematically optimised in this context and parameter configurations such as the choice of step size are kept on default. We assume that the minimization path remains in a feasible area where the pairwise distance is a positive number. However, there can be cases for which the discontinuity is approached – this is called Buckingham catastrophe. Our work shows that the optimization process can be correspondingly adapted to reach the minimiser of Φ without falling into such a case. However, there is a trade-off between a method’s robustness and convergence speed.

In addition to the above, the simplest forms of the energy potential model create further issues. In our case, Φ is a multiple summation over all pairs of ions i, j . This summation can be conditionally convergent depending on the order of the summands. Furthermore, since Φ represents interactions between particles in some neighbourhood, more pairs need to be added to the summation that account for the interactions with atoms outside the border of the unit cell. As a consequence, discontinuities can be created related to the terms close to this border, owing to the abrupt exclusion of further summands that keeps the sum finite. We tackle these by using some mathematical techniques widely known in bibliography to bring about convenient properties for Φ .

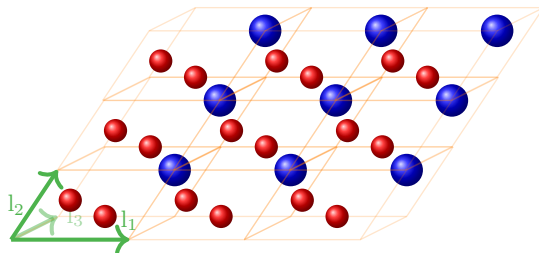


Figure 1: A mock representation of a crystal comprising ions of two kinds of elements (red and blue) in the 3-dimensional Euclidean space. The green arrows represent the lattice vectors and all ions’ positions can be represented as their linear combination.

Our contributions. In this paper we investigate the derivation of the energy function Φ and the forces $-\nabla\Phi$ and present their most numerically robust form. The energy Φ is a potentially infinite summation, therefore it is crucial in which way it is calculated and in which order the terms are summed up. We implement the energy and forces and systematically design a set of experiments to test two popular first order local optimization algorithms frequently used by Chemists, Gradient Descent and Conjugate Gradient, using our implementation. More specifically:

- We carefully construct the energy potential model and present the analytical process of evaluating the energy function. Towards this goal, we prove some useful propositions, critical for the Computational Chemistry related background theory. They can be found in Section 4. We propose a new geometric method called Inflated Cell Truncation in Subsection 4.3. This new method is also a part of the energy computation.
- We provide a thorough derivation of the forces, the energy function’s first derivatives, with formal proofs and we explain what are the parameters with respect to which they are evaluated. Detailed description of the differentiation process can be found in Section 5.
- All derived formulae and the two algorithms have been implemented with our Python/Cython software hosted in this Github repository (<https://github.com/lrcfmd/veltiCRYS>).
- We conduct extensive experiments to formally compare the two algorithms in the setting of structural relaxation. The setting of the experiments is presented in Section 7.
- To the best of our knowledge, this is the first paper about such a systematic study of the algorithms applied to the problem in question. As such, we provide a performance benchmark for first order methods using each algorithm with constant step in Section 8.
- We improve the algorithms’ benchmarked performance by designing scheduling rules for the step size in Section 9.
- We provide a thorough analysis of the experiments and a tool to formally evaluate the algorithms’ suitability to our preferences in Section 9. This tool is a utility function that can be used to decide which of the two algorithms will be more useful in certain applications.

The road-map of the document is as follows. In Section 2 we discuss previous work related to energy calculation and minimisation realised with the first order algorithms that we study. In Section 3 we introduce basic concepts and definitions related to Crystal Structure Prediction and Crystallography. We, then, describe the energy model that forms our objective function and present our formulae derivation in Sections 4 and 5. In Section 6 we introduce the first order algorithms that we use and that we compare. We, next, present our experimentation process with details in the implementation, the results and their analysis in Section 7, where our utility tool is also introduced following the recipe presented by Graham D. et al [18]. Finally, we elaborate on the utility scores of each method used in our experiments and state our conclusions.

2 Related Work

The calculation of the energy of crystal structures is a long studied subject that has been investigated since the first attempts to understand materials' properties. Many reports have presented different versions of the Coulomb energy potential expanded with Ewald summation [33, 43, 39, 27, 42, 43]. There are also some reports presenting the dispersion energy of interatomic potentials like Buckingham [23]. Following the example of GULP [17], we combine both Buckingham and Coulomb potentials in one document, as well as their derivation details. We also elaborate on the derivation of the forces, the functions' first derivatives [21], and the kinds of parameters that are updated during a crystal structure relaxation, which are not straightforward. Such information can be found scattered in literature, so we attempt to gather all knowledge related to structural relaxation together.

Gradient Descent and Conjugate Gradient algorithms are no strangers to geometry optimization in Chemistry applications. Any generic geometry optimization review will give credit to these two simple algorithms in unconstrained minimization settings, as the work of Schlegel shows [37]. Publications as early as Catlow and Mackrodt's [8] study function minimisation through ion displacement and lattice deformation. The work of Payne et al. [32] describes the use of Conjugate Gradient for energy minimisation of the electronic structure but also in energy functional minimisation. Many approaches to geometry optimization have been proposed since then [3] with machine learning getting increasingly more attention [13, 5], as in any application related to Computer Science. However, there is a lack of analysis of the algorithmic aspects of the aforementioned simple first order algorithms. These are still being used today for structural relaxation [14],[31], but little analysis has been provided in this context. The recent study of Salih and Faraj [41] investigates the algorithms' performance and compares them on the basis of 3 simple nonlinear function applications. Our work extends this comparison to a much more complex setup and is focused on the efficiency of their direction selection by excluding the line search.

3 Preliminaries

For the rest of the article we refer only to optimisation problems whose goal is function minimisation. The specific objective function will be introduced in detail. Before continuing further, we will list some useful definitions and symbols that will be frequently used.

Definition 1 (Ions). *Atom with an electric charge due to the loss or gain of one or more electrons. In this work ions are presented as input and our methods are agnostic towards how the ions are created.*

Definition 2 (Unit Cell). *The smallest fundamental arrangement of the ions positions' that reflects the crystal's symmetry and structure is called unit cell. The unit cell C_n is a parallelepiped built on a set of three vectors $L = [l_1 l_2 l_3]$ such that $l_t \in \mathbb{R}^3$, $\forall t \in \{1, 2, 3\}$ and contains N positions r_1, r_2, \dots, r_N , $r_i \in \mathbb{R}^3$, $i \in [N]$, where the ions are placed. The unit cell of the crystal in Figure 1 is depicted in Figure 2.*

Definition 3 (Lattice). *Given the translation vectors $L_n = n^T L$ with $n \in \mathbb{N}$, lattice is the set $\mathcal{D}_{L_n} \subset \mathbb{R}^3$ of mathematical points that correspond to the infinitely repeated positions of ions which form the crystal structure is the lattice. The points can be defined using the lattice vectors L_n , such that $\forall r_{i_1}, r_{i_2} \in \mathcal{D}_{L_n}$ we have $r_{i_2} = r_{i_1} + n_1 l_1 + n_2 l_2 + n_3 l_3$ and n_1, n_2, n_3 are arbitrary integers.*

Definition 4 (Reciprocal Lattice). *It represents the Fourier transform of the lattice of Definition 3 (real space lattice). It is used along with the real lattice in crystallography for periodic structures. The derivation of the reciprocal lattice vectors $k = [k_1 k_2 k_3]$ is described in Table 1. The points can be defined in the same way as for the real space lattice using the vectors G_m , such that $\forall r_{i_1}, r_{i_2} \in \mathcal{D}_{G_m}$ we have $r_{i_2} = r_{i_1} + m_1 k_1 + m_2 k_2 + m_3 k_3$ and m_1, m_2, m_3 are arbitrary integers.*

Definition 5 (Potential Energy). *Potential energy, henceforth Φ , is the energy that exists on account of the ions' positions. It is the energy stored in a structure as a result of the relative positions $r_i \in \mathbb{R}^3$, $i \in [N]$ of the ions and the forces that one exerts to another and form mutual chemical bonds.*

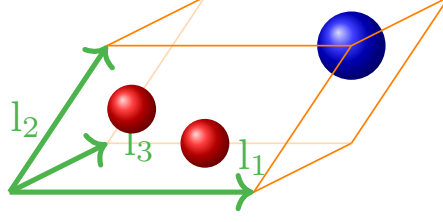


Figure 2: The unit cell of the crystal structure depicted in Figure 1. The vectors l_1, l_2 and l_3 represent the 3 lattice vectors.

The following abbreviations can be found throughout this document:

r_i	vector position of ion i in \mathbb{R}^3
R	matrix of ion positions in $\mathbb{R}^{3 \times N}$
L	matrix of lattice vectors in $\mathbb{R}^{3 \times 3}$
L_n	$n^T L = n_1 l_1 + n_2 l_2 + n_3 l_3$ in \mathbb{R}^3 , $n = (n_1, n_2, n_3)$, $n \in \mathbb{Z}^3$
$r_{i,j,n}$	$r_i + L_n - r_j$, $i, j \in [N]$
u_α	component α (Greek letter) of vector u with $\alpha \in \{x, y, z\}$
k_t	$2\pi \cdot (l_{t \bmod 3+1} \times l_{(t+1) \bmod 3+1}) / \langle l_t, l_{(t \bmod 3+1} \times l_{(t+1) \bmod 3+1} \rangle$, $t \in \{1, 2, 3\}$
G_m	$m^T k = m_1 k_1 + m_2 k_2 + m_3 k_3$ in \mathbb{R}^3 , $m = (m_1, m_2, m_3)$, $m \in \mathbb{Z}^3$
k_e	electrostatic constant $1/(4\pi\epsilon_0)$
$\sum_{i,j}^{N'} \sum_n$	$\sum_i^N \sum_j^N \sum_n$ for all $n = (n_1, n_2, n_3)$ except $n = (0, 0, 0)$ when $i = j$, $i, j \in [N]$

Table 1: Notation

We will now proceed to describe Problem P in more detail, starting with information and justifications on the reason why each energy function was selected and some intuition on its implementation.

4 Objective Function - Energy

Since our research is based on ionic structures, we model our case using the Buckingham-Coulomb energy potential. The total energy comprises two lattice summation schemes over a hypothetical infinite structure built by repeating the unit cell \mathcal{C}_n in all dimensions of the Euclidean space. The first scheme, the Coulomb part, addresses the distant electrostatic interaction of monopole to monopole and the second, the Buckingham part, accounts for Pauli repulsion energy and van der Waals energy between two atoms as a function of the interatomic distance between them. The two terms of each Buckingham summand represent repulsion and attraction respectively:

$$\Phi_{Coul}(R, L) = \frac{k_e}{2} \sum_{i,j}^{N'} \sum_{n \in \mathcal{N}} \frac{q_i q_j}{||r_{i,j,n}||} \quad (1)$$

$$\Phi_{Buck}(R, L) = \frac{1}{2} \sum_{i,j}^{N'} \sum_{n \in \mathcal{N}} A \exp\left(-\frac{||r_{i,j,n}||}{\rho}\right) - \frac{C}{||r_{i,j,n}||^6} \quad (2)$$

$$\Phi = \Phi_{Coul} + \Phi_{Buck} \quad (3)$$

The independent variables of both functions are the ion positions $R = (r_1, r_2, \dots, r_N)$ and the lattice vectors $L = (l_1, l_2, l_3)$. The Buckingham constants A, C and ρ have been experimentally determined in literature [10] and differ among the combination of elements in the atoms pairs. Both energy sums run over all distances $||r_{i,j}|| = ||r_i - r_j||$ of pairs $i, j \in [N]$ with N' symbolising the exclusion $i \neq j$ if and only if $n = (0, 0, 0)$. The set \mathcal{N} is defined using the Inflated Cell Truncation method described in the third part of this Section.

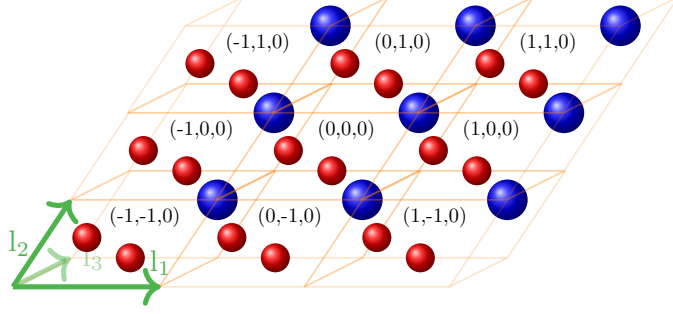


Figure 3: Central unit cell $\mathcal{C}_{(0,0,0)}$ surrounded by 8 unit cell images denoted by $(-1, 1, 0)$, $(1, 0, 0)$, $(1, 1, 0)$, $(-1, 0, 0)$, $(1, 0, 0)$, $(-1, -1, 0)$, $(0, -1, 0)$ and $(1, -1, 0)$.

Our energy calculations involve particles subjected to periodic boundary conditions (PBCs), so that each ion i of a central reference unit cell $\mathcal{C}_{(0,0,0)}$ interacts with the neighbouring ions residing in surrounding images of $\mathcal{C}_{(0,0,0)}$, as in Figure 3. Each ion i is separated from images of ion j by the pairwise distances $\|r_{i,j,n}\| = \|r_i + L_n - r_j\|$, where the vector L_n creates the periodic translations of each ion j of the central unit cell.

As such, each sum over all pairs i, j also runs through all triplets $n = (n_1, n_2, n_3)$, $n_1, n_2, n_3 \in \mathbb{Z} \cup \{0\}$ which correspond to the central reference unit cell $\mathcal{C}_{(0,0,0)}$ and the surrounding images \mathcal{C}_n denoted by $n \neq (0, 0, 0)$. The convergence of the sum over all pairwise interactions is strongly affected by the selection of interacting images included in the set of n triplets \mathcal{N} , but also the order of the summation in Equations (1),(2) [1]. In this form, Φ_{Coul} is conditionally convergent; the order of the terms in the summation determines whether it will finally converge. Moreover, the need for finite interaction terms imposes the use of methods which abruptly terminate the summation up until some designated distance away from the ions of the central unit cell. This term exclusion causes precision loss problems, discontinuity of limits, such as the derivatives, and others [15], [22] [40]. For this reason, we instead expand Φ_{Coul} using the Ewald summation.

4.1 Ewald Summation

As already discussed, the Coulomb potential in its original form is evaluated directly in real space and is conditionally convergent, the conditions being dependent on the order of the summation. When employing the Ewald method, our target is to split the summation into short and long range contributions, so as to treat each part differently and arrive to two rapidly and absolutely convergent summation parts. For the rest of this paper, let $(\mathcal{C}_n : L_n, R)$ be crystal structure with unit cell \mathcal{C}_n described by a set of real lattice vectors $L_n, n \in \mathbb{R}^3$, a set of reciprocal lattice vectors $G_m, m \in \mathbb{R}^3$ and with ion positions R .

Proposition 1. *Expanding with Ewald summation, the short range interactions of the Coulomb potential summation are calculated as:*

$$\Phi_{Coul}^S(R, L) = \frac{k_e}{2} \sum_n \sum_{i=1}^N \sum_{j=1}^{N'} \frac{q_i q_j}{\|r_i + L_n - r_j\|} \operatorname{erfc}(\alpha \|r_i + L_n - r_j\|) \quad (4)$$

Proposition 2. *Expanding with Ewald summation, the long range interactions of the Coulomb potential summation are calculated as:*

$$\Phi_{Coul}^L(R, L) = \frac{k_e}{2} \sum_n \sum_{i=1}^N \sum_{j=1}^N \frac{k_e}{2} \frac{q_i q_j}{\|r_i + L_n - r_j\|} \operatorname{erf}\left(\frac{\|r_i + L_n - r_j\|}{\sqrt{2}\sigma}\right) \quad (5)$$

The sum of $\Phi_{Coul}^S + \Phi_{Coul}^L$ gives the total value of electrostatic energy of the crystal structure. We will next expand the long range interactions part Φ_{Coul}^L even further, so as to arrive to an equally fast convergent scheme as the quickly decreasing complementary error function $\operatorname{erfc}(\cdot)$.

4.2 Long Range Term

In the following, we have exploited the periodicity of the terms of the energy summation to derive an expression for the long range ion interactions that converges fast. We also employ techniques to dispose of imaginary terms. For that purpose, we have resorted to a Fourier series expansion and symmetry conventions.

Proposition 3. *The form of the reciprocal term of the Coulomb potential with fast convergence is:*

$$\Phi_{Coul}^L(r, L) = \frac{4\pi}{|V||G_m|^2} \exp\left(-\frac{\|G_m\|^2}{4\alpha^2}\right) \exp(iG_m r) \quad (6)$$

Proposition 4. *The fast convergent Coulomb potential for long range interactions in a crystal structure is given by the function*

$$\Phi_{Coul}^L(r, L) = \frac{2\pi k_e}{V\|G_m\|^2} \sum_{G_m \neq 0} \sum_{i=1}^N \sum_{j=1}^N q_i q_j \exp\left(-\frac{\|G_m\|^2}{4\alpha^2}\right) \cos(G_m r) \quad (7)$$

Proposition 5. *The convergent form of its Coulomb energy potential is formed by the following equations:*

$$\begin{aligned} \Phi_{Coul}^S(r, L) &= k_e \sum_{i,j}^{N'} \sum_n q_i q_j \frac{\text{erfc}(\alpha \|r_{i,j,n}\|)}{2\|r_{i,j,n}\|} \\ \Phi_{Coul}^L(r, L) &= k_e \sum_{i,j}^N \sum_{m \neq 0} q_i q_j \frac{2\pi \cdot \exp\left(-\frac{G_m^2}{4\alpha^2}\right) \cdot \cos(G_m \cdot r_{i,j})}{VG_m^2} \\ \Phi_{Coul}^{self}(r, L) &= -k_e \sum_{i=1}^N q_i^2 \frac{\alpha}{\sqrt{\pi}} \end{aligned} \quad (8)$$

so that

$$\Phi_{Coul} = \Phi_{Coul}^S + \Phi_{Coul}^L + \Phi_{Coul}^{self} \quad (9)$$

It is important to notice that for the long range term Φ_{Coul}^L the summation includes the pair $i = j$ for $n = 0$ and a new set of triplets $m \in \mathcal{M}$ that correspond to the lattice vectors of unit cell images in reciprocal space, so that $G = (k_1, k_2, k_3)$ are the reciprocal vectors and the sum is over G_m . The summation cost is owed to the number N of ions, the set of real \mathcal{N} and reciprocal \mathcal{M} vectors, as well as the $\alpha = 1/\sqrt{2}\sigma$ parameter, and reaches a complexity of $O(N^{\frac{3}{2}})$ [27].

4.3 Inflated Cell Truncation

There are theoretical and practical issues that dictate the exclusion of energy terms which stand for far too long range interactions. On the one hand, there is a balance to maintain between short range and distant energy contributions, as the interaction terms' number increases along with the distance from a certain ion. This is mitigated owing to the slow decay of the functions that emerge from the Ewald expansion. On the other hand, implementation issues call for finite sums, hence, one of the decisions to be made regarding the energy model concerns the possible values of each of the integers $n_1, n_2, n_3, m_1, m_2, m_3$. These numbers declare which neighbouring copies of the unit cell are to be taken into account in the energy and derivatives evaluation. In other words, they define how many terms are to be added into the summation of the energy and forces, thus, affect greatly the convergence of these numbers. The starting point to construct the set of these numbers is the cutoff [24] r_{off} , which reflects the maximum distance $\|r_{i,j,n}\|$ in Angstroms that should separate two ions i, j . We set the cutoff for real r_{off}^S and reciprocal space r_{off}^L according Catlow's formulae [24], which aim to minimise the number of summands to achieve an accuracy A:

$$\alpha = \frac{N^{1/6} \sqrt{\pi}}{V^{1/3}}, \quad r_{off}^S = \frac{\sqrt{-\log(A)}}{\alpha}, \quad r_{off}^L = 2\alpha \sqrt{-\log(A)} \quad (10)$$

where V is the volume of one unit cell. Another thing that affects the result of the summation is the symmetry of the terms of interaction that would be included. More specifically, it would not be realistic to select neighbouring cells in a way that ultimately approaches the shape of a tube.

Traditionally, the simplest method used in order to keep the energy summation finite is the truncation method [28]. According to this method, all summands are multiplied by a function $\psi(||r_{i,j,n}||)$

$$\psi(||r_{i,j,n}||) = \begin{cases} 1, & ||r_{i,j,n}|| < r_{off} \\ 0, & ||r_{i,j,n}|| \geq r_{off} \end{cases} \quad (11)$$

that allows only ions j within the range of some ion i to be studied. Following this scheme, various ways of creating neighbour lists that store the neighbours within range for each atom in the central unit cell have been developed. One of the most widely used algorithms include the Verlet Neighbour list [16], which maintains the array of the neighbours of the atom within a fixed cutoff, and the Linked-Cell method [6], which creates a list for each tile in a divided supercell. However, the first method requires a potentially large memory allocation and both methods suffer from a time-consuming bookkeeping, especially for our constant changing setting of the lattice. Other more modern approaches include that of Mason [29], who focuses on the storing power of a bitmap, so that the neighbours are represented in memory in a way that enables locality information storage, and that of Zhang et al. [44], whose work revolves around the consideration of potential neighbours near the margin of the ion's sphere of interaction. These techniques, however, are designed to facilitate Molecular Dynamics processes, whereas in our case we can fully exploit the symmetry of the ionic crystal.

For this work, we provided a geometric solution that makes use of the properties of the unit cell called *Inflated Cell Truncation 1*. Let S be a sphere (O, r) where O is the centre of gravity of the central unit cell $\mathcal{C}_{(0,0,0)}$ and r is a radius with length equal to the cutoff value $r = r_{off}$. We assume that

$$r_{off} \geq \max\{||l_1||, ||l_2||, ||l_3||\} \quad (12)$$

meaning that there is at least one whole unit cell in S . We, then, identify each plane P to which a face of the unit cell parallelepiped belongs and we assume the corresponding translations P' of the planes so that P' is parallel to P and tangent to S . Because of symmetry, we only need to move the 3 adjacent planes defined by l_1, l_2, l_3 and apply the opposite movements to the rest. Then, we compute the length of the translation vector t which performs $P' = P + t$ and enumerate all images of unit cells that are encased in the plane translations P' .

Theorem 1. *Let \mathcal{C}_n be the parallelepiped of a unit cell and A a face of \mathcal{C}_n with v the height that corresponds to A . The vector t that translates the plane P of \mathcal{C}_n to a parallel plane P' tangent to (O, r_{off}) has length $||t|| = r_{off} - \frac{v}{2}$ and is parallel to the normal $N_{P'}$ of plane P' .*

Corollary 1. *The distance between P and P' can fit $\frac{||t||}{||v||} + 1/2$ many unit cell images.*

The previous results reveal that, in order to include a reasonable number of neighbours for the ions of the central unit cell $\mathcal{C}_{(0,0,0)}$, we can find the translation vector t for each face and separate it into a number of segments equal in length to half the height of the parallelepiped parallel to the normal of that face. In the following pseudocode we present the procedure of *InflatedCellTruncation1* which utilises these results to enumerate the images of unit cells that we include in our energy summation. For our setting, we have included whole unit cell images instead of excluding all terms outside the cutoff sphere (O, r_{off}) .

Algorithm 1 Algorithm for the procedure that computes the triplets n and m for energy related calculations

Input the transpose of the matrix of lattice vectors L^T , the cutoff r_{off}

Output an array of triplets n_1, n_2, \dots, n_{c-1} with $n_i = (n_{i,1}, n_{i,2}, n_{i,3})$

```

1: procedure INFLATEDCELLTRUNCATION( $L^T, r_{off}$ )
2:    $V \leftarrow \det(L^T)$ 
3:    $O \leftarrow \langle [0.5, 0.5, 0.5], L^T \rangle$ 
4:    $v_0, v_1, v_2 \leftarrow \text{Normals}(l_1, l_2, l_3)$ 
5:   for  $i = 0, 1, 2$  do
6:      $v \leftarrow V / \|v_i\|$ 
7:      $t_{(i+2)\%3} \leftarrow \lceil (r_{off} - \frac{v}{2}) / v \rceil$ 
8:    $c \leftarrow (2t_0 + 1) \cdot (2t_1 + 1) \cdot (2t_2 + 1) - 1$ 
9:   for  $(s_0, s_1, s_2) \leftarrow \text{enumerate}(2t_0 + 1, 2t_1 + 1, 2t_2 + 1)$  do
10:    if  $(s_0, s_1, s_2) \neq (t_0, t_1, t_2)$  then
11:       $n_i \leftarrow (s_0, s_1, s_2) - t$ 
12:   return  $n_1, \dots, n_{c-1}$ 

```

In the above algorithm the function Normals in line 4 calculates the respective normal vectors for each of the 3 faces defined by l_1, l_2, l_3 . We only need 3 normals as the symmetrical operations are performed in the next lines for the rest of the faces. This algorithm is used both for the real cutoff with triplets n , but also the cutoff in reciprocal space with triplets m .

4.4 Buckingham Catastrophe

One of the limitations of the widely used Buckingham-Coulomb energy potential is called Buckingham catastrophe [2] and is a hard situation to recover from for minimisation techniques. It refers to the Buckingham potential, whose form causes the Buckingham-Coulomb model to have neighbourhoods of deep wells that mathematically tend to negative infinity, as pictured in Figure 4.

Intuitively, in terms of chemical components, a small distance between ions can cause the attraction $\|r_{i,j,n}\|^{-6}$ term of Equation (2) to overpower the repulsion term and continuously push the ions together until they start to merge. In terms of the mathematical approach, the $\|r_{i,j,n}\|^{-6}$ term diverges as $\|r_{i,j,n}\|^6 \rightarrow 0$ and a minimisation algorithm sets out to reach the infimum of Φ in a neighbourhood of the potential energy surface that stretches to $-\infty$. Obviously, this creates an infinite loop that can only be salvaged by creating an iteration deadline, or placing constraints to Problem P. For our experiments we examined the possibility of arriving to such a catastrophe using unconstrained optimisation and limiting the running time by iteration number.

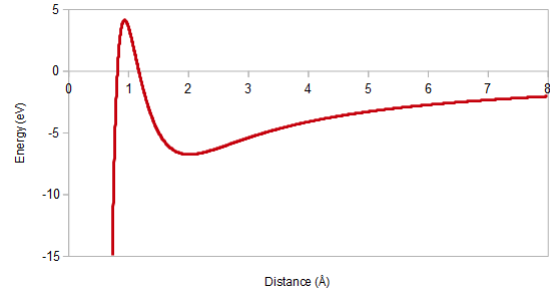


Figure 4: Example of Coulomb-Buckingham potential of interaction between oppositely charged ions¹.

Equation (2) suggests that a cutoff radius should also be used for a finite summation of the Buckingham terms as explained in Paragraph 4.3. Our empirical results showed that, when the cutoff is not large enough, the abrupt exclusion of Buckingham terms can cause discontinuities of the gradient and steep slopes on the PES. For this reason, we revisit the problematic dispersion term $\|r_{i,j,n}\|^{-6}$, which is the prevailing term of a series with larger powers $\|r_{i,j,n}\|^{-7}, \|r_{i,j,n}\|^{-8}$ and so on [7]. The dispersion term is expanded using the Ewald method as explained in Paragraph 4.1 and the summation follows the methods found in Paragraph 4.2 – due to the symmetry in the periodicity of the unit cell – so that the final form of the Buckingham potential that we use is the following:

¹https://commons.wikimedia.org/wiki/File:Coulomb-Buckingham_Potential.png

Proposition 6. *The Buckingham energy potential of the structure is formed by the following equations:*

$$\begin{aligned}
\Phi_{Buck}^S(R, L) &= \sum_{i,j}^{N'} \sum_n \left[A_{ij} \exp\left(-\frac{\|r_{i,j,n}\|}{\rho}\right) - \frac{C_{ij}}{\|r_{i,j,n}\|^6} \left(1 + \alpha^2 \|r_{i,j,n}\|^2 + \frac{\alpha^4 \|r_{i,j,n}\|^4}{2}\right) \exp(-\alpha^2 \|r_{i,j,n}\|^2) \right] \\
\Phi_{Buck}^L(R, L) &= -\frac{1}{2} \sum_{i,j}^N C_{ij} \frac{\pi^{3/2}}{12V} \sum_{G_m \neq 0} \left[\sqrt{\pi} \cdot \operatorname{erfc}\left(\frac{G_m}{2\alpha}\right) + \left(\frac{4\alpha^3}{G_m^3} - \frac{2\alpha}{G_m}\right) \exp\left(-\frac{G_m^2}{4\alpha^2}\right) \right] \cdot \cos(G_m r_{i,j}) G_m^3 \\
\Phi_{Buck}^{self}(R, L) &= \frac{1}{2} \sum_{i,j}^N \left(-\frac{C_{ij}}{3V} \pi^{3/2} \alpha^3 \right) + \sum_{i=1}^N \frac{C_{ii} \alpha^6}{12}
\end{aligned} \tag{13}$$

so that

$$\Phi_{Buck} = \Phi_{Buck}^S + \Phi_{Buck}^L + \Phi_{Buck}^{self} \tag{14}$$

The proof follows the same pattern as the proof of Proposition 5.

5 Gradient - Forces

During structural optimisation, there are two main aspects of the crystal that need to be examined in terms of changes and how these changes affect the structure energy. For this work, we have explored both aspects and we will be presenting all the necessary formulae that describe the related degrees of freedom of the crystal structure during relaxation. These equations have been rigorously derived and thoroughly tested with the implementation that accompanies this paper.

The two aspects previously referred to are the internal and external coordinates of the crystal. The internal coordinates describe relative positioning of the ions, whilst external coordinates describe the lattice formation. In order to perform energy minimisation, we use the derivatives of the energy function with respect to both kinds of parameters. Here, the internal coordinates' degrees of freedom are $3N$ and correspond to the ion position Cartesian coordinates, while the external coordinates' degrees of freedom are nine and correspond to the lattice vectors. Accordingly, in order to perform optimisation, we need two kinds of derivatives of the energy function. The first kind is pretty straightforward, since the parameters' involvement is clearly defined from the definition of the energy potential function.

The physical interpretation of the derivatives is, on the one hand, the forces that each ion exerts onto another, and, on the other hand, the forces that are transmitted along the volume of the lattice because of the action of one point in relation to the neighbouring points. More precisely, when the lattice is updated, it can happen either by changing the length of the lattice vectors, or by changing the angles between them, thus affecting the volume of the structure. We will be discussing how these changes can be modeled in a way that excludes unwanted movements, such as rigid body movements.

5.1 Internal Coordinates

In this paragraph we present the formulae related to the internal forces acting in a crystal structure, or, more precisely, the forces that act on the ion position vectors. These arise as the negative of the gradient of the energy function Φ , whose components are the derivatives $\frac{\partial \Phi}{\partial r_t}$ of Φ with respect to each ion position r_t . Each such derivative corresponds to a 3-dimensional vector whose components are the partial derivatives of Φ with respect to Cartesian coordinates of r_t .

Proposition 7. *The internal electrostatic forces of $(\mathcal{C}_n : L_n, R)$ can be written as:*

$$\begin{aligned}
\mathcal{F}_{Coul} &= -\nabla_r \Phi_{Coul} \\
&= -\left(\frac{\partial \Phi_{Coul}}{\partial r_1}, \frac{\partial \Phi_{Coul}}{\partial r_2}, \dots, \frac{\partial \Phi_{Coul}}{\partial r_N} \right)
\end{aligned} \tag{15}$$

where

$$\begin{aligned} \frac{\partial \Phi_{Coul}}{\partial r_t} = & \frac{k_e}{2} \sum_n \left[- \sum_{j=1}^{N'} q_t q_j \left(\frac{2\alpha}{\sqrt{\pi}} \exp(-\alpha^2 \|r_{t,j,n}\|^2) + \frac{\text{erfc}(\alpha r_{t,j,n})}{\|r_{t,j,n}\|} \right) \frac{r_{t,j,n}}{\|r_{t,j,n}\|^2} + \right. \\ & \left. \sum_{i=1}^{N'} q_i q_t \left(\frac{2\alpha}{\sqrt{\pi}} \exp(-\alpha^2 \|r_{i,t,n}\|^2) + \frac{\text{erfc}(\alpha r_{i,t,n})}{\|r_{i,t,n}\|} \right) \frac{r_{i,t,n}}{\|r_{i,t,n}\|^2} \right] + \\ & \frac{k_e}{2} \sum_{G_m \neq 0} \frac{2\pi k_e}{V \|G_m\|^2} \exp\left(-\frac{\|G_m\|^2}{4\alpha^2}\right) \left[- \sum_{j=1}^N q_t q_j \sin(G_m r_{t,j}) + \sum_{i=1}^N q_i q_t \sin(G_m r_{i,t}) \right] G_m, \quad t \in [N] \end{aligned} \quad (16)$$

Proposition 8. *The internal Buckingham forces of $(\mathcal{C}_n : L_n, R)$ can be written as:*

$$\begin{aligned} \mathcal{F}_{Buck} &= -\nabla_r \Phi_{Buck} \\ &= -\left(\frac{\partial \Phi_{Buck}}{\partial r_1}, \frac{\partial \Phi_{Buck}}{\partial r_2}, \dots, \frac{\partial \Phi_{Buck}}{\partial r_N} \right) \end{aligned} \quad (17)$$

where

$$\begin{aligned} \frac{\partial \Phi_{Buck}}{\partial r_t} = & \sum_n \left\{ \sum_{j=1}^{N'} \left[-\frac{A_{tj}}{\rho} \exp\left(-\frac{\|r_{t,j,n}\|}{\rho}\right) - C_{tj} \frac{\exp(-\alpha^2 \|r_{t,j,n}\|^2)}{\|r_{t,j,n}\|^5} \left(\frac{6}{\|r_{t,j,n}\|^2} + 6\alpha^2 + \alpha^6 r_{t,j,n}^4 + 3\alpha^4 \|r_{t,j,n}\|^2 \right) \right] + \right. \\ & \left. \sum_{i=1}^{N'} \left[\frac{A_{it}}{\rho} \exp\left(-\frac{\|r_{i,t,n}\|}{\rho}\right) + C_{it} \frac{\exp(-\alpha^2 \|r_{i,t,n}\|^2)}{\|r_{i,t,n}\|^5} \left(\frac{6}{\|r_{i,t,n}\|^2} + 6\alpha^2 + \alpha^6 \|r_{i,t,n}\|^4 + 3\alpha^4 \|r_{i,t,n}\|^2 \right) \right] \right\} \frac{r_{i,t,n}}{\|r_{i,t,n}\|} - \\ & \frac{\pi^{3/2}}{12V} \sum_{G_m \neq 0} \left\{ \sum_{j=1}^N C_{tj} \left[\sqrt{\pi} \cdot \text{erfc}\left(\frac{G_m}{2\alpha}\right) + \left(\frac{4\alpha^3}{k^3} - \frac{2\alpha}{G_m} \right) \exp\left(-\frac{G_m^2}{4\alpha^2}\right) \right] \cdot \sin(G_m r_{t,j,n}) + \right. \\ & \left. \sum_{i=1}^N C_{it} \left[\sqrt{\pi} \cdot \text{erfc}\left(\frac{G_m}{2\alpha}\right) + \left(\frac{4\alpha^3}{k^3} - \frac{2\alpha}{G_m} \right) \exp\left(-\frac{G_m^2}{4\alpha^2}\right) \right] \cdot \sin(G_m r_{i,t,n}) \right\} G_m, \quad t \in [N] \end{aligned} \quad (18)$$

The sum of Equations (16), (18) constitutes the partial derivative of the overall energy potential function Φ with respect to ion position r_t , $t \in [N]$. Hence, each such derivative is one of the N components of

$$\mathcal{F} = -\nabla_r \Phi = \mathcal{F}_{Coul} + \mathcal{F}_{Buck} \quad (19)$$

that correspond to the internal coordinate forces.

5.2 External Coordinates

When performing structural relaxation, the initial state of the crystal is assumed to be in a state of agitation. This means that there are two factors preventing the crystal state to reach equilibrium. On the one hand, the distance among each pair of ions does not counterbalance the acting forces per ion. On the other hand, the crystal lattice is in a shape that does not correspond to the equilibrium state, it is deformed. Thus, apart from using the previously listed derivatives with respect to ion positions, we need to change the lattice vectors and express the forces acting on the vectors in such a way, so as to combine position derivatives and lattice forces into one updating step. In the following paragraphs we are going to elaborate on how this deformation affects the derivatives of the energy. A large part of the following discussion is owed to the book by Crandall et al. [11].

As with the motion of the ions, we can differentiate the energy function Φ with respect to the lattice vectors L_n and derive the forces acting on each vector's l_1, l_2, l_3 component. This process allows the vectors to move freely in three ways each and, thus, can lead to many steps of the relaxation process describing rigid body movements. These movements have no impact to the shape of the unit cell and can slow down the structural relaxation, as well as interfere with the calculations in a negative way while the unit cell seemingly travels in the three-dimensional space.

For this reason, we use a different set of variables to relax, so that only deformation, compression or elongation of the lattice vectors and relative rotation, is involved in the optimisation of the lattice. By separating the affected quantities to lengths and angles, we can eliminate rigid body movements and limit the degrees of freedom of the lattice to six one-dimensional variables in a symmetrical tensor ϵ . Then at each step of the optimisation the lattice vectors are characterised by a state of strain $0, \epsilon_1, \dots, \epsilon_n$.

Proposition 9. *The forces that act on the volume of a unit cell \mathcal{C}_n and change the shape of the crystal lattice can be expressed with the symmetric stress tensor $\sigma = \{\sigma_{\lambda\mu}\}_{\lambda,\mu \in [3]}$ as a result of an existing strain $\epsilon = \{\epsilon_{\lambda\mu}\}_{\lambda,\mu \in [3]}$.*

The parameters affected by stress are R, L_n, G_m , hence each stress component $\sigma_{\lambda\mu}$ is calculated as

$$\sigma_{\lambda\mu} = \frac{1}{V} \left(\sum_n \sum_{i=1}^N \frac{\partial \Phi}{\partial r_{i\lambda}} r_{i\mu} + \sum_n \frac{\partial \Phi}{\partial L_{n\lambda}} L_{n\mu} + \sum_m \frac{\partial \Phi}{\partial G_{m\mu}} G_{m\lambda} + \frac{\partial \Phi}{\partial V} \delta_{\lambda\mu} V \right) \quad (20)$$

The overall stress can be easily calculated by separately evaluating the stress produced by Coulomb and Buckingham stresses so that $\sigma_{\lambda\mu} = \sigma_{(Coul)\lambda\mu} + \sigma_{(Buck)\lambda\mu}$. By Theorem 9 and Lemma 5.2 the following corollaries arise naturally.

Corollary 2. *The stress applied on the unit cell volume due to Coulomb forces is calculated as:*

$$\begin{aligned} \frac{\partial \Phi_{Coul}^S}{\partial \epsilon_{\lambda\mu}} &= \sum_{i,j,n}^{N'} q_i q_j \left[k_e \frac{-\alpha' V}{\sqrt{\pi}} \exp(-\alpha^2 \|r_{i,j,n}\|^2) \delta_{\lambda\mu} + f'_S(\|r_{i,j,n}\|) \frac{r_{i,j,n(\lambda)}}{\|r_{i,j,n}\|} r_{i,j,n(\mu)} \right] \\ \frac{\partial \Phi_{Coul}^L}{\partial \epsilon_{\lambda\mu}} &= \frac{2\pi k_e}{V} \sum_{i,j,G_m \neq 0} q_i q_j \frac{\exp(-\frac{G_m^2}{4\alpha^2})}{G_m^2} \cos(G_m r_{i,j}) \left[\left(\frac{1}{2\alpha^2} + \frac{2}{G_m^2} \right) G_{m\mu} G_{m\lambda} - \delta_{\lambda\mu} \left(1 - \frac{G_m^2}{2\alpha^3} \alpha' V \right) \right] \\ \frac{\partial \Phi_{Coul}^{self}}{\partial \epsilon_{\lambda\mu}} &= \delta_{\lambda\mu} \frac{\alpha' V k_e}{\sqrt{\pi}} \sum_i q_i^2 \end{aligned} \quad (21)$$

and ultimately

$$\sigma_{(Coul)\lambda\mu} = \frac{1}{V} \left(\frac{\partial \Phi_{Coul}^S}{\partial \epsilon_{\lambda\mu}} + \frac{\partial \Phi_{Coul}^L}{\partial \epsilon_{\lambda\mu}} - \frac{\partial \Phi_{Coul}^{self}}{\partial \epsilon_{\lambda\mu}} \right) \quad (22)$$

Corollary 3. *The stress applied on the unit cell volume due to Buckingham forces is calculated as:*

$$\begin{aligned} \frac{\partial \Phi_{Buck}^S}{\partial \epsilon_{\lambda\mu}} &= - \sum_{i,j,n}^{N'} \frac{C_{i,j}}{\|r_{i,j,n}\|^6} \exp(-\alpha^2 \|r_{i,j,n}\|^2) \left[\left(\frac{6}{\|r_{i,j,n}\|^2} + 6\alpha^2 + \alpha^6 \|r_{i,j,n}\|^4 + 3\alpha^4 \|r_{i,j,n}\|^2 \right) r_{i,j,n(\lambda)} r_{i,j,n(\mu)} + \right. \\ &\quad \left. \alpha' \alpha^5 V \|r_{i,j,n}\|^6 \delta_{\lambda\mu} \right] \\ \frac{\partial \Phi_{Buck}^L}{\partial \epsilon_{\lambda\mu}} &= \sum_{i,j}^N C_{i,j} \frac{\pi^{3/2}}{12V} \sum_m \cos(G_m r_{i,j}) \cdot \left[\left(3\sqrt{\pi} \|G_m\| \operatorname{erfc}\left(\frac{\|G_m\|}{2\alpha}\right) - 6\alpha \exp\left(-\frac{G_m^2}{4\alpha^2}\right) \right) G_{m\mu} G_{m\lambda} - \right. \\ &\quad \left. \delta_{\lambda\mu} \left(-\sqrt{\pi} \operatorname{erfc}\left(\frac{\|G_m\|}{2\alpha}\right) G_m^3 + (-2\alpha^2 + G_m^2 + 6V\alpha\alpha') 2\alpha \exp\left(-\frac{G_m^2}{4\alpha^2}\right) \right) \right] \\ \frac{\partial \Phi_{Buck}^{self}}{\partial \epsilon_{\lambda\mu}} &= - \sum_{i,j}^N \frac{C_{i,j}}{3V} \pi^{3/2} \alpha^2 \cdot \frac{3\alpha' V - \alpha}{V} \end{aligned} \quad (23)$$

and ultimately

$$\sigma_{(Buck)\lambda\mu} = \frac{1}{V} \left(\frac{\partial \Phi_{Buck}^S}{\partial \epsilon_{\lambda\mu}} + \frac{\partial \Phi_{Buck}^L}{\partial \epsilon_{\lambda\mu}} - \frac{\partial \Phi_{Buck}^{self}}{\partial \epsilon_{\lambda\mu}} \right) \quad (24)$$

This concludes the presentation of the energy function and its first order derivatives, along with the necessary theory that accompanies the derivations. In the next we emphasize on the experimentation process starting with a description of the employed algorithms.

6 Algorithms

In the following we investigate the performance of Steepest Descent, or Gradient Descent, and Conjugate Gradient. The choice of these algorithms is based on the prospect of selecting stable recipes that are sure to converge to the local energy minimum and investigate how parameter tuning can affect the relaxation. More specifically, we are interested in comparing the stability and convergence speed of their respective updating schemes, as well as understanding how the step size selection can allow for reaching the local minimum or lead to irreversible failure, as described in Paragraph 4.4. We will

begin by describing the non-trivial procedure which is employed in order to correctly update each variable of the energy potential function.

For our experiments, the positions of the ions and the strains of the lattice vectors serve as the input variables. The strain tensor is the infinitesimal version of the change seen in solids under acting forces, as found in [11]. The strain tensor is symmetric so that only 6 degrees of freedom are allowed and are updated in two rounds of calculations. First, the components of the tensor constructed by the last 3x3 symmetric matrix of the vector $s \cdot d$ are decreased by 1, the non-diagonal elements are scaled by 1/2 and the diagonal is increased by 1 to form Δ . Then, the new tensor is the outer product of the old variables and Δ . After each iteration, the variables R and $E[DU]$ receive an increment $s \cdot d$ that moves ions and lattice vectors alike. The whole unit cell is adjusted according to laws of Physics and ions' positions that exceed the borders of the unit cell are wrapped to reenter the unit cell according to periodic boundary conditions (PBS).

Algorithm 2 Algorithm of parameter update

Input step size s , direction vector d , transpose of ion positions R^T , transpose of lattice vectors L^T , strain tensor E

Output updated transpose of ion positions R^T , transpose of lattice vectors L^T and strain tensor E

```

1: function UPDATE( $s, d, R^T, L^T, E$ )
2:    $R^T \leftarrow R^T + s \cdot d[1, \dots, N]$  ▷ Ion positions' update
3:    $E[DU] \leftarrow E[DU] + s \cdot d[N + 1, \dots, N + 6]$  ▷ Strain update
4:    $E[L^T] \leftarrow E[U]$  ▷ Render strain matrix symmetric
5:    $\Delta \leftarrow (E - J_3)^T S_3 + I_3$ 
6:    $L^T \leftarrow L^T \Delta^T$  ▷ Apply strains to lattice vectors
7:    $R^T \leftarrow R^T \Delta^T$  ▷ Apply strains to ion vectors
8:   return  $R^T, L^T, E$ 

```

In the above we denote with L, D, U the matrix decomposition in lower triangular, diagonal and upper triangular parts, so that matrix E will be populated with the six values $d[N + 1, \dots, N + 6]$ according to the Voigt notation. Moreover, S, J_3, I_3 stand for the following matrices

$$S_3 = \begin{bmatrix} 1 & \frac{1}{2} & \frac{1}{2} \\ \frac{1}{2} & 1 & \frac{1}{2} \\ \frac{1}{2} & \frac{1}{2} & 1 \end{bmatrix}, \quad I_3 = \begin{bmatrix} 1 & 0 & 0 \\ 0 & 1 & 0 \\ 0 & 0 & 1 \end{bmatrix}, \quad J_3 = \begin{bmatrix} 1 & 1 & 1 \\ 1 & 1 & 1 \\ 1 & 1 & 1 \end{bmatrix}$$

In order to avoid a large percentage of Buckingham catastrophes, a strain reset must be in place. This means that there must be an interval after which the current configuration is assumed to be the initial one, the crystal structure without any stress present. This is achieved by setting the components of strain matrix E to 1, so that $E = I_3$, every $3N + 9$ iterations. We selected this interval as a reset point according to the number of parameters of the problem P and the least steps possible to relax the structure, however its duration is yet to be optimised.

Below are the descriptions of Gradient Descent and Conjugate Gradient as adapted to our Problem P . We have included detailed pseudocodes that can be directly compared to our implementation.

6.1 Gradient Descent

Steepest descent is a simple method relying on the function gradient to define the search direction of the optimisation. Let $\mathcal{F} : \mathbb{R}^n \rightarrow \mathbb{R}$ a multivariate differentiable function. Then the negative of the gradient vector $\nabla \mathcal{F}$ determines the direction with maximum decrease. The search direction for minimising the objective function is usually normalised:

$$d_i = -\frac{\nabla f(x_i)}{\|\nabla f(x_i)\|}.$$

Once search direction is calculated, a find a step size a_i is provided. Thus, at each iteration the approximation is updated as:

$$x_{i+1} = x_i + a_i d_i.$$

During the first round of our experiments we employ Gradient Descent as described in Algorithm 3 where d is the gradient vector $\nabla_{R,L} \Phi_t$ divided by the gradient norm g . The different nature of the

function's parameters, ion positions and strains, tends to create large differences in their updating values, hence, the direction vector comprises components of different order. The division by the gradient norm as calculated in Equation (26) provides stability to the method. We set $tol = 1e-3$ and $I = 50000$, the justification of which is in Section 7.1.

Algorithm 3 Algorithm of Gradient Descent

Input constant step size s , energy function Φ , initial configuration R_0, L_0

Output relaxed structure R_t, L_t

```

1: procedure GD( $R_0, L_0$ )
2:    $E_0 \leftarrow J_3$ 
3:    $\Phi_0 \leftarrow \Phi(R_0, L_0)$ ,  $i \leftarrow 0$ 
4:   for  $i = 1, \dots, I$  do
5:      $d_i \leftarrow -\nabla_{R,L} \Phi_i / g(R_i, L_i)$   $\triangleright$  Function  $g$  computes the gnrm as described in Eq. 26
6:      $R_{i+1}, L_{i+1}, E_{i+1} \leftarrow \text{UPDATE}(s, d_i, R_i, L_i, E_i)$ 
7:     if  $g(R_{i+1}, L_{i+1}) < tol$  then
8:       return  $R_{i+1}, L_{i+1}$ 
9:    $\Phi_{i+1} \leftarrow \Phi(R_{i+1}, L_{i+1})$ 

```

6.2 Conjugate Gradient

For the second part of our experiments we use Conjugate Gradient, as in Algorithm 4. This is a conjugate directions method for nonlinear problems, meaning that every produced direction is targeted to be conjugate to all previous directions. The algorithm is inspired by the fact that there are at most N mutually conjugate vectors in an N by N matrix A , so Conjugate Gradient would find a solution in at most N iterations given a linear minimising problem $\min A^T x + b$. The nonlinear version is made possible using the Gram-Schmidt orthonormalising process to create the search directions d_i . Only the first order derivatives are needed for its calculation. The updating method is as follows:

$$\begin{aligned}
 x_{i+1} &= x_i + a_i d_i \\
 p_{i+1} &= r_{i+1} + \beta_{i+1} d_i,
 \end{aligned} \tag{25}$$

where a_i is the step size and d_i is the direction vector. There are various schemes for updating the β parameter. We use the Polak–Ribière method [34] to update the direction vector, which is proven to have good performance in various similar problems. It is an inherently restarting method [36] that avoids repeatedly small steps when the direction vector is almost orthogonal to the residual of the function. We also introduce a manual restart step in ln. 16 aiming to reinforce the effect of recalibrating the algorithm.

Algorithm 4 Algorithm of Conjugate Gradient

Input constant step size s , energy function Φ , initial configuration R_0, L_0 **Output** relaxed structure R_i, L_i

```
1: procedure CG( $R_0, L_0$ )
2:    $\Phi_0 \leftarrow \Phi(R_0, L_0)$ 
3:    $E_0 \leftarrow J_3$ 
4:    $\gamma_0 \leftarrow -\nabla_{R,L} \Phi_0 / g(R_0, L_0)$   $\triangleright$  Function  $g$  computes the gnrm as described in Eq. 26
5:    $R_1, L_1, E_1 \leftarrow \text{UPDATE}(s, d_0, R_i, L_0, E_0)$ 
6:   if  $g(R_1, L_1) < tol$  then
7:     return  $R_1, L_1$ 
8:    $\Phi_1 \leftarrow \Phi(R_1, L_1)$ 
9:    $d_0 \leftarrow \gamma_0, i \leftarrow 1$ 
10:  for  $i = 2, \dots, I$  do
11:     $\gamma_i \leftarrow -\nabla_{R,L} \Phi_i / g(R_i, L_i)$ 
12:     $\beta_i \leftarrow \gamma_i^T (\gamma_i - \gamma_{i-1}) / (\gamma_i^T \gamma_i)$ 
13:     $d_i = \gamma_i + \beta_i d_{i-1}$ 
14:    if  $i \bmod (3N + 9) == 0$  then  $\triangleright$  Restart CG procedure
15:       $E_i \leftarrow J_3$   $\triangleright$  Strain reset
16:       $d_i \leftarrow -\nabla_{R,L} \Phi_i / g(R_i, L_i)$ 
17:       $R_{i+1}, L_{i+1}, E_{i+1} \leftarrow \text{UPDATE}(s, d_i, R_i, L_i, E_t)$ 
18:      if  $g(R_{i+1}, L_{i+1}) < tol$  then
19:        return  $R_{i+1}, L_{i+1}$ 
20:     $\Phi_{i+1} \leftarrow \Phi(R_{i+1}, L_{i+1})$ 
```

7 Experimental Setting

In this section we will introduce the experimentation process. We first describe the purpose of our experiments and provide an outline of what is presented in the results. Afterwards, we include a technical description of the input and software used for their execution.

7.1 Description

Experiments on crystal structures have been conducted since the very conception of some optimisation methods used today to minimise functions such as the cost function of neural networks. However, little work has been done on treating the relaxation procedure as an algorithm destined for Crystal Structure Prediction and formally exhibiting the properties and requirements of this setting in Computer Science terms. Our experiments' goal is to close this gap and explore the properties of the energy function, as well as to identify the best algorithmic techniques that suit this minimisation problem.

Gradient Descent is usually the to-go algorithm for any non-convex local optimisation problem. On the one hand, it is intuitively easy to understand as it is merely following the gradient, which provides the way of the function's quickest decrease. On the other hand, it can be robust enough to eventually lead to the minimiser using only the first, and easiest to compute, derivatives. However, our results suggest that Conjugate Gradient is a valuable alternative optimisation algorithm which is not only occasionally more trustworthy than Gradient Descent, but also quicker to converge. Thus, we test the following hypotheses:

- Conjugate Gradient is more robust than Gradient Descent.
- Careful step size selection improves the optimisation's performance.
- There is a trade-off between convergence speed and robustness.
- There is a connection between the gradient and the iteration number after the algorithm reaches a certain stage of the computations.

We test each of the above hypotheses experimentally and we provide an enhanced algorithmic recipe reflecting the conclusions drawn from our results. We trial the convergence and speed of

Gradient Descent and Conjugate Gradient under 4 step size adaptations: a) constant step size, b) exponential scheduled step size (*expo*), c) constant scheduled bisection (*bisect*) for the step size and c) gradient-norm-related scheduled (*gbisect*) step size. We examine the impact of various constant step size values under three conditions, namely, the number of successful experiments over all structures, the runtime, in terms of number of iterations per run, and the number of concluded experiments out of all experiments inside a given deadline, again in terms of iteration number. We, then, analyse the behaviour of each step size recipe under the same conditions and select the optimal per method. The results of the experiments will give rise to a **trade-off** whereby, step size recipes that reduce the runtime result into more failed experiments. This becomes particularly prominent with constant step sizes, as, the larger the step size gets, the more the number of experiments that do not finish before a set deadline increases. Therefore, a function will be proposed to measure the utility of each algorithm with each step size adaptation.

For the first phase of our experiments, each structure underwent 10 minimisations; 5 minimisations for each of Gradient Descent and Conjugate Gradient methods with 5 different constant step sizes. For the second phase of our experiments we included another 3 kinds of runs during which the step size changes according to some rule, called scheduling rule. For each step size updating rule various hyperparameters were tested and evaluated, and one configuration was finally selected as optimal.

Every structure, needing several structural modifications to approach equilibrium, underwent a procedure with which each minimisation iteration corresponds to two parameter updates. Firstly, a displacement of all ions in the unit cell and, second, a length and angle adaptation of the unit cell vectors; in other words, a structural relaxation iteration. In simple terms, with each parameter update as in Algorithm 2, we move the ions R in the unit cell, then we stretch or shrink the lattice vectors L and change the three angles in between the lattice vectors. The direction of movement or change is given by a vector d from the sequence of direction vectors $\{d_i\}_{i=0}^{i_f}$, $d_i \in \mathbb{R}^{3N+6}$ where i_f is the last iteration of each experiment. For Gradient Descent d_i is set according to line 5 of Algorithm 3 and for Conjugate Gradient Descent d_i is set according to line 13 of Algorithm 4. The relaxation follows this sequence of directions until one of the following occurs; either the gradient norm g has fallen below some tolerance value tol , in our case $tol = 1e-3$, and the resulting potential energy Φ is less than the energy Φ_0 of the initial configuration, or the experiment fails. A failed experiment could either have reached a maximum number of updating iterations, finished the relaxation with a higher energy than the initial energy or fallen into Buckingham catastrophe. In more detail:

We refer to the following as the gradient norm

$$g(R, L) = \frac{\sqrt{\sum_{i=1}^N ((\frac{\partial \Phi}{\partial r_{ix}})^2 + (\frac{\partial \Phi}{\partial r_{iy}})^2 + (\frac{\partial \Phi}{\partial r_{iz}})^2) + \sum_{i=1}^6 \frac{\partial \Phi}{\partial \epsilon_i}^2}}{3N + 6} \quad (26)$$

and we announce a successful relaxation when

$$g < 1e-3 \text{ and } \Phi < \Phi_0 \quad (27)$$

Since our experiments' input is constructed in a way such that R_0, L_0 is not very "close" to the stable $\text{Sr}_3\text{Ti}_3\text{O}_9$, we allow for a margin of error ϵ which enables our methods to converge to the *true* local minimum of R_0, L_0 .

We consider an experiment outcome a failure when one of three cases appear that cause a termination. The first case is closely related to the nature of the energy model, specifically the Buckingham energy potential. We say that an experiment has failed when Buckingham *catastrophe* happens (see Section 4.4), which results into a constantly increasing gradient norm and decreasing energy value. Secondly, we say that a relaxation has failed when the conditions 27 are not fulfilled and the iteration number i has reached 50000 iterations, which we describe as *overtime*. This result indicates that the step size magnitude is large enough to prevent convergence below the selected tolerance in a reasonable time margin and cannot guarantee a finite sequence of iterations. We observed that when the step size is too big the gradient and energy started to oscillate and their values could not decrease below some threshold in a sensible amount of time. An example of a structure arriving at such a situation is shown in Figure 5. Lastly, we include a special case of failure for the larger step size cases of runs. This is when, in spite of the iteration number $i < I$, the experiment had not completed in the time interval of 3 days after its submission. This case arose only for the category of experiments on the largest constant step size and concerns only a minority of the dataset, while the rest of the structures of this category of experiments came to failure due to the aforementioned reasons. We can, hence,

safely assume that experiments running for 3 days were destined to fail either due to Buckingham catastrophe or due to reaching the iteration limit I .

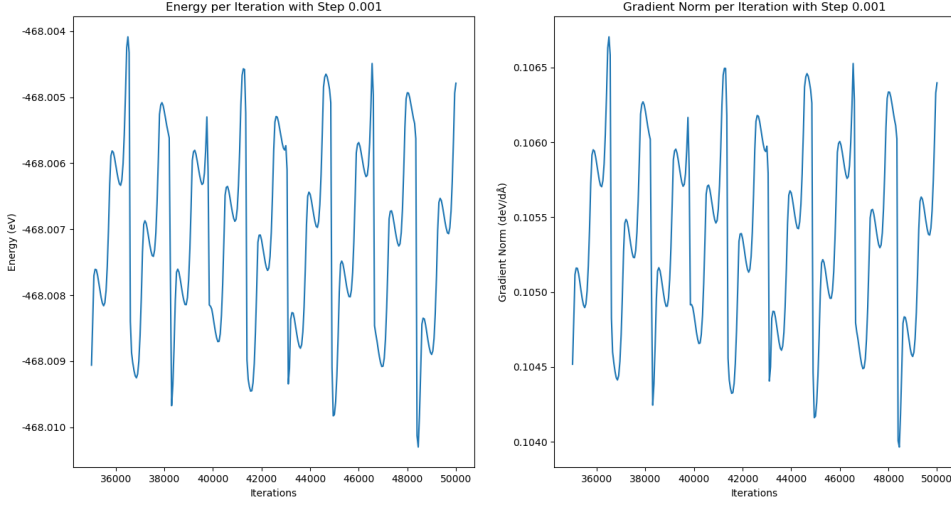
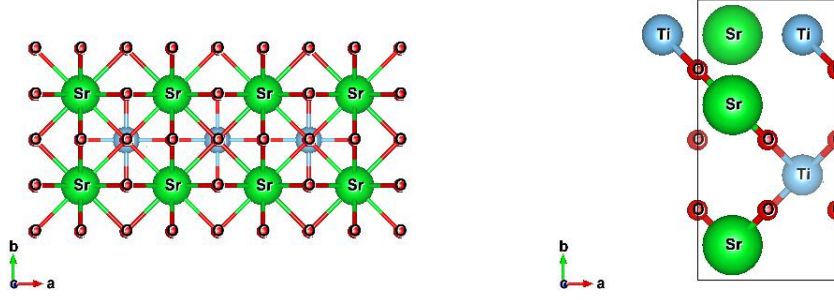


Figure 5: **Oscillating energy and gradient norm.** *Left*, Energy versus iteration number for one structure being relaxed with a large constant step $s = 1\text{e-}3$; *right*, Gradient norm versus iteration number for one structure being relaxed with a large constant step $s = 1\text{e-}3$.

7.2 Datasets

For our experiments we have used a set of crystal structures specially tailored for challenging structural relaxation strategies to find the local minimum. These are 200 structures have been produced with a stable Strontium Titanate ($\text{Sr}_3\text{Ti}_3\text{O}_9$) as a reference point and the introduction of randomness to the placement of strontium, titanium and oxygen atoms inside the unit cell. More specifically, after defining the length of each lattice vector from a set of values of 4, 6, 8, 10, and 12 Angstroms, an orthorhombic unit cell is formed. Then, 15 ions – 3 strontium, 3 titanium and 9 oxygen ions – are placed in a random manner on grid points defined by a 1 Angstrom grid spacing, such that the negative ions are placed on grid points with even indices, and positive ions and are placed on grid points with odd indices. Figure 6a and Figure 6b illustrate the stable and a representative example of the random structures respectively. This construction method provides input elements that are not likely to lie near the PES minimum, thus allowing to test if an algorithm can find the minimum despite it being far away. The 200 structures were divided into 5 groups of 40 randomly to provide an unbiased basis for statistical analysis of the results.



(a) An example of stable $\text{Sr}_3\text{Ti}_3\text{O}_9$ structure. (b) An example of a random $\text{Sr}_3\text{Ti}_3\text{O}_9$ structure.

Figure 6: **Illustrations of the crystal structure with the chemical formula $\text{Sr}_3\text{Ti}_3\text{O}_9$ in stable state and after random placement of the ions in the unit cell.** The unit cell of the crystal in the first image is constructed by the double duplication of SrTiO_3 along x-axis and constitutes a configuration with minimum energy on the PES. The unit cell of the second image depicts the result of the random placement of ions on a grid of 1 Angstrom and is an example of the input data used to find a minimum on the PES.

7.3 Software

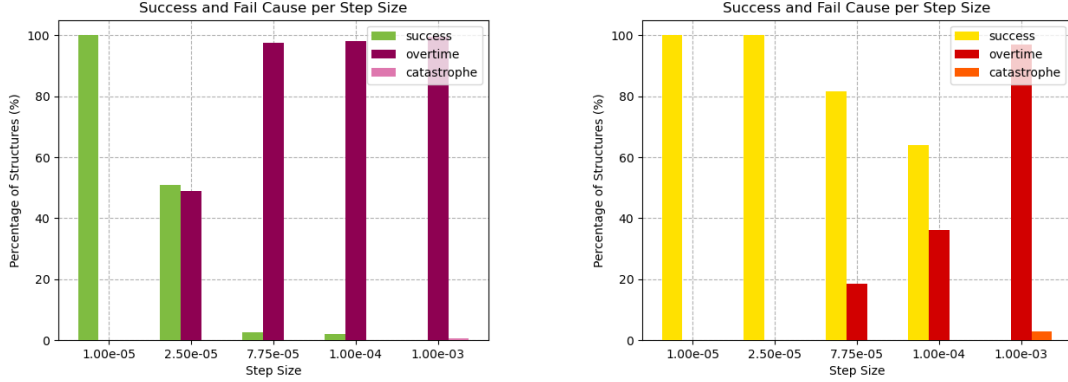
Our implementation offers the aforementioned energy and forces calculations as in Equations (7)-(13) using the *Inflated Cell Truncation* method. Input can be defined using ASE’s[25] *Atoms* class or read as a *CIF* file[20]. Other ASE tools for geometry and input-output tools have also been used. The implementation’s backbone calculations are written in Cython and parts such as input handling are written in Python. The calculations of the derivatives have been tested with the corresponding numerical evaluations. A unit testing suite is included and energy calculations have been compared against GULP’s [17] and LAMMPS’s [26] corresponding calculations. The output can be configured to extract PNG images and CIF files for each produced crystal structure configuration every requested number of iterations. There is also the option to pause the execution at every step or allow the relaxation to develop until its very conclusion.

In the next section, we will first present the results of experiments running on constant step size s and provide a direct comparison of Gradient Descent and Conjugate Gradient in this context. We will also attempt to analyse some measures of the crystal structure to understand how these affect the relaxation duration. In the second experimental analysis section, we will present the results from relaxations run with scheduled step size. A utility function will be introduced in order to measure the performance of the two algorithms both with constant and scheduled step size.

8 Experimental Analysis I – Constant Step

We test five values for the constant step size, namely $1\text{e-}5$ (small), $2.5\text{e-}5$, $7.75\text{e-}5$, $1\text{e-}4$ (medium) and $1\text{e-}3$ (large). Our choice of the lower step size value was determined empirically and stemmed out of the hypothesis that there is at least one local minimiser in the feasible neighbourhood around R_0, L_0 . This is a justified hypothesis taking into account that we already know a stable structure with similar configuration to each (R_0, L_0) , the stable $\text{Sr}_3\text{Ti}_3\text{O}_9$. After several experiments we achieved a successful relaxation for **100%** of the dataset using a constant $s = 1\text{e-}5$ for both examined methods as seen in Tables 2, 3. The results from these runs showed that a successful relaxation would terminate in less than 50000 cycles in all cases. Our next goal was to accelerate convergence using larger step sizes, consequently, we set our limit for the number of iterations to 50000. Further testing revealed that our experimental setting has a tolerance for a constant step size in the range $[1\text{e-}5, 1\text{e-}3]$ above which all data structures fail to relax. Figure 7 illustrates that, both for Gradient Descent (Figure 7a) and Conjugate gradient (Figure 7b), 0% of instances converged with $s = 1\text{e-}3$ according to some failure reason as described in the above. Thus, $1\text{e-}3$ will be the highest value of the step size that we test. In order to investigate the algorithms’ behaviour for step sizes in the range $(1\text{e-}5, 1\text{e-}3)$, we

complete a set of step size values to test with $2.5\text{e-}5$, $7.75\text{e-}5$ and $1\text{e-}4$.



(a) Success rate of tested step sizes with Gradient Descent (b) Success rate of tested step sizes with Conjugate Gradient

Figure 7: **Percentage of success over all 200 structures for relaxations with constant step sizes $1\text{e-}5$, $2.5\text{e-}5$, $7.75\text{e-}5$, $1\text{e-}4$ and $1\text{e-}3$.** The first bar on the left per step size shows the percentage of 200 structures that were successfully relaxed and the next two bars per step size show the ones that failed due to overtime running – reached the budget of iterations – or Buckingham catastrophe.

Small step size When the step size is constantly very small with unchanged value, Gradient Descent and Conjugate Gradient have similar performance. The smallest step size $s = 1\text{e-}5$ cancels the conjugacy between directions produced from Conjugate Gradient, as expected in cases of employment of the Polak–Ribière update [19]. This happens because when the step size value approaches zero $s \rightarrow 0$ then the difference between consecutive gradients decreases $\gamma_i - \gamma_{i-1} \rightarrow 0$ and the direction vector approaches the negative gradient $d_i \rightarrow -\gamma_i$. As a result, Conjugate Gradient acts as Gradient Descent and the two methods appear to have almost *no differences* in consecutive steps.

Medium step size When the step size is more than doubled, from $s = 1\text{e-}5$ to $2.5\text{e-}5$, the behaviour of Conjugate Gradient starts to deviate from that of Gradient Descent. Whilst the percentage of successful experiments in the first case abruptly falls, Conjugate Gradient can still complete all the relaxations, which are also accelerated. In more detail, almost half of the Gradient Descent experiments fail, but all experiments of the latter case are successful and finish in less than half the number of iterations from before.

When $s = 7.75\text{e-}5$ and $s = 1\text{e-}4$, the success rate decreases for both methods, but the decrease is much more rapid for Gradient Descent, with just a few structures being able to finally relax. More specifically, Gradient Descent fails to converge for 98% of the structures. Here, Conjugate Gradient failure number is kept to max 50% of the structures, and the successful relaxations are even more accelerated to a mean ≈ 3500 iterations per optimisation run. Ultimately, a trade-off between success rate and convergence speed is evident, but the high failure rate of Gradient Descent renders it useless for high step size values.

For each increase in the step size value from $s = 1\text{e-}5$ to $7.75\text{e-}5$ we observe that, although we have more failures, we also have less average number of iterations to success. This acceleration is to be expected, for a larger step size suggests larger updates and bigger movements on the PES. This, in turn, suggests quicker convergence to the minimiser. However, when $s = 1\text{e-}4$, we observe a surge of average number iterations to success for some structures relaxed with Conjugate Gradient. We observed that in some cases of structures that were successfully relaxed for both $s = 7.75\text{e-}5$ and $s = 1\text{e-}4$, the relaxations with the latter step size run for at least twice as long. This means that, if these structures were relaxed in ≈ 3500 iterations with $s = 7.75\text{e-}5$, then the iterations with $s = 1\text{e-}4$ were increased to ≥ 7000 . This suggests that for $s = 1\text{e-}4$ a different and longer path is taken towards the local minimum. This also indicates that the larger step size skips the minimum in the first ≈ 3500 iterations. We can conclude that any $s \geq 1\text{e-}4$ when s is constant does not guarantee quicker convergence.

Large step size For this step size value *all* structures fail to relax with a budget of 50000 iterations for either of the two methods. Following our previous observations, we find that almost all failures are caused due to the large step size that fails to accurately approach the small neighbourhood of the local minimum in $I = 50000$ iterations. Here we must report that Conjugate Gradient with this constant step leads several structures to unit cells with very large pairwise distances, so this confirms that the *true* local minimum was missed and another extremum is being followed. All structures that were run with Gradient Descent, except for one, failed due to exhausting the iteration budget I . This one experiment followed a path down the unbounded energy well created by the Buckingham energy potential when ions start to merge. For the first time until this point of our experimentation procedure we come across with a frequent **Buckingham catastrophe** when using Conjugate Gradient with $s = 1e-3$. In this case at least one experiment out of 40 falls into Buckingham catastrophe creating a 2.5% to 5% possibility for a structure to fail because of it. Therefore, we see that large displacements push ion components together into an energy regime that does not allow the procedure to recover from pacing towards $-\infty$. After all, it has been shown in literature [12] that large values in constant step size can cause problems to Conjugate Gradient’s convergence and lead to uphill directions.

Gradient Descent								
	1e-5		2.5e-5		7.75e-5		1e-4	
	Mean Iter	S	Mean Iter	S	Mean Iter	S	Mean Iter	S
batch 1	25100	40	34500	16	50000	0	50000	1
batch 2	28500	40	30400	21	47700	2	47800	2
batch 3	28000	40	29700	22	48900	1	48900	1
batch 4	27600	40	29700	21	48800	1	48800	1
batch 5	28800	40	29200	22	48800	1	50000	0

Table 2: Gradient Descent Statistics

This table lists the mean iteration number (Mean Iter) and the number of successful (S) Gradient Descent relaxations. Each row represents one batch of randomly allocated 40 structures and the results are shown for each constant step size out of $\{1e-5, 2.5e-5, 7.75e-5, 1e-4\}$.

Conjugate Gradient								
	1e-5		2.5e-5		7.75e-5		1e-4	
	Mean Iter	S	Mean Iter	S	Mean Iter	S	Mean Iter	S
batch 1	25100	40	10100	40	12900	32	16300	29
batch 2	28500	40	11400	40	12200	33	27300	20
batch 3	28000	40	11100	40	10200	35	23000	24
batch 4	27600	40	11100	40	13500	32	17600	28
batch 5	28800	40	11500	40	14300	31	19100	27

Table 3: Conjugate Gradient Statistics

This table lists the mean iteration number (Mean Iter) and the number of successful (S) Conjugate Gradient relaxations. Each row represents one batch of randomly allocated 40 structures and the results are shown for each constant step size out of $\{1e-5, 2.5e-5, 7.75e-5, 1e-4\}$.

We will now examine the results from the perspective of two easily available measures, the gradient norm and the maximum pairwise distance. One would expect that the initial gradient norm of the crystal would be a good way to predict what happens during the relaxation. This is because it stands for the forces acting in the unit cell and, thus, closely reflects the structure of the crystal, but also provides the condition for the procedure termination. We will show that this is not true and provide a justification, as well as other measures that are more closely correlated to the end result.

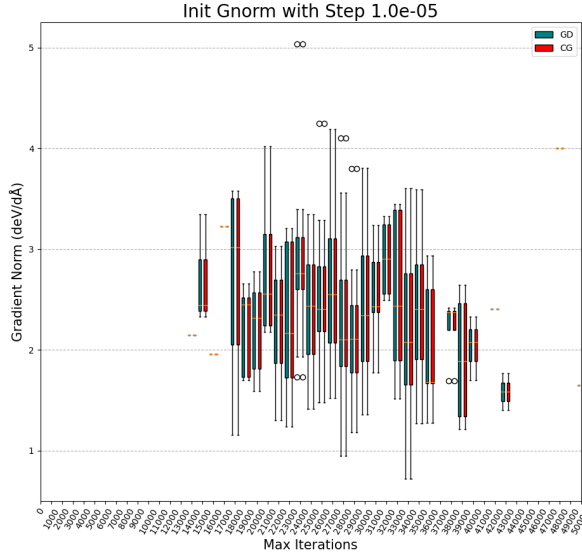
Initial Gradient norm vs total iterations Unfortunately, the gradient norm of the initial configuration does not provide any indication for the total iteration number of successful relaxations. Figure 8 illustrates this argument by associating the range of initial gradient norm values among the 200 structures with the number of steps to success. We observe that the norm varies with undefined

probability in relation to the number of iterations a structure goes through until successful completion. Hence, no predictions can be made with respect to the running time using this information. This is because, when the optimisation starts, we notice a large drop both in energy and gradient values, that eventually stabilises. Figure 9, which depicts the range of number of steps taken to go from a gradient norm value to the immediately smaller, it is apparent that the majority of iterations is realised for gradient norm values smaller than 0.3. This strengthens our argument that in the first few iterations the decrease in gradient and energy is fast and exponential to a degree that their values are not associated with the final iterations.

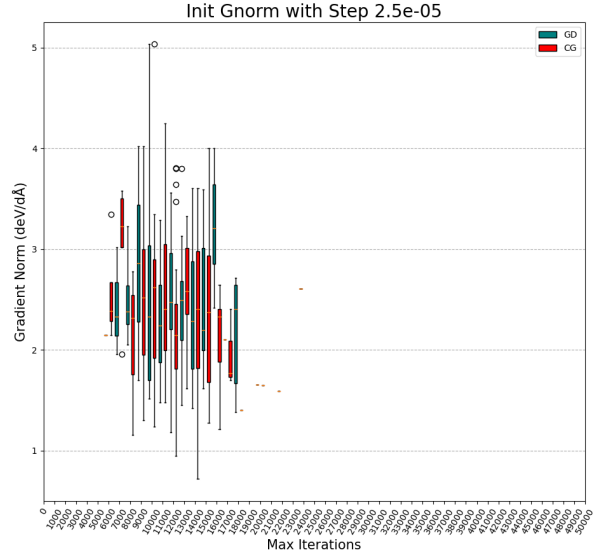
Late Gradient norm vs total iterations This is not true when we examine the gradient norm of a configuration later in the relaxation process. Considering the norm of the gradient around iteration 5000 for $s = 1\text{e-}5$ we can match the increase of its magnitude to the increase in iteration number, according to Figure 10. The almost linear connection of gradient norm and total iteration number becomes even more clear for Conjugate Gradient and step size $s = 2.5\text{e-}5$. This proportionality is to be expected, since a gradient with larger values implies more steps to be taken in order for it to decrease below a certain tolerance value *tol*. This relation cannot be observed when $s = 1\text{e-}4$, for which the gradient norm is not proportional to the iteration number increase.

For Gradient Descent with $s = 2.5\text{e-}5$, on the other hand, same total iteration numbers as when $s = 1\text{e-}5$ are associated with smaller gradient norm values. This means that some experiments studied at the same stage of the relaxation – at 5000 iterations – but with different step sizes, $s = 1\text{e-}5$ and $s = 2.5\text{e-}5$, had reached different energy values with the latter being closer to the minimum. Even so, the relaxation procedure lasted for the same number of iterations, thus more steps were taken close to the minimum for the second case. One can also observe that the iteration number of Conjugate Gradient updates is doubled when $s = 1\text{e-}4$ compared to the iteration number when $s = 7.75\text{e-}5$. This confirms the statement that the increase in step size has prolonged the relaxation process for structures that can be optimised in less steps, indicating that some additional steps were taken to redirect the process towards the local minimum, or a different to the *true* local minimum was approached.

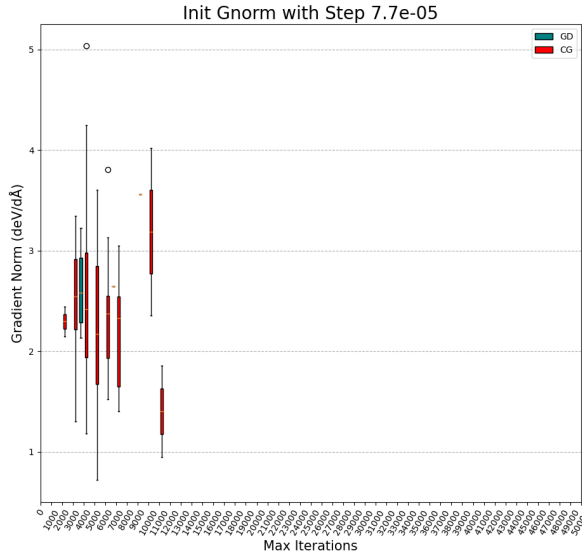
Initial max pairwise distance vs total iterations In contrast to the initial gradient norm, we can predict the number of iterations to success using the maximum pairwise distance of ions in the initial configuration. We anticipate that longer pairwise distances in the cell imply more optimisation steps, and this is confirmed by the following. The range of max pairwise distances in the initial unit cell versus iterations to success is depicted in Figure 11. Pairwise distances in the initial unit cell require accordingly long relaxations to arrive to completion when $s = 1\text{e-}5$ for either Gradient Descent or Conjugate Gradient (Figure 11a). This is also the case for $s = 2.5\text{e-}5$ and Conjugate Gradient, as seen in Figure 11b, yet Gradient Descent starts to show different behaviour with this step size for structures that finish in more than 15.000 iterations. We observe that for the same initial pairwise distances the number of iterations to success has increased for some cases of $s = 2.5\text{e-}5$ compared to $s = 1\text{e-}5$. This happens because Gradient Descent produces large updating steps that cannot lead directly to the minimiser and more iterations are needed to redirect the procedure back to it. However, Conjugate Gradient maintains a seemingly linear relation between total number of iterations and maximum initial pairwise distance for step size values up to $s = 1\text{e-}4$. When $s \geq 1\text{e-}4$ the step size is large enough to break this pattern and more steps are required to adjust the direction of Conjugate Gradient for the minimum to be reached, as seen for the first algorithm and smaller step size values.



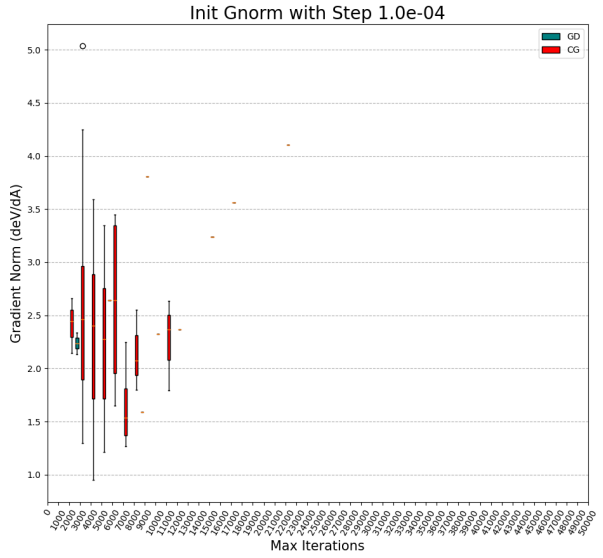
(a) Initial gradient norm versus (rounded to 1000) total iteration number for successful relaxations with constant step $s = 1e-5$.



(b) Initial gradient norm versus (rounded to 1000) total iteration number for successful relaxations with constant step $s = 2.5e-5$.

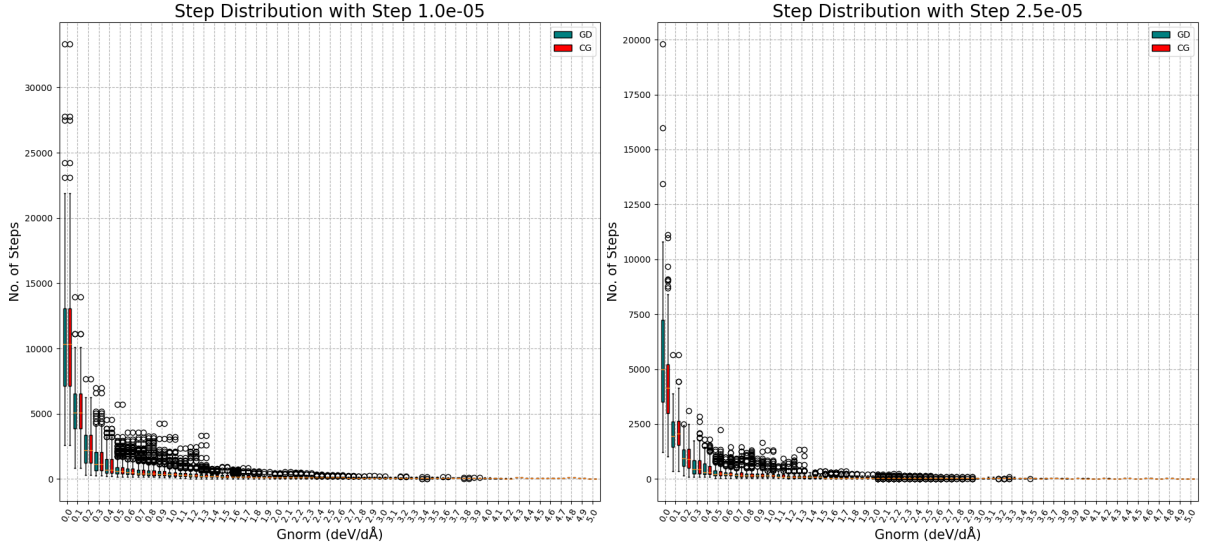


(c) Initial gradient norm versus (rounded to 1000) total iteration number for successful relaxations with constant step $s = 7.75e-5$.



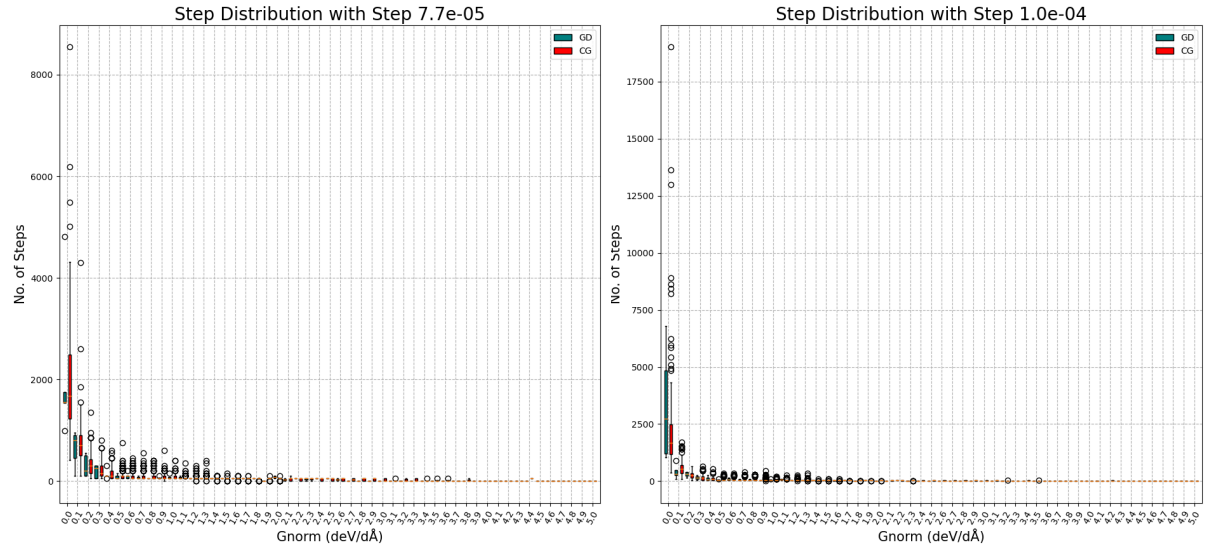
(d) Initial gradient norm versus (rounded to 1000) total iteration number for successful relaxations with constant step $s = 1e-4$.

Figure 8: Range of the initial gradient norm with respect to the number of iterations to success. Figures (a),(b),(c) and (d) show the distribution of the initial gradient norm among total iteration number. The initial gradient norm is the norm of the gradient of a structure that has not undergone any relaxation yet. Each box matches a range of gradient norm values from the y-axis to a rounded total iterations from the x-axis. The purpose of these plots is to show the relation of the initial gradient norm with the number of total iterations that the successful structures underwent. Green boxes correspond to Gradient Descent and red boxes correspond to Conjugate Gradient.



(a) Distribution of iterations to reach values of the gradient norm rounded to the first decimal for experiments run with constant step size $s = 1\text{e-}5$.

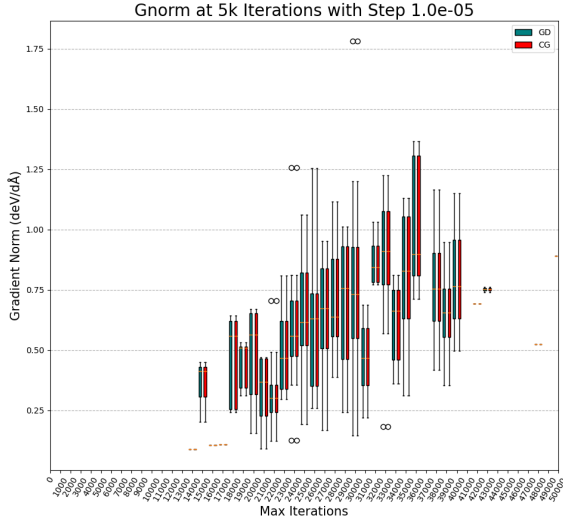
(b) Distribution of iterations to reach values of the gradient norm rounded to the first decimal for experiments run with constant step size $s = 2.5\text{e-}5$.



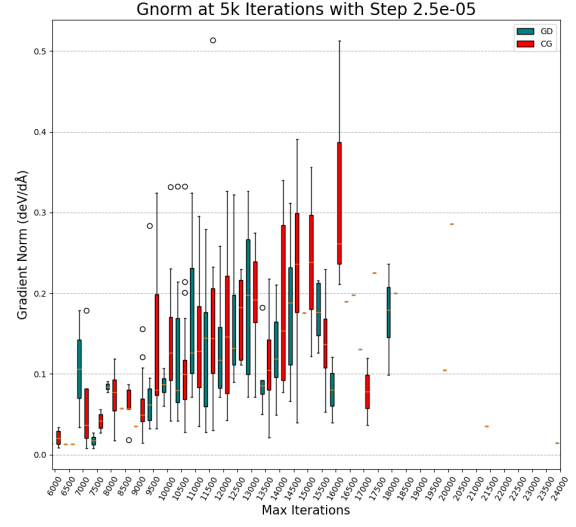
(c) Distribution of iterations to reach values of the gradient norm rounded to the first decimal for experiments run with constant step size $s = 7.75\text{e-}5$.

(d) Distribution of iterations to reach values of the gradient norm rounded to the first decimal for experiments run with constant step size $s = 1\text{e-}4$.

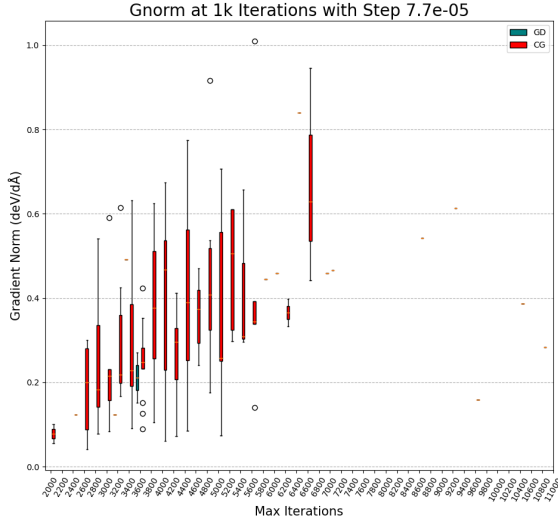
Figure 9: Distribution of relaxation iterations with respect to gradient norm values. In the above plots the y-axis corresponds to number of steps/iterations and the x-axis corresponds to values of gradient norm. Each box shows the range of number of iterations that was needed so that the norm would decrease by 0.1 deV/d\AA . The ranges include the relaxations that were successfully completed using Gradient Descent (green) and Conjugate Gradient (red) with an input of 200 instances.



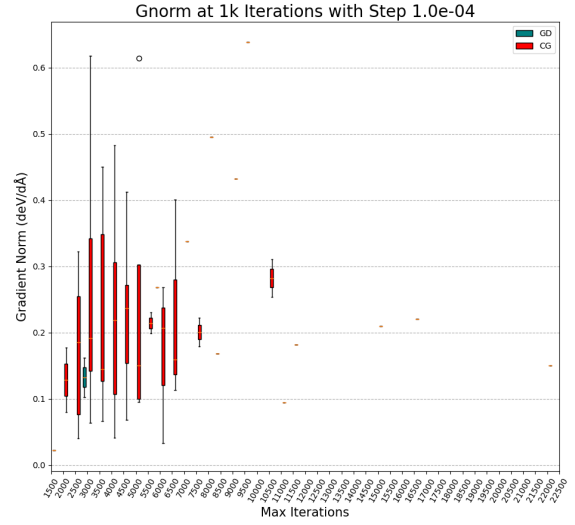
(a) Gradient norm value range at iteration 5000 when the step size is a constant $s = 1e-5$. The x-axis shows the iterations' number to success rounded to 1000.



(b) Gradient norm value range at iteration 5000 when the step size is a constant $s = 2.5e-5$. The x-axis shows the iterations' number to success rounded to 500.

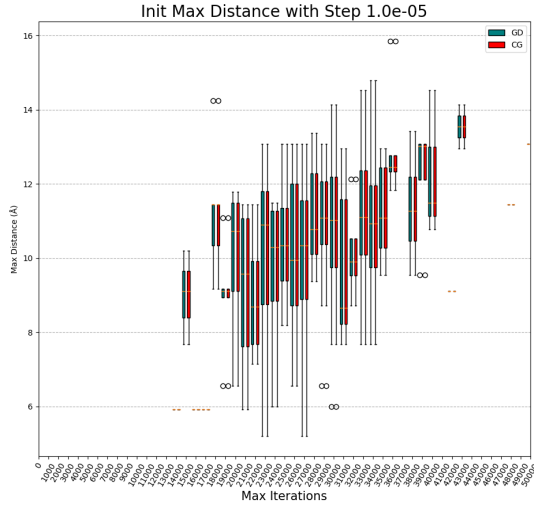


(c) Gradient norm value range at iteration 1000 when the step size is a constant $s = 7.75e-5$. The x-axis shows the iterations' number to success rounded to 200.

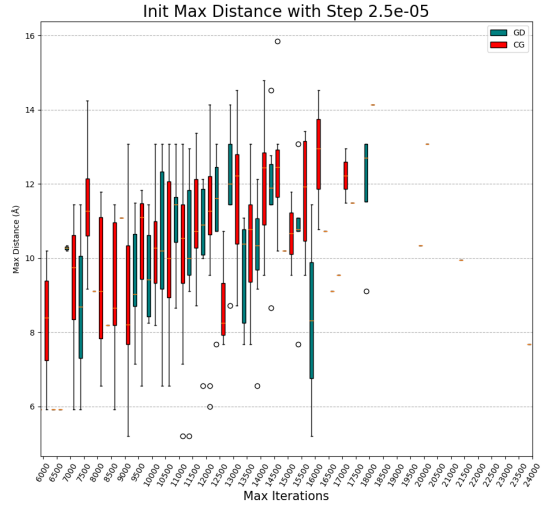


(d) Gradient norm value range at iteration 1000 when the step size is a constant. The x-axis shows the iterations' number to success rounded to 500.

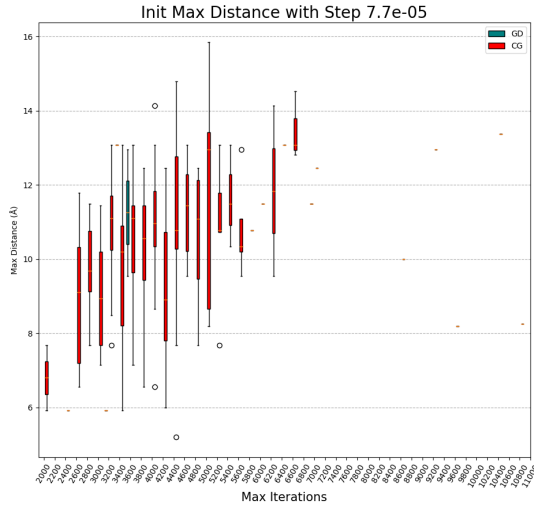
Figure 10: The range of the gradient norm values with respect to the number of iterations to success. Each box matches a range of values of the gradient norm of successful experiments from the y-axis to a number of total iterations on the x-axis. The iteration number has been rounded to different levels per constant step size, in accordance with the overall experimentation process length for the particular step size. The methods used on all 200 structures are Gradient Descent (green) and Conjugate Gradient (red).



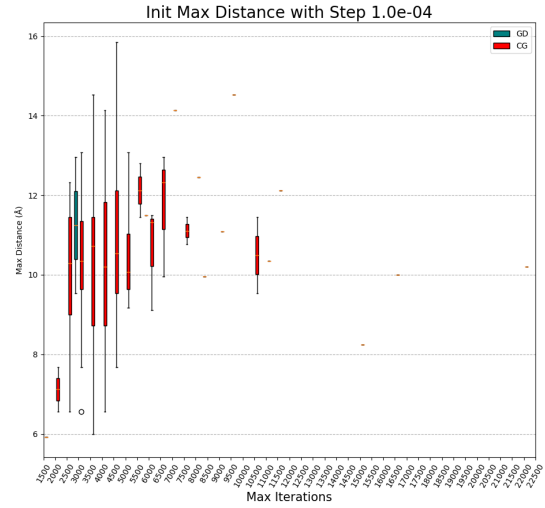
(a) Max pairwise distances in the initial unit cell with respect to the number of iterations to success rounded to 1000. The step size used is a constant $s = 1e-5$.



(b) Max pairwise distances in the initial unit cell with respect to the number of iterations to success rounded to 500. The step size used is a constant $s = 2.5e-5$.

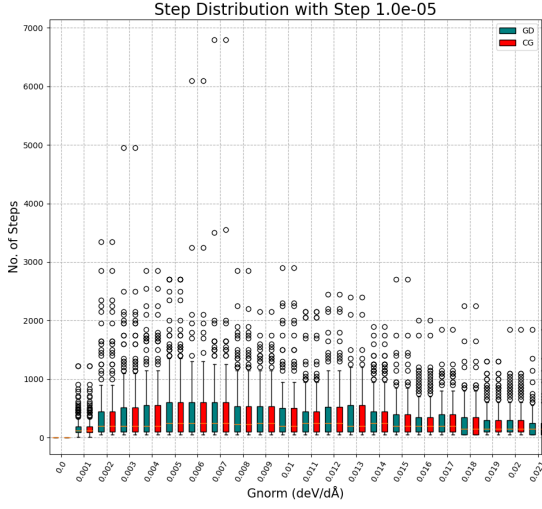


(c) Max pairwise distances in the initial unit cell with respect to the number of iterations to success rounded to 200. The step size used is a constant $s = 7.7e-5$.

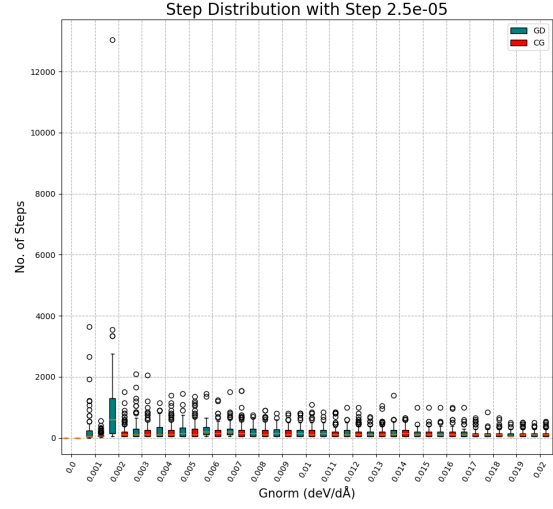


(d) Max pairwise distances in the initial unit cell with respect to the number of iterations to success rounded to 500. The step size used is a constant $s = 1e-4$.

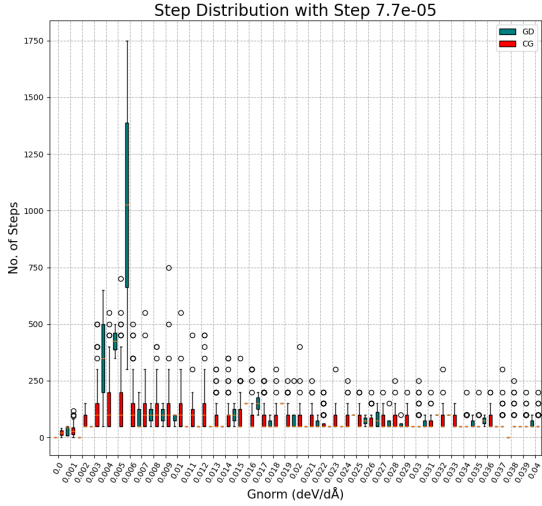
Figure 11: Range of the maximum pairwise distances in the unit cell with respect to the number of steps to success. The distances in question are the pairwise distances of the ions before the relaxation starts. The iteration number has been rounded to different levels per constant step size, in accordance with the overall experimentation process length for the particular step size. The methods used on all 200 structures are Gradient Descent (green) and Conjugate Gradient (red).



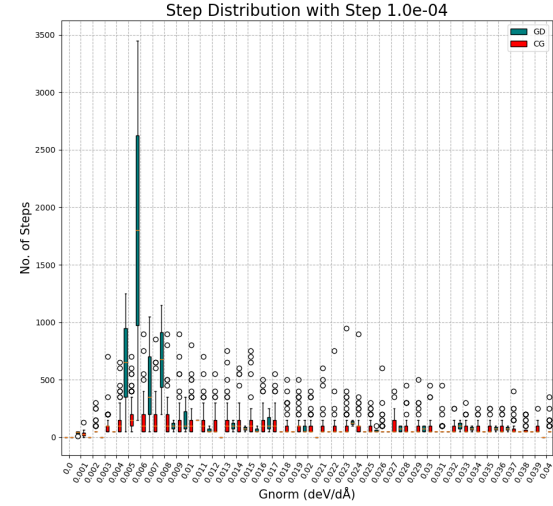
(a) Distribution of steps with respect to a 0.001 \AA gradient norm decrease. The constant step size for this plot was $s = 1e-5$.



(b) Distribution of steps with respect to a 0.001 \AA gradient norm decrease. The constant step size for this plot was $s = 2.5e-5$.



(c) Distribution of steps with respect to a 0.001 \AA gradient norm decrease. The constant step size for this plot was $s = 7.75e-5$.



(d) Distribution of steps with respect to a 0.001 \AA gradient norm decrease. The constant step size for this plot was $s = 1e-4$.

Figure 12: Step number distribution with respect to gradient norm close to zero. The boxes in the above figures show the ranges of number of steps that were needed to decrease from one gradient norm value to the smaller by 0.001 deV/d\AA value. These correspond to the successful experiments out of 200 input structures per method for Gradient Descent (green) and Conjugate Gradient (red) with constant step size. Each plot shows the results for one value of constant step size. The results are focused around a small neighbourhood of the minimum where the gradient norm was less than $4 \cdot 10^{-2} \text{ deV/d\AA}$.

The previously found difference in robustness between Gradient Descent and Conjugate Gradient is owed to the nature of the two algorithms. It is apparent that the first resorts to many iterations of redirection until the path to the minimiser is retrieved, even for as small step sizes as $s = 2.5e-5$. On the other hand, Conjugate Gradient succeeds to steadily approach the minimiser with gradual progress even for $s = 1e-4$. As already mentioned, most of the iterations happen when the gradient norm is below 0.3 and Figure 12 reveals that, for $s > 1e-5$, a vast number of Gradient Descent iterations

is taken towards the end. Nonetheless, with Conjugate Gradient we observe an evenly distributed number of iterations. As a consequence, we can conclude that Conjugate Gradient steadily follows a smooth path constructed to lead towards the minimum, whereas Gradient Descent follows small steps that need constant readjustment in order to eventually point to the correct direction.

Ultimately, different step size values display better performance for different reasons and in combination with different algorithms. The overall winning utility scores for all $\lambda \in [0, 1]$ are displayed by **Conjugate Gradient with constant step size $s = 2.5e-5$** , which provides speed along with high numbers of successful experiments. A small $s = 1e-5$ is also guaranteed to eventually relax all structures, but when low iteration number matters, better options are Conjugate Gradient with $s = 7.75e-5, 1e-4$.

To summarise, we have seen that Conjugate Gradient maintains a success rate of at least 50% in 200 experiments for up to x10 times the smallest constant step size value $s = 1e-5$. On the other hand, Gradient Descent's success rate falls by almost 50% when the step size is roughly doubled from $s = 1e-5$ to $s = 2.5e-5$. This difference is clear when we evaluate the utility of each algorithm with the respective step sizes. Conjugate Gradient can perform well with a wider range of constant step sizes revealing an increased utility both in terms of speed and success rate. This is due to its ability to adapt well the direction of relaxation and make steady progress. Ultimately, its versatility can accelerate a process of multiple experiments without having to resort to failed experiments. We observe, nonetheless, that there is a threshold ($s = 1e-4$) above which step size increase affects the convergence speed of Conjugate Gradient negatively, so one cannot increase the step size value further and expect quicker convergence. For our energy model, a large uneducated increase to the step size can lead to Buckingham catastrophe, which sentences the optimisation procedure to failure. Hence, we conclude that a small step size value that can slowly and steadily lead to the minimum using an update with only the first derivatives, but a larger step size in combination with Conjugate Gradient can accelerate the process.

9 Experimental Analysis II – Utility Comparison

In this Section, we will employ the same two methods and adjust the step size with 3 scheduling rules. We will show that monotonically decreasing the step size affects the results of the methods in different ways depending on the reduction rule. We will also exploit our aforementioned study on constant step size to tune its initial and expected last value.

Bisection (bisect) The first scheduling rule we employed is a simple bisection. The initial value of the step size and a lower bound for it are provided. The step size is initialised and then it is updated with the mean of its current value and the lower bound every 100 iterations. With this rule mean iteration number is reduced to less than half the iterations compared to having the lowest constant step size.

Gradient norm-Scheduled Bisection (gbisect) The step size is initialised with a given upper value. A lower bound is also provided. Once the gradient norm is decreased by some order of magnitude β , the next step size value becomes the mean of the current step size and the lower bound. We compare two values for the order of magnitude; 10 – which we call gbisect10 – and Euler's number (e) – which we call gbisecte. For the same group of structures, gbisect10 performs significantly different for each algorithm, while gbisecte, which reduces the step size much more frequently and quickly, provides similar results for the two algorithms.

Exponential Scheduled (expo) With this rule an upper bound and a lower bound for the value of the step size are provided. The step size is initialised with the upper bound and is then multiplied by a fixed constant number $0 < \gamma < 1$ at every subsequent iteration until it reaches the lower bound. This rule proves to be particularly effective in combination with Gradient Descent. Let $\underline{s} = 1e-5$

and $\bar{s} = 1e-3$, the smallest and largest step size values from the experiments with constant step size. We set the initial value (s_0) of a scheduled step size to be \bar{s} , our lower bound to be \underline{s} and test the

scheduling rules over groups of 40 structures. We define *gbisect* and *gbisect10* as the scheduling rules that follow the *gbisect* scheme and change the step size every time the gradient norm falls by an order of $\beta = e$ (Euler’s number) and $\beta = 10$ respectively. We also let $\gamma = 0.999$ for the *expo* rule.

Figure 13 shows the success rate and range of total iterations for all 200 structures. It illustrates the comparison of Gradient Descent and *expo999*, Conjugate Gradient and *gbisect10* and both algorithms with all constant step sizes in terms of mean iteration number and success rate. However, it is not immediately obvious which combination is the best and under what criteria. The introduction of an iteration deadline affects these results rendering the answer even more difficult.

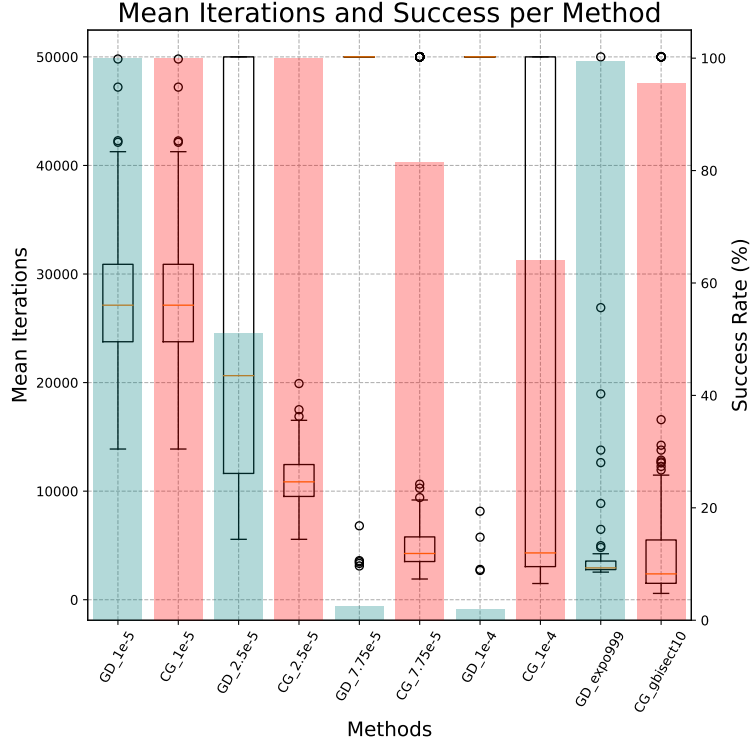


Figure 13: Success rate and iteration number median and deviation for Gradient Descent with *expo999*, $1e-5$, $2.5e-5$, $7.75e-5$, $1e-4$ and Conjugate Gradient with *gbisect10*, $1e-5$, $2.5e-5$, $7.75e-5$, $1e-4$.

Figure 14: **Method comparison in success rate and speed.** The figure depicts the number of structures that were successfully relaxed out of all 200 for Gradient Descent with *expo999* and constant steps (green), but also the number of structures that were successfully relaxed out of all 200 for Conjugate Gradient with *gbisect10* and constant steps (red). The boxes show the median and derivation in number of iterations per method for both failed and successful experiments per method.

We now introduce a utility function to evaluate the performance of Gradient Descent and Conjugate Gradient with different step size arrangements according to Graham D. et al [18]. We set two preferences: success rate and iteration number. The Problem (P’) is a maximisation problem of the utility function $u_{FP} \in \mathbb{R}$:

$$u_{FP} = (1 - \lambda) \cdot \frac{I - i_f}{I} + \lambda\tau \quad (\text{P}')$$

The function is evaluated on the result that each structure produces and then the mean value is used for the overall result per method. The success rate τ is defined as the percentage of structures that was successfully relaxed from the batch that this structure belonged to. The iteration number i_f is the the total number of iterations per experiment. Given the iterations’ upper bound I , we consider i_f to be capped by I . By introducing function $p(i_f, I) = \frac{I - i_f}{I}$ wherein I is a known captime, we construct u_{FP} as in Equation P’. Following the notation of Graham D. et al, we define the two constants c_0, c_1 as $0 < c_1 = 1 - \lambda < 1$ and $c_0 = \lambda\tau$. The λ parameter designates the side – success rate or speed in iterations – to which we place the most preference. According to this preference, we can select the

algorithmic recipe that would mostly correspond to our needs.

9.1 Constant Step Size Utility

As depicted in Figure 15, Gradient Descent and Conjugate Gradient display different levels of utility for different constant step sizes. Also, there is great difference between the two for almost all of the step size values. The utility of Gradient Descent decreases as the step size increases, appointing $s = 1e-5$ as the definitive best choice. Either low iteration number is preferred, in other words $\lambda \rightarrow 0$, or success rate is preferred, namely $\lambda \rightarrow 1$, this step size shows the highest score among other values. While Conjugate Gradient features the highest utility in terms of speed with a constant $s = 2.5e-5$, it manages to relax all structures with both $1e-5$ and $2.5e-5$, thus the two compete for the highest utility score when $\lambda \rightarrow 1$. However, $s = 1e-5$ becomes a good choice only for $\lambda \geq 0.6$, namely, when a low number of failed experiments is more important than low iteration number. For $\lambda < 0.6$ $s = 7.75e-5$ balances success rate and iteration number more favorably than the smallest step size, whose score further drops for $\lambda < 0.3$ and even $s = 1e-4$ is a better choice. Figure 15 confirms once more that Gradient Descent and Conjugate Gradient have similar performance for a small $s = 1e-5$, thus, the aforementioned comparison of Conjugate Gradient with $s = 2.5e-5, 7.75e-5, 1e-4$ and $s = 1e-5$ can be directly applied to Gradient Descent with $s = 1e-5$.

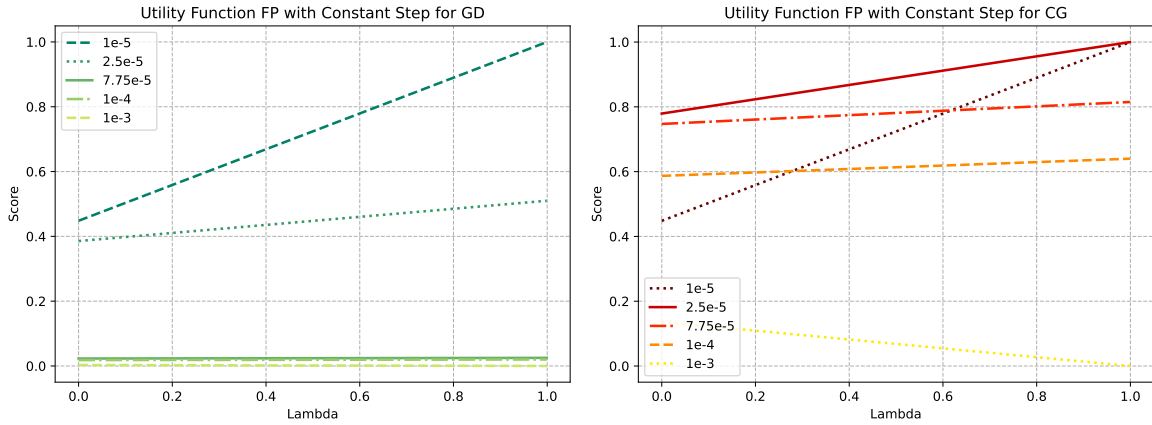
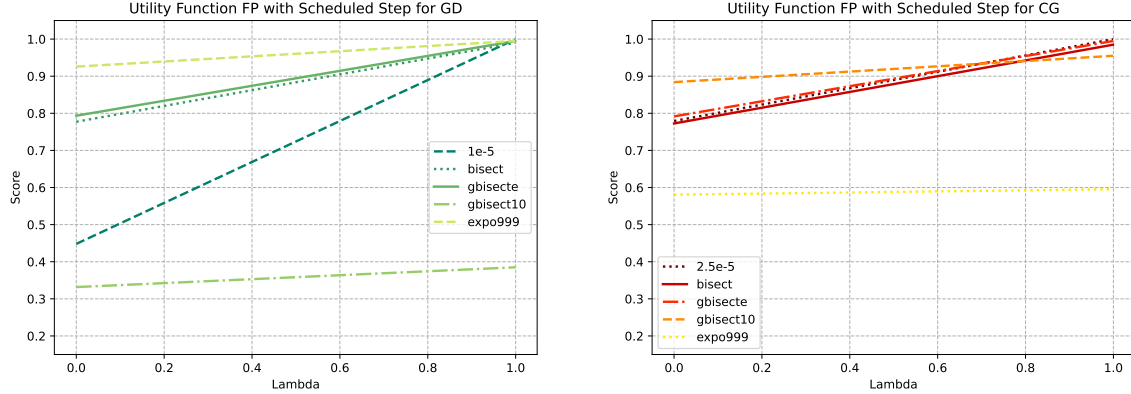


Figure 15: **Utility scores of Gradient Descent and Conjugate Gradient with constant step.** Each line represents results over 200 structures. *Left*, Scores of Gradient Descent run with constant steps $1e-5, 2.5e-5, 7.75e-5, 1e-4$ and $1e-3$ with respect to the λ parameter of the utility function u_{FP} ; *right*, scores of Conjugate Gradient run with constant steps $1e-5, 2.5e-5, 7.75e-5, 1e-4$ and $1e-3$ with respect to the λ parameter of the utility function u_{FP} .

9.2 Scheduled Step Size Utility

The results from scheduled step size experiments, much like the previous experiments, show that different step size recipes provide high utilities for different preferences. Various hyperparameter configurations show that when the step size remains in small values then more structures can be relaxed, while larger step sizes can increase convergence speed. It is also shown that each scheduling rule is effective with a different algorithm between Gradient Descent and Conjugate Gradient. We find that *expo* is more beneficial to Gradient Descent, while *gbisect* with $\beta = 10$ is more beneficial to Conjugate Gradient, and both have roughly the same performance with *bisect*. In the case of Gradient Descent we can observe the same monotonicity as with the constant step sizes in Figure 16. No crossing lines exist, meaning that, when a step size scheduling rule is quick, it is also able to relax more structures. However, results show that there is at least one failed experiment with scheduled step size, such as when using *bisect* or *expo* with $\gamma = 0.999$ and $s_0 = \bar{s}$, thus a constant step size is optimal for $\lambda \rightarrow 1$. On the contrary, as long as Conjugate Gradient is concerned, different rules show different score order depending on the preferences case. While *gbisect* with $\beta = 10$ provides the lowest iteration number, it does not manage to relax a considerable amount of structures. In other words, while for $\lambda \rightarrow 0$ *gbisect* with $\beta = 10$ is the best choice, for $\lambda > 0.8$ other rules with continuous

and small reductions, such as *bisect*, *gbisect*, and definitely the constant $s = 2.5\text{e-}5$, have the best results.



(a) Gradient Descent utility scores with respect to λ . Each line corresponds to a different step size rule including the constant $s = 1\text{e-}5$, bs, gbisectwith $\beta = e$ and $\beta = 10$ and es with $\gamma = 0.999$.

(b) Conjugate Gradient utility scores with respect to λ . Each line corresponds to a different step size rule including the constant $s = 1\text{e-}5$, bs, gbisectwith $\beta = e$ and $\beta = 10$ and es with $\gamma = 0.999$.

Figure 16: Utility scores of Gradient Descent and Conjugate Gradient with constant and scheduled step. The depicted scores correspond to results of relaxations of 200 structures. Each line shows how the score of each method changes according to the parameter λ of the utility function u_{FP} when different rules for changing the step size are applied. For all rules except GD_1e-5 and CG_2.5e-5 the initial step size is $s = s_1$ and its lower bound is s_0 .

Because of the great performance of Gradient Descent with *expo999*, we also experimented with the parameter γ . Figure 17 shows that the monotonicity previously seen with Gradient Descent persists. We notice that the order of Gradient Descent's scores with each γ value, when $\lambda \rightarrow 0$, is preserved until $\lambda \rightarrow 1$, at which point all corresponding lines meet. This means that all rules *expo99*, *expo999*, *expo9999* have relaxed all structures in the same group, thus their speed is what distinguishes them; the optimal rules appears to be forged with $\gamma = 0.999$, which retains a score close to 1 for all $\lambda \in [0, 1]$. A decrease of γ from 0.999 to 0.99 means that the step size's changes are larger and it is more quickly decreased. Reducing $\gamma = 0.9999$ to $\gamma = 0.99$ accomplishes a smaller number of iterations, hence, better results can be obtained when the step size value drops somewhat quicker among iterations.

Another parameter change of exponential scheduled step size was tested, concerning its initial value. We increased it from $s = 1\text{e-}3$ to $s = 10^{-2}$ and decreased it from $s = 1\text{e-}3$ to $s = 1\text{e-}4$. The analysis of this change's impact through the utility function showed that our selection sourced from the constant step experiments, s_1 , was the best choice. More specifically, Gradient Descent with *expo999* and first step size $s = s_1$ has the best scores for all $\lambda \in [0, 1]$ compared to $s = 1\text{e-}4$ and $s = 1\text{e-}2$, as seen in Figure 18a. Actually, the second highest utility score of this method depends on our preferences; if we exclude s_1 from our options, the large $1\text{e-}2$ provides the highest utility for low iteration number, but the small $1\text{e-}4$ provides the highest utility in terms of success rate.

A similar initial step size analysis for *gbisect10* is provided, with the same three different values

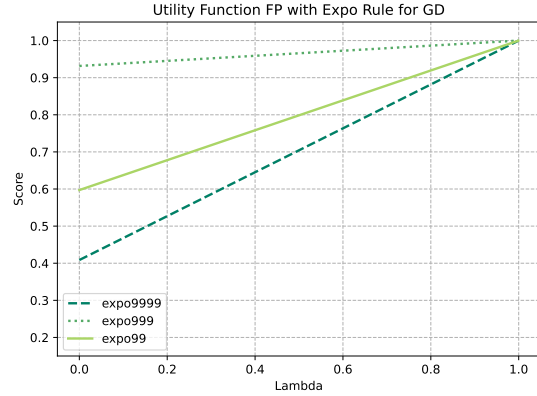
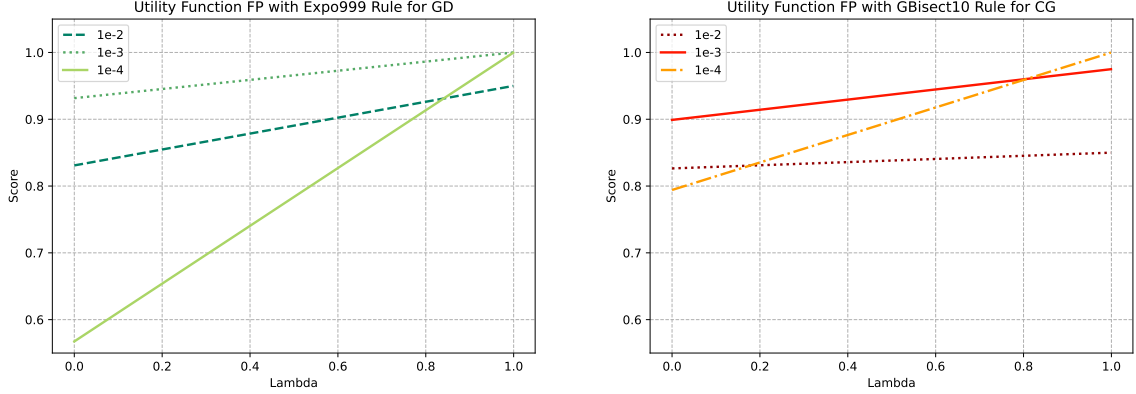


Figure 17: Utility scores of Gradient Descent with the exponential scheduling rule for different values of γ . The score values correspond to 40 structures each and are presented with respect to parameter λ of the utility function u_{FP} and $\gamma \in \{0.99, 0.999, 0.9999\}$.

like before and their utility scores, as found in Figure 18b. It appears that for $\lambda \rightarrow 0$ the smallest step size performs the worst, the largest step size enhances performance but the median displays the best performance. In other words, when a low number of iterations is important, $s = 1e-3$ is the best option. When speed and success rate are equally important, or else, $\lambda = 0.5$, the largest initial step size performs the worst, the smallest initial step size displays a medium performance (with its score being close to the mean of the worse and best score for this λ) and $s = 1e-3$ has the best results. For $\lambda \rightarrow 1$ it is implied that a large number of structures being successfully relaxed is our preference and speed is unimportant, consequently, a small step size is the safest and most reliable option.



(a) Utility scores of Gradient Descent with exponential scheduled step size when $\gamma = 0.999$ and the initial step size is $1e-2$, s_1 , $1e-4$.

(b) Utility scores of Conjugate Gradient with gradient-norm-scheduled step size when $\beta = 10$ and the initial step size is $1e-2$, s_1 , $1e-4$.

Figure 18: **Utility scores of scheduling rules with best performance in low iteration number when the initial step size varies.** The experiments carried out include 40 structures per initial step size value. The methods shown are Gradient Descent with *expo999* and Conjugate Gradient with *gbisect10*, the step scheduling rules that presented the best performance in iteration number in combination with increased success rate.

9.3 Utility Comparison and Analysis

We saw that Conjugate Gradient performs well with a constant step size in terms of speed and some literature review shows that it appears to have nice convergence guarantees, as long as the value of the step size is not very big. This is consistent with our results. The utility scores in the first two columns of the Tables 4a,4b with $\lambda \in [0, 0.5]$ which correspond to constant step sizes confirm that Conjugate Gradient can greatly reduce the number of iterations compared to Gradient Descent. In conjunction with the last column, it is apparent that Conjugate Gradient's utility is the best in all cases with consistently high success rate, thus more robust. We believe that the conjugacy of the produced direction vectors, along with the 'memory' that the updating scheme carries, can more accurately and quickly traverse the PES, hence the results.

Powell [35] has showed that, even with an exact line search, Conjugate Gradient must be combined with a changing step size that tends to zero. In our work we present that a decreasing step size can increase the utility of Conjugate Gradient in terms of speed, in other words, it can reduce the number of its iterations. This is shown by the large increase in its utility score for $\lambda \rightarrow 0$ in rows of Table 4b concerning *gbisect* and *gbisect10* compared to the previous rows, concerning constant step. However, for the rest of the scheduling rules there is small or no increase. Scheduling the step size to be reduced according to an observed large drop in the gradient norm, like with *gbisect10*, increases the algorithm's convergence speed and can in most cases relax a crystal structure successfully. Step size scheduling rules that frequently decrease the step size value, like *bisect* and *gbisect* increase the possibility for successful relaxations, so the utility with $\lambda \rightarrow 1$ is improved, but they do not perform well in terms of speed, thus the utility scores $\lambda \rightarrow 0$ are low.

Table 4: Utility scores for all scheduling rules combined with Gradient Descent and Conjugate Gradient using function u_{FP} . The scores of constant steps, bisect, gbisecte, gbisect10 and 1e-3.expo999 correspond to experiments with 200 structures. The rest correspond to experiments involving 40 structures per method.

(a) The scores of rules expo9999, expo99, 1e-4.expo999 and 1e-2.expo999 correspond to experiments on 40 structures.

method		λ		
		0	0.5	1
const	1e-5	0.448	0.724	1.000
	2.5e-5	0.385	0.448	0.510
	7.75e-5	0.023	0.024	0.025
	1e-4	0.018	0.019	0.020
	1e-3	0.003	0.001	0.000
bisect	1e-3	0.777	0.884	0.990
	1e-3	0.794	0.894	0.995
	1e-3	0.332	0.358	0.385
gbisecte	1e-3	0.409	0.704	1.000
	1e-3	0.567	0.784	1.000
	1e-3	0.926	0.960	0.995
gbisect10	1e-3	0.830	0.89	0.950
	1e-3	0.597	0.798	1.000
	1e-3	0.597	0.798	1.000

(b) The scores of rules 1e-4.gbisecl10 and 1e-2.gbisecl10 correspond to experiments on 40 structures.

method		λ		
		0	0.5	1
const	1e-5	0.448	0.724	1.000
	2.5e-5	0.779	0.890	1.000
	7.75e-5	0.747	0.781	0.815
	1e-4	0.587	0.613	0.640
	1e-3	0.136	0.068	0.000
bisect	1e-3	0.773	0.879	0.985
	1e-3	0.792	0.893	0.995
	1e-3	0.794	0.897	1.000
gbisecl10	1e-4	0.884	0.919	0.955
	1e-3	0.826	0.838	0.850
	1e-2	0.580	0.588	0.595

We have already argued that small steps lead Conjugate Gradient updates to imitate Gradient Descent updates. This also means that its ability to keep information from previous iterations vanishes. Consequently, for Conjugate Gradient to be effective, long leaps on the function domain need to be executed, so that new directions can benefit from past directions visited. This way, the new directions will tend to be more orthogonal to the direction where the minimum lies and Conjugate Gradient can approach it in less steps [4]. The recent work of Renous et al. [9] inspires similar conclusions; it is reported that Conjugate Gradient needs less restarts when the conditions are more lenient.

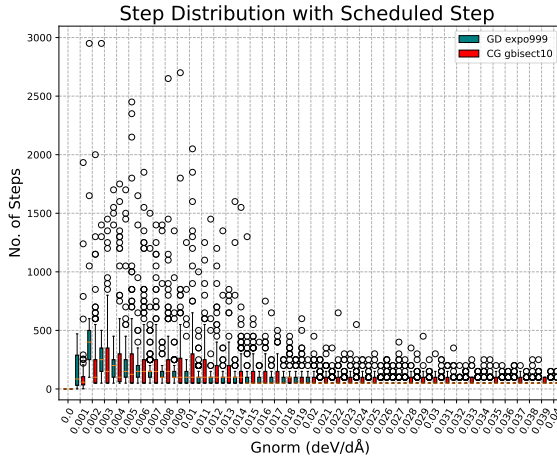


Figure 19: Step number distribution for the best performing scheduled step schemes. The figure depicts the ranges of number of steps to decrease the gradient norm by 0.001 deV/dÅ for Gradient Descent with exponential rule (green) and Conjugate Gradient with gbisecl.

the last iterations the step size is reduced to almost 1e-5, ergo Conjugate Gradient behaves like Gradient Descent and loses its previous convergence properties. The following figure, Figure 19, reveals that Gradient Descent continues to follow the pattern of accumulating iterations towards the end, as with the constant step size. With many steps of continuously reduced step size, it is facilitated to

More specifically, by using the notation of the paper, when $p \geq 0.5$ then the descent condition $g_{k+1}^T d_{k+1} \leq -\sigma \|g_{k+1}\|^{1+p}$ holds more often. This means that, when the RHS is larger in magnitude, restarts happen less frequently. Hence, a higher threshold allows for more iterations to happen and Conjugate Gradient behaves less similarly to Gradient Descent with longer trajectories.

Interestingly, rules like *bisect* and *gbisecl* increase the utility of Gradient Descent in terms of speed and success rate resulting to same or better utility scores for this algorithm compared to Conjugate Gradient. We can observe that Gradient Descent with a scheduling rule that reduces the step size frequently achieves better results. For a constant small decrease in step size, like when using the *expo999* scheduling rule, Gradient Descent achieves optimal results, unless the initial step size, and by extent all consequent step sizes, is too small. Conjugate Gradient's utility enhancement with long steps also justifies why rule *gbisecl10* with this algorithm is not as effective as *expo999* with Gradient Descent; towards

frequently adjust the direction of the search with most corrections realised just before reaching the minimum. Hence, a trajectory consisting of small Gradient Descent advances eventually converges faster.

Another possible explanation of Gradient Descent’s with *expo999* success over Conjugate Gradient is related to the nature of the PES. It has been proved [4] that Gradient Descent’s convergence rate can be higher than Conjugate Gradient’s in strongly convex problems. It would not come as a surprise if the PES neighbourhood in which the minimum lies is defined by a strongly convex function, in which case Gradient Descent can converge faster.

10 Conclusions & Future Work

In this paper we have provided the derivation of a set of crucial equations used in crystal structure prediction. We tested Gradient Descent and Conjugate Gradient with a constant step size and other step size adaptive methods thus providing the foundations for a direct comparison of the two in geometric optimisation of crystals. With these benchmarks in place, we intend to further investigate the algorithms’ performance in relaxation when combined with proper line search, which will be designed to avoid skipping the *true* local minimum of the function. The outcome of the process was that Conjugate Gradient is more trustworthy and efficient, due to its ability to adapt to the PES and mark a steady progress. We confirmed that a scheduled decrease to the step size reduces the iteration number, but there is a trade-off between quick convergence and the number of successful experiments. What is more, we showed that Gradient Descent and Conjugate Gradient benefit from different kinds of step size scheduling rules. We concluded that the values extracted from our constant step experiments provide the best schemes, with Gradient Descent and rule *expo999* displaying optimal results for speed preferences and small constant step sizes displaying optimal results for success rate preferences. In the future, we will include second order methods to our study and extend our analysis to accommodate them accordingly.

11 Acknowledgments

This work has been funded by the Leverhulme Research Centre for Functional Materials Design.

References

- [1] Simulation of electrostatic systems in periodic boundary conditions. II. Equivalence of boundary conditions. *Proceedings of the Royal Society of London. A. Mathematical and Physical Sciences*, 373(1752):57–66, 10 1980.
- [2] János Ángyán, John Dobson, Georg Jansen, and Tim Gould. Dispersion Energies via Division Into Atoms or Larger Units. In *London Dispersion Forces in Molecules, Solids and Nano-structures: An Introduction to Physical Models and Computational Methods*, chapter 8, pages 200–236. Royal Society of Chemistry, 4 2020.
- [3] Erik Bitzek, Pekka Koskinen, Franz Gähler, Michael Moseler, and Peter Gumbsch. Structural relaxation made simple. *Physical Review Letters*, 97(17):1–4, 2006.
- [4] Charles Blair. Problem Complexity and Method Efficiency in Optimization (A. S. Nemirovsky and D. B. Yudin). *SIAM Review*, 27(2):264–265, 8 2006.
- [5] Daniel Born and Johannes Kästner. Geometry Optimization in Internal Coordinates Based on Gaussian Process Regression: Comparison of Two Approaches. *Journal of Chemical Theory and Computation*, 17(9):5955–5967, 9 2021.
- [6] Charles L. Brooks. Computer simulation of liquids. *Journal of Solution Chemistry* 1989 18:1, 18(1):99–99, 1 1989.
- [7] Amyand David Buckingham. Theory of long-range dispersion forces. *Discussions of the Faraday Society*, 40(0):232–238, 1 1965.

- [8] C. R. A. Catlow and W. C. Mackrodt. *Theory of simulation methods for lattice and defect energy calculations in crystals*, pages 1–20. Springer Berlin Heidelberg, Berlin, Heidelberg, 1982.
- [9] Rémi Chan-Renous-Legoubin and Clément W. Royer. A nonlinear conjugate gradient method with complexity guarantees and its application to nonconvex regression. *EURO Journal on Computational Optimization*, 10:100044, 1 2022.
- [10] C. Collins, G. R. Darling, and M. J. Rosseinsky. The Flexible Unit Structure Engine (FUSE) for probe structure-based composition prediction. *Faraday Discussions*, 211(0):117–131, 10 2018.
- [11] Stephen H. Crandall, Norman C. Dahl, and Ellis H. Dill. An Introduction to the Mechanics of Solids. In *Physics Today*, volume 13, pages 201–254, 1960.
- [12] Yu Hong Dai. Convergence of conjugate gradient methods with constant stepsizes. *Optimization Methods and Software*, 26(6):895–909, 12 2010.
- [13] Estefanía Garijo Del Río, Jens Jørgen Mortensen, and Karsten Wedel Jacobsen. Local Bayesian optimizer for atomic structures. *Physical Review B*, 100(10), 9 2019.
- [14] Zhen Fan, Zhixin Sun, Guangyong Jin, and Chao Xin. Effect of strain on the band structure and optical properties of Na₂Bi₂(SeO₃)₃F₂. *Computational Materials Science*, 218:111962, 2 2023.
- [15] Scott E. Feller, Richard W. Pastor, Atipat Rojnuckarin, Stephen Bogusz, and Bernard R. Brooks. Effect of Electrostatic Force Truncation on Interfacial and Transport Properties of Water. *Journal of Physical Chemistry*, 100(42):17011–17020, 1996.
- [16] Daan Frenkel and Berend Smit. *Understanding molecular simulation: From algorithms to applications*. Academic Press, Incorporated, 2 edition, 1996.
- [17] Julian D. Gale and Andrew L. Rohl. The General Utility Lattice Program (GULP). *Molecular Simulation*, 29(5):291–341, 2003.
- [18] Devon R. Graham, Kevin Leyton-Brown, and Tim Roughgarden. Formalizing Preferences Over Runtime Distributions, 2022.
- [19] L Grippo and S Lucidi. A globally convergent version of the Polak-Ribiere conjugate gradient method. *Mathematical Programming*, 78:375–391, 1997.
- [20] S. R. Hall, F. H. Allen, and I. D. Brown. The crystallographic information file (CIF): a new standard archive file for crystallography. *Acta Crystallographica Section A*, 47(6):655–685, 11 1991.
- [21] Zachary C. Holden, Bhaskar Rana, and John M. Herbert. Analytic gradient for the QM/MM-Ewald method using charges derived from the electrostatic potential: Theory, implementation, and application to ab initio molecular dynamics simulation of the aqueous electron. *Journal of Chemical Physics*, 150(14):144115, 4 2019.
- [22] Philippe H. Hünenberger and Wilfred F. Van Gunsteren. Alternative schemes for the inclusion of a reaction-field correction into molecular dynamics simulations: Influence on the simulated energetic, structural, and dielectric properties of liquid water. *The Journal of Chemical Physics*, 108(15):6117, 8 1998.
- [23] Pieter J. In ’t Veld, Ahmed E. Ismail, and Gary S. Grest. Application of Ewald summations to long-range dispersion forces. *The Journal of Chemical Physics*, 127(14):144711, 10 2007.
- [24] R. A. Jackson and C. R.A. Catlow. Computer Simulation Studies of Zeolite Structure. *Molecular Simulation*, 1(4):207–224, 1988.
- [25] Ask Hjorth Larsen, Jens Jørgen Mortensen, Jakob Blomqvist, Ivano E Castelli, Rune Christensen, Marcin Dułak, Jesper Friis, Michael N Groves, Bjørk Hammer, Cory Hargus, Eric D Hermes, Paul C Jennings, Peter Bjerre Jensen, James Kermode, John R Kitchin, Esben Leonhard Kolsbjerg, Joseph Kubal, Kristen Kaasbjerg, Steen Lysgaard, Jón Bergmann Maronsson, Tristan Maxson, Thomas Olsen, Lars Pastewka, Andrew Peterson, Carsten Rostgaard, Jakob

- Schiøtz, Ole Schütt, Mikkel Strange, Kristian S Thygesen, Tejs Vegge, Lasse Vilhelmsen, Michael Walter, Zhenhua Zeng, and Karsten W Jacobsen. The atomic simulation environment—a python library for working with atoms. *Journal of Physics: Condensed Matter*, 29(27):273002, 6 2017.
- [26] Ask Hjorth Larsen, Jens Jørgen Mortensen, Jakob Blomqvist, Ivano E Castelli, Rune Christensen, Marcin Dułak, Jesper Friis, Michael N Groves, Bjørk Hammer, Cory Hargus, Eric D Hermes, Paul C Jennings, Peter Bjerre Jensen, James Kermode, John R Kitchin, Esben Leonhard Kolsbjerg, Joseph Kubal, Kristen Kaasbjerg, Steen Lysgaard, Jón Bergmann Maronsson, Tristan Maxson, Thomas Olsen, Lars Pastewka, Andrew Peterson, Carsten Rostgaard, Jakob Schiøtz, Ole Schütt, Mikkel Strange, Kristian S Thygesen, Tejs Vegge, Lasse Vilhelmsen, Michael Walter, Zhenhua Zeng, and Karsten W Jacobsen. Fast parallel algorithms for short-range molecular dynamics. *J Comp Phys*, 1995.
 - [27] Hark Lee and Wei Cai. Ewald Summation for Coulomb Interactions in a Periodic Supercell. 2009.
 - [28] Per Linsew and Hans C. Andersen. Truncation of Coulombic interactions in computer simulations of liquids. *The Journal of Chemical Physics*, 85(5):3027–3041, 1986.
 - [29] D. R. Mason. Faster neighbour list generation using a novel lattice vector representation. *Computer Physics Communications*, 170(1):31–41, 7 2005.
 - [30] Artem Oganov, Chris Pickard, Qiang Zhu, and Richard Needs. Structure prediction drives materials discovery. *Nature Reviews Materials*, 4, 04 2019.
 - [31] Philomena Oluwatosin Olaniyan, Md-Masuduzzaman Nadim, and Mahamud Subir. Detection and binding interactions of pharmaceutical contaminants using quartz crystal microbalance – Role of adsorbate structure and surface functional group on adsorption. *Chemosphere*, 311:137075, 1 2023.
 - [32] M. C. Payne, M. P. Teter, D. C. Allan, T. A. Arias, and J. D. Joannopoulos. Iterative minimization techniques for ab initio total-energy calculations: molecular dynamics and conjugate gradients. *Rev. Mod. Phys.*, 64:1045–1097, 10 1992.
 - [33] Chris J. Pickard. Real space pairwise electrostatic summation in a uniform neutralising background. *Phys. Rev. Mater.*, 2, 1 2018.
 - [34] E Polak and G Ribiere. Note sur la convergence de méthodes de directions conjuguées. *Revue française d’informatique et de recherche opérationnelle, série rouge*, pages 35–43, 1969.
 - [35] M. J. D. Powell. Nonconvex minimization calculations and the conjugate gradient method. In *Numerical Analysis*, volume 1066, pages 122–141. Springer, Berlin, Heidelberg, 1984.
 - [36] M. J.D. Powell. Restart procedures for the conjugate gradient method. *Mathematical Programming*, 12(1):241–254, 12 1977.
 - [37] H. Bernhard Schlegel. Geometry optimization. *WIREs Computational Molecular Science*, 1(5):790–809, 9 2011.
 - [38] J. L. Schlenker, G. V. Gibbs, and M. B. Boisen. Strain-tensor components expressed in terms of lattice parameters. *Acta Crystallographica Section A*, 34(1):52–54, 1978.
 - [39] Benjamin Stamm, Louis Lagardère, Étienne Polack, Yvon Maday, and Jean-Philip Piquemal. A coherent derivation of the Ewald summation for arbitrary orders of multipoles: The self-terms. *The Journal of Chemical Physics*, 149(12), 5 2018.
 - [40] Peter J Steinbach and Bernard R Brooks. New Spherical-Cutoff Methods for Long-Range Forces in Macromolecular Simulation. *Journal of Computational Chemistry*, 15(7):667–683, 1994.
 - [41] Dana Taha, Mohammed Salih, and Bawar Mohammed Faraj. Comparison Between Steepest Descent Method and Conjugate Gradient Method by Using Matlab. *Journal of Studies in Science and Engineering*, 2021(1):20, 2021.
 - [42] Abdunour Y Toukmaji and John A Board. Ewald summation techniques in perspective: a survey. Technical report, 1996.

- [43] D. Wang, J. Liu, J. Zhang, S. Raza, X. Chen, and C. L. Jia. Ewald summation for ferroelectric perovskites with charges and dipoles. *Computational Materials Science*, pages 314–321, 11 2019.
- [44] Chenglong Zhang, Mingcan Zhao, Chaofeng Hou, and Wei Ge. A multilevel-skin neighbor list algorithm for molecular dynamics simulation. *Computer Physics Communications*, 222:59–69, 1 2018.

A Appendix

A.1 Proofs related to the energy function potential

Proof of Propositions 1 and 2 (See page 5)

The following derivations involving the handling of the ions' potential field have been heavily inspired by the work of H.Lee and W.Cai [27].

Proposition 1. *Expanding with Ewald summation, the short range interactions of the Coulomb potential summation are calculated as:*

$$\Phi_{Coul}^S(R, L) = \frac{k_e}{2} \sum_n \sum_{i=1}^N \sum_{j=1}^{N'} \frac{q_i q_j}{\|r_i + L_n - r_j\|} \operatorname{erfc}(\alpha \|r_i + L_n - r_j\|) \quad (4)$$

Proposition 2. *Expanding with Ewald summation, the long range interactions of the Coulomb potential summation are calculated as:*

$$\Phi_{Coul}^L(R, L) = \frac{k_e}{2} \sum_n \sum_{i=1}^N \sum_{j=1}^{N'} \frac{k_e}{2} \frac{q_i q_j}{\|r_i + L_n - r_j\|} \operatorname{erf}\left(\frac{\|r_i + L_n - r_j\|}{\sqrt{2}\sigma}\right) \quad (5)$$

Proof. For the proof of Propositions 1 and 2, we will be referring to the electric potential field (ϕ) and the charge density distribution (ρ) of a point charge (q_j) at position r :

$$\begin{aligned} \phi_j(r) &= \frac{1}{4\pi\epsilon_0} \frac{q_j}{\|r - r_j\|}, \quad r, r_j \in \mathbb{R}^3 \\ \rho_j(r) &= q_j \delta(r - r_j), \quad r, r_j \in \mathbb{R}^3 \end{aligned}$$

where ϵ_0 is the vacuum permittivity and δ is the Dirac delta function. The potential field at position $r = r_i + L_n$ generated by all ions with positions r_j , $j \in [N]$, $j \neq i$ is

$$\phi_j(r_i) = \frac{1}{4\pi\epsilon_0} \sum_n \sum_{j=1}^{N'} \frac{q_j}{\|r_i + L_n - r_j\|}, \quad r_i, r_j \in \mathbb{R}^3 \quad (28)$$

which gives the conditionally convergent energy potential

$$\Phi_{Coul}(R, L) = \frac{1}{4\pi\epsilon_0} \sum_{i=1}^N \phi_j(r_i)$$

The following techniques for the mentioned derivations are heavily based on the work of Lee and Cai [27]. We can consider that the charge distribution of an ion extends in space as a Gaussian distribution

$$G_\sigma(r) = \frac{1}{(2\pi\sigma^2)^{3/2}} \exp\left(-\frac{r^2}{2\sigma^2}\right), \quad r \in \mathbb{R}^3 \quad (29)$$

Moreover, it is convenient to acknowledge that the delta function is actually the limit of the Gaussian distribution G_σ with the standard deviation approaching zero $\sigma \rightarrow 0$

$$\lim_{\sigma \rightarrow 0} G_\sigma(r) = \delta(r)$$

Then, we can discriminate between interactions close to charge q_j and interactions in distance from it by adding and subtracting $G_\sigma(r - r_i)$ to charge density distribution

$$\begin{aligned} \rho_j(r) &= \rho_j^S(r) + \rho_j^L(r) \\ \rho_j^S(r) &= q_j \delta(r - r_j) - q_j G_\sigma(r - r_j) \\ \rho_j^L(r) &= q_j G_\sigma(r - r_j) \end{aligned} \quad (30)$$

The charge density distribution is connected to the potential field ϕ_i through Poisson's equation. When it takes the form of a Gaussian distribution, we have

$$\nabla^2 \phi_j(r) = -\frac{\rho_j(r)}{\epsilon_0} = -\frac{q_j G_\sigma(r - r_j)}{\epsilon_0} \quad (31)$$

Now, since G_σ is a function with only one independent variable r , we can express Poisson's equation in spherical coordinates. To be more specific, the Laplacian operator in terms of spherical coordinates appears as

$$\nabla^2 = \frac{1}{r^2} \frac{\partial}{\partial r} \left(r^2 \frac{\partial}{\partial r} \right) + \frac{1}{r^2 \sin \theta} \frac{\partial}{\partial \theta} \left(\sin \theta \frac{\partial}{\partial \theta} \right) + \frac{1}{r^2 \sin^2 \theta} \frac{\partial^2}{\partial \phi^2} \quad (32)$$

We define as $\bar{\phi}_j(r)$, $\bar{G}_\sigma(r)$ the functions that correspond to $\phi_j(r)$, $G_\sigma(r)$ with the difference that the independent variable becomes the distance $r = \|r - r_j\|$ since it is the only quantity affected from the vector positions r . Because of spherical symmetry and after some operations

$$\begin{aligned} \frac{1}{r^2} \frac{\partial}{\partial r} \left(r^2 \frac{\partial}{\partial r} \bar{\phi}_j(r) \right) &= \frac{1}{r^2} \left(r^2 \frac{\partial^2 \bar{\phi}_j(r)}{\partial r^2} + 2r \frac{\partial \bar{\phi}_j(r)}{\partial r} \right) \\ &= \frac{\partial^2 \bar{\phi}_j(r)}{\partial r^2} + \frac{2}{r} \frac{\partial \bar{\phi}_j(r)}{\partial r} \\ &= \frac{1}{r} \frac{\partial^2}{\partial r^2} (r \bar{\phi}_j(r)) \end{aligned}$$

we get the following simple equation from Equation (31)

$$\frac{1}{r} \frac{\partial^2}{\partial r^2} (r \bar{\phi}_j(r)) = -\frac{\bar{G}_\sigma(r)}{\epsilon_0}$$

By integration we arrive to

$$\begin{aligned} r \bar{\phi}_j(r) &= \frac{\sigma}{\epsilon_0} \int_0^r \bar{G}_\sigma(r) dr \\ &= \frac{\sigma}{\epsilon_0} \frac{1}{(2\pi\sigma^2)^{3/2}} \sqrt{\frac{\pi}{2}} \sigma \operatorname{erf} \left(\frac{r}{\sqrt{2}\sigma} \right) \\ \Rightarrow \bar{\phi}_j(r) &= \frac{1}{4\pi\epsilon_0 r} \operatorname{erf} \left(\frac{r}{\sqrt{2}\sigma} \right) \end{aligned} \quad (33)$$

in which $\operatorname{erf}(z) = \frac{2}{\sqrt{\pi}} \int_0^z \exp(-t^2) dt$ is the error function. After the split of charge density distribution in Equation (30), the potential field caused by ion j is correspondingly split into

$$\phi_j(r) = \phi_j^S(r) + \phi_j^L(r) \quad (34)$$

$$\phi_j^S(r) = \frac{1}{4\pi\epsilon_0} \frac{q_j}{\|r - r_j\|} \left[1 - \operatorname{erf} \left(\frac{\|r - r_j\|}{\sqrt{2}\sigma} \right) \right] = \frac{1}{4\pi\epsilon_0} \frac{q_j}{\|r - r_j\|} \operatorname{erfc} \left(\frac{\|r - r_j\|}{\sqrt{2}\sigma} \right) \quad (35)$$

$$\phi_j^L(r) = \frac{1}{4\pi\epsilon_0} \frac{q_j}{\|r - r_j\|} \operatorname{erf} \left(\frac{\|r - r_j\|}{\sqrt{2}\sigma} \right) \quad (36)$$

Finally, we can calculate the electrostatic energy caused by short ranged interactions using Equation (35). This range is determined by the term $\operatorname{erfc}()$, which truncates the summation for long distances and converges absolutely

$$\begin{aligned} \Phi_{Coul}^S(R, L) &= \frac{k_e}{2} \sum_{i=1}^N \phi_j^S(r) \\ &= \frac{k_e}{2} \sum_n \sum_{i=1}^N \sum_{j=1}^{N'} \frac{q_i q_j}{\|r_i + L_n - r_j\|} \operatorname{erfc}(\alpha \|r_i + L_n - r_j\|) \end{aligned} \quad (37)$$

with $\alpha = \frac{1}{\sqrt{2}\sigma}$ and $k_e = \frac{1}{4\pi\epsilon_0}$. In the same fashion, for long ranged interactions we have

$$\begin{aligned}\Phi_{Coul}^L(R, L) &= \frac{k_e}{2} \sum_n \sum_{i=1}^N \sum_{j=1}^N \phi_j^L(r) \\ &= \frac{k_e}{2} \sum_n \sum_{i=1}^N \sum_{j=1}^N \frac{q_i q_j}{\|r_i + L_n - r_j\|} \operatorname{erf}\left(\frac{\|r_i + L_n - r_j\|}{\sqrt{2}\sigma}\right)\end{aligned}\quad (38)$$

□

Proof of Proposition 3 (See page 6)

The proof of this proposition has been inspired by the techniques presented by D. Wang et al. [43].

Proposition 3. *The form of the reciprocal term of the Coulomb potential with fast convergence is:*

$$\Phi_{Coul}^L(r, L) = \frac{4\pi}{|V|||G_m||^2} \exp\left(-\frac{||G_m||^2}{4\alpha^2}\right) \exp(iG_m r) \quad (6)$$

Proof. Let us define a function

$$f(r_i - r_j) = f(r) = \sum_n \frac{1}{\|r + L_n\|} \operatorname{erf}(\alpha\|r + L_n\|) = f(r + L_n) \quad (39)$$

according to Equation (36). The function f is periodic for intervals equal to the unit cell lengths defined by the three linearly independent vectors $L_n = n_1 l_1 + n_2 l_2 + n_3 l_3$. We can expand f as a Fourier series of exponential functions

$$f(r) = \sum_{m \in \mathbb{Z}^3} h(m) \exp(iG_m r) \quad (40)$$

in which we have used the reciprocal vectors' property $k_i \cdot l_j = 2\pi\delta_{ij}$, $i, j \in \{1, 2, 3\}$ where δ_{ij} is the Kronecker delta, and $h(m)$ are Fourier coefficients. It follows from Equation (39) that the multipliers of the series of Equation (40) are

$$\begin{aligned}h(m) &= \frac{1}{|V|} \iiint_V f(r) \exp(-iG_m r) d^3r \\ &= \frac{1}{|V|} \iiint_V \sum_n \frac{1}{\|r + L_n\|} \operatorname{erf}\left(\frac{\|r + L_n\|}{\sqrt{2}\sigma}\right) \exp(-iG_m r) d^3r,\end{aligned}$$

where V is the unit cell, and $|V|$ is its the volume. Following the derivation of Wang et al. [43] we change r into spherical coordinates ρ, θ, ϕ , which describe vector's r length, angle from x-axis in the xy-plane and angle from z-axis respectively. We can assume that the z-axis is parallel to G_m as follows

$$\begin{aligned}h(m) &= \frac{1}{|V|} \iiint_V f(r) \exp(-iG_m r) d^3r \\ &= \frac{1}{|V|} \int_0^{2\pi} \int_0^\pi \int_0^\infty \frac{1}{\rho} \operatorname{erf}\left(\frac{\rho}{\sqrt{2}\sigma}\right) \exp(-i||G_m||\rho \cos(\phi)) d\rho (\rho d\phi) (\rho \sin\phi d\theta) \\ &= \frac{2\pi}{|V|} \int_0^\infty \rho \cdot \operatorname{erf}\left(\frac{\rho}{\sqrt{2}\sigma}\right) \int_0^\pi \exp(-i||G_m||\rho \cos(\phi)) d\phi d\rho \\ &= \frac{4\pi}{|V|||G_m||} \int_0^\infty \sin(||G_m||\rho) \operatorname{erf}\left(\frac{\rho}{\sqrt{2}\sigma}\right) d\rho\end{aligned}$$

Next, we perform a variable change to replace $||G_m||\rho$ with some x and $\frac{1}{\sqrt{2}\sigma}$ with α

$$\begin{aligned}h(m) &= \frac{4\pi}{|V|||G_m||^2} \int_0^\infty \sin(x) \operatorname{erf}\left(\frac{\alpha x}{||G_m||}\right) dx \\ &= \frac{4\pi}{|V|||G_m||^2} \exp\left(-\frac{||G_m||^2}{4\alpha^2}\right)\end{aligned}\quad (41)$$

□

Here, the employment of some Gaussian charge distribution with standard deviation σ serves as the means to embed convergence factors that ultimately convert the Coulombic energy potential function to an absolutely convergent summation.

Proof of Proposition 4 (See page 6)

Proposition 4. *The fast convergent Coulomb potential for long range interactions in a crystal structure is given by the function*

$$\Phi_{Coul}^L(r, L) = \frac{2\pi k_e}{V \|G_m\|^2} \sum_{G_m \neq 0} \sum_{i=1}^N \sum_{j=1}^N q_i q_j \exp\left(-\frac{\|G_m\|^2}{4\alpha^2}\right) \cos(G_m r) \quad (7)$$

Proof. Let f be defined as in the proof of Proposition 3. Let us also define a real function $g : \mathbb{R}^3 \rightarrow \mathbb{R}$. We can express any vector r using the coordinate system constructed by the lattice vectors, such that

$$r = x_1 \frac{l_1}{\|l_1\|} + x_2 \frac{l_2}{\|l_2\|} + x_3 \frac{l_3}{\|l_3\|} \quad (42)$$

and then $f(r) = g(x_1, x_2, x_3)$. Hence, the periodicity of f is now expressed through g with

$$g(x_1, x_2, x_3) = g(x_1 + l'_1, x_2 + l'_2, x_3 + l'_3), \text{ where } l'_j \in \{0, \|l_j\|\}, \text{ for } j \in \{1, 2, 3\}$$

Then, g can be expanded to a Fourier series using a set of orthonormal functions. Let $u_t = \frac{2\pi m_t}{\|l_t\|}$, $t \in \{1, 2, 3\}$

$$\begin{aligned} g(x_1, x_2, x_3) = & \sum_{m_1=0}^{\infty} \sum_{m_2=0}^{\infty} \sum_{m_3=0}^{\infty} a_m \cos(u_1 x_1) \cos(u_2 x_2) \cos(u_3 x_3) + \\ & b_m \sin(u_1 x_1) \cos(u_2 x_2) \cos(u_3 x_3) + c_m \cos(u_1 x_1) \sin(u_2 x_2) \cos(u_3 x_3) + \\ & d_m \sin(u_1 x_1) \sin(u_2 x_2) \cos(u_3 x_3) + \alpha_m \cos(u_1 x_1) \cos(u_2 x_2) \sin(u_3 x_3) + \\ & \beta_m \sin(u_1 x_1) \cos(u_2 x_2) \sin(u_3 x_3) + \gamma_m \cos(u_1 x_1) \sin(u_2 x_2) \sin(u_3 x_3) + \\ & \delta_m \sin(u_1 x_1) \sin(u_2 x_2) \sin(u_3 x_3) \end{aligned} \quad (43)$$

with multipliers indexed by a triplet $m = (m_1, m_2, m_3)$, $m_1, m_2, m_3 \in \mathbb{Z}$. We can replace all terms with Euler's identity

$$\begin{aligned} \cos(u_t x_t) &= \frac{1}{2} [\exp(iu_t x_t) + \exp(-iu_t x_t)], \quad t \in \{1, 2, 3\} \\ \sin(u_t x_t) &= \frac{1}{2i} [\exp(iu_t x_t) - \exp(-iu_t x_t)], \quad t \in \{1, 2, 3\} \end{aligned}$$

and get a series with terms comprising product combinations $\exp(\pm iu_1 x_1) \exp(\pm iu_2 x_2) \exp(\pm iu_3 x_3) = \exp[i(\pm u_1 x_1 \pm u_2 x_2 \pm u_3 x_3)]$. We can regroup the multipliers $a_m, b_m, c_m, d_m, \alpha_m, \beta_m, \gamma_m, \delta_m$ to accompany each unique exponential term of the form $\exp[i(\pm u_1 x_1 \pm u_2 x_2 \pm u_3 x_3)]$ and get new multipliers of the form $\eta_{mj} = \frac{1}{8}(\pm a_m \pm ib_m \pm ic_m \pm d_m \pm i\alpha_m \pm \beta_m \pm \gamma_m \pm i\delta_m)$. Let us define the set, Θ , of all such coefficients, $\Theta = \{\frac{1}{8}(\oplus a_m \oplus ib_m \oplus ic_m \oplus d_m \oplus i\alpha_m \oplus \beta_m \oplus \gamma_m \oplus i\delta_m) : \oplus \in \{+, -\}\}$, so that

$$\begin{aligned} g(x_1, x_2, x_3) = & \sum_{m_1, m_2, m_3 \in \mathbb{N}} \{ \eta_{m1}(m) \exp[i(u_1 x_1 + u_2 x_2 + u_3 x_3)] + \\ & \eta_{m2}(m) \exp[i(u_1 x_1 - u_2 x_2 + u_3 x_3)] + \eta_{m3}(m) \exp[i(-u_1 x_1 + u_2 x_2 + u_3 x_3)] + \\ & \eta_{m4}(m) \exp[i(-u_1 x_1 - u_2 x_2 + u_3 x_3)] + \eta_{m5}(m) \exp[i(u_1 x_1 + u_2 x_2 - u_3 x_3)] + \\ & \eta_{m6}(m) \exp[i(u_1 x_1 - u_2 x_2 - u_3 x_3)] + \eta_{m7}(m) \exp[i(-u_1 x_1 + u_2 x_2 - u_3 x_3)] + \\ & \eta_{m8}(m) \exp[i(-u_1 x_1 - u_2 x_2 - u_3 x_3)] \} \end{aligned}$$

where $\eta_{mj}(m) \in \Theta$, are appropriate coefficients for $j \in \{1, 2, \dots, 8\}$. We observe that

$$\begin{aligned} g(x_1, x_2, x_3) = & \eta_{m1} \exp[i(u_1 x_1 + u_2 x_2 + u_3 x_3)] + [\eta_{m1}]^* \exp[-i(u_1 x_1 + u_2 x_2 + u_3 x_3)] + \\ & \eta_{m2} \exp[i(u_1 x_1 - u_2 x_2 + u_3 x_3)] + [\eta_{m2}]^* \exp[-i(u_1 x_1 - u_2 x_2 + u_3 x_3)] + \\ & \eta_{m3} \exp[i(-u_1 x_1 + u_2 x_2 + u_3 x_3)] + [\eta_{m3}]^* \exp[-i(-u_1 x_1 + u_2 x_2 + u_3 x_3)] + \\ & \eta_{m6} \exp[i(u_1 x_1 + u_2 x_2 - u_3 x_3)] + [\eta_{m6}]^* \exp[-i(u_1 x_1 + u_2 x_2 - u_3 x_3)] \end{aligned} \quad (44)$$

As a result of Equations 42, 40, we have that $\exp(iG_m r) = \exp[i(u_1 x_1 + u_2 x_2 + u_3 x_3)]$ and

$$\begin{aligned}
f(r) &= g(x_1, x_2, x_3) = \\
&\sum_{m \in \mathbb{N}^3} h(m_1, m_2, m_3) \exp[i(m_1, m_2, m_3)kr] + \sum_{m \in \mathbb{N}^3} h[-(m_1, m_2, m_3)] \exp[-i(m_1, m_2, m_3)kr] + \\
&\sum_{m \in \mathbb{N}^3} h(m_1, -m_2, m_3) \exp[i(m_1, -m_2, m_3)kr] + \sum_{m \in \mathbb{N}^3} h[-(m_1, -m_2, m_3)] \exp[-i(m_1, -m_2, m_3)kr] + \\
&\sum_{m \in \mathbb{N}^3} h(-m_1, m_2, m_3) \exp[i(-m_1, m_2, m_3)kr] + \sum_{m \in \mathbb{N}^3} h[-(-m_1, m_2, m_3)] \exp[-i(-m_1, m_2, m_3)kr] + \\
&\sum_{m \in \mathbb{N}^3} h(m_1, m_2, -m_3) \exp[i(m_1, m_2, -m_3)kr] + \sum_{m \in \mathbb{N}^3} h[-(m_1, m_2, -m_3)] \exp[-i(m_1, m_2, -m_3)kr]
\end{aligned} \tag{45}$$

The uniqueness of the multipliers of trigonometric series and Equations 44, 45 show that the multipliers of the exponential and cosine-sine series are connected through the following relation

$$h(m) = h(m_1, m_2, m_3) = \frac{1}{8}(a_m - ib_m - ic_m - d_m - i\alpha_m - \beta_m - \gamma_m + i\delta_m) = \eta_{m1} \tag{46}$$

in accordance to the sign of each of the integers m_1, m_2, m_3 . As a consequence of the orthogonality of the functions in Equation (43), we can exactly calculate its multipliers. Let $m'_1, m'_2, m'_3 \in \mathbb{Z}$ and space $\mathcal{V} = [-\frac{\|l_1\|}{2}, \frac{\|l_1\|}{2}] \times [-\frac{\|l_2\|}{2}, \frac{\|l_2\|}{2}] \times [-\frac{\|l_3\|}{2}, \frac{\|l_3\|}{2}]$ define a unit cell volume image. In order to obtain the value of multiplier a_m , we take advantage of the orthogonality of the summation terms and multiply both sides of Equation (43) with $\cos(\frac{2\pi m'_1}{\|l_1\|}x_1) \cos(\frac{2\pi m'_2}{\|l_2\|}x_2) \cos(\frac{2\pi m'_3}{\|l_3\|}x_3)$ and integrate over \mathcal{V} . This results into eliminating any terms with a multiplier different from a_m and

$$\begin{aligned}
&\int_{-\frac{\|l_1\|}{2}}^{\frac{\|l_1\|}{2}} \int_{-\frac{\|l_2\|}{2}}^{\frac{\|l_2\|}{2}} \int_{-\frac{\|l_3\|}{2}}^{\frac{\|l_3\|}{2}} g(x_1, x_2, x_3) \cos(\frac{2\pi m'_1}{\|l_1\|}x_1) \cos(\frac{2\pi m'_2}{\|l_2\|}x_2) \cos(\frac{2\pi m'_3}{\|l_3\|}x_3) dx_1 dx_2 dx_3 = \\
&\int_{-\frac{\|l_1\|}{2}}^{\frac{\|l_1\|}{2}} \int_{-\frac{\|l_2\|}{2}}^{\frac{\|l_2\|}{2}} \int_{-\frac{\|l_3\|}{2}}^{\frac{\|l_3\|}{2}} a_m [\cos(\frac{2\pi m_1}{\|l_1\|}x_1) \cos(\frac{2\pi m_2}{\|l_2\|}x_2) \cos(\frac{2\pi m_3}{\|l_3\|}x_3)] \cdot \\
&\quad [\cos(\frac{2\pi m'_1}{\|l_1\|}x_1) \cos(\frac{2\pi m'_2}{\|l_2\|}x_2) \cos(\frac{2\pi m'_3}{\|l_3\|}x_3)] dx_1 dx_2 dx_3 + 0 = \\
&\int_{-\frac{\|l_1\|}{2}}^{\frac{\|l_1\|}{2}} \int_{-\frac{\|l_2\|}{2}}^{\frac{\|l_2\|}{2}} \int_{-\frac{\|l_3\|}{2}}^{\frac{\|l_3\|}{2}} \frac{a_m}{8} \{ \cos[\frac{2\pi(m_1 - m'_1)}{\|l_1\|}x_1] + \cos[\frac{2\pi(m_1 + m'_1)}{\|l_1\|}x_1] \} \cdot \\
&\quad \{ \cos[\frac{2\pi(m_2 - m'_2)}{\|l_2\|}x_2] + \cos[\frac{2\pi(m_2 + m'_2)}{\|l_2\|}x_2] \} \cdot \\
&\quad \{ \cos[\frac{2\pi(m_3 - m'_3)}{\|l_3\|}x_3] + \cos[\frac{2\pi(m_3 + m'_3)}{\|l_3\|}x_3] \} dx_1 dx_2 dx_3 = \\
&\quad \frac{1}{8} a_m \delta_{m_1 m'_1} \delta_{m_2 m'_2} \delta_{m_3 m'_3} \|l_1\| \cdot \|l_2\| \cdot \|l_3\|
\end{aligned}$$

leading to

$$a_m = \frac{8}{V} \int_{-\frac{\|l_1\|}{2}}^{\frac{\|l_1\|}{2}} \int_{-\frac{\|l_2\|}{2}}^{\frac{\|l_2\|}{2}} \int_{-\frac{\|l_3\|}{2}}^{\frac{\|l_3\|}{2}} g(x_1, x_2, x_3) \cos(\frac{2\pi m_1}{\|l_1\|}x_1) \cos(\frac{2\pi m_2}{\|l_2\|}x_2) \cos(\frac{2\pi m_3}{\|l_3\|}x_3) dx_1 dx_2 dx_3$$

The multipliers d_m, β_m, γ_m are calculated in the same fashion. However, for b_m we find the following

$$\begin{aligned}
b_m &= \int_{-\frac{\|l_1\|}{2}}^{\frac{\|l_1\|}{2}} \int_{-\frac{\|l_2\|}{2}}^{\frac{\|l_2\|}{2}} \int_{-\frac{\|l_3\|}{2}}^{\frac{\|l_3\|}{2}} g(x_1, x_2, x_3) \sin(\frac{2\pi m_1}{\|l_1\|}x_1) \cos(\frac{2\pi m_2}{\|l_2\|}x_2) \cos(\frac{2\pi m_3}{\|l_3\|}x_3) dx_1 dx_2 dx_3 \\
&= \int_{-\frac{\|l_1\|}{2}}^0 \int_{-\frac{\|l_2\|}{2}}^0 \int_{-\frac{\|l_3\|}{2}}^0 g(x_1, x_2, x_3) \sin(\frac{2\pi m_1}{\|l_1\|}x_1) \cos(\frac{2\pi m_2}{\|l_2\|}x_2) \cos(\frac{2\pi m_3}{\|l_3\|}x_3) dx_1 dx_2 dx_3 + \\
&\quad \int_0^{\frac{\|l_1\|}{2}} \int_0^{\frac{\|l_2\|}{2}} \int_0^{\frac{\|l_3\|}{2}} g(x_1, x_2, x_3) \sin(\frac{2\pi m_1}{\|l_1\|}x_1) \cos(\frac{2\pi m_2}{\|l_2\|}x_2) \cos(\frac{2\pi m_3}{\|l_3\|}x_3) dx_1 dx_2 dx_3
\end{aligned}$$

with a change of variables $-u = x_1$, $-v = x_2$, $-w = x_3$ in the first triple integral

$$b_m = \int_0^{\frac{\|l_1\|}{2}} \int_0^{\frac{\|l_2\|}{2}} \int_0^{\frac{\|l_3\|}{2}} g(-u, -v, -w) \sin\left(-\frac{2\pi m_1}{\|l_1\|}u\right) \cos\left(-\frac{2\pi m_2}{\|l_2\|}v\right) \cos\left(-\frac{2\pi m_3}{\|l_3\|}w\right) dudvdw + \\ \int_0^{\frac{\|l_1\|}{2}} \int_0^{\frac{\|l_2\|}{2}} \int_0^{\frac{\|l_3\|}{2}} g(x_1, x_2, x_3) \sin\left(\frac{2\pi m_1}{\|l_1\|}x_1\right) \cos\left(\frac{2\pi m_2}{\|l_2\|}x_2\right) \cos\left(\frac{2\pi m_3}{\|l_3\|}x_3\right) dx_1 dx_2 dx_3$$

but since $r = -u\frac{l_1}{\|l_1\|} - v\frac{l_2}{\|l_2\|} - w\frac{l_3}{\|l_3\|}$ represents the separation vector between two ions and g depends only on their distance, meaning it only depends on $\|r\|$, we get the same value for $-r = u\frac{l_1}{\|l_1\|} + v\frac{l_2}{\|l_2\|} + w\frac{l_3}{\|l_3\|}$ and

$$b_m = \int_0^{\frac{\|l_1\|}{2}} \int_0^{\frac{\|l_2\|}{2}} \int_0^{\frac{\|l_3\|}{2}} g(u, v, w) \left[-\sin\left(\frac{2\pi m_1}{\|l_1\|}u\right)\right] \cos\left(-\frac{2\pi m_2}{\|l_2\|}v\right) \cos\left(-\frac{2\pi m_3}{\|l_3\|}w\right) dudvdw + \\ \int_0^{\frac{\|l_1\|}{2}} \int_0^{\frac{\|l_2\|}{2}} \int_0^{\frac{\|l_3\|}{2}} g(x_1, x_2, x_3) \sin\left(\frac{2\pi m_1}{\|l_1\|}x_1\right) \cos\left(\frac{2\pi m_2}{\|l_2\|}x_2\right) \cos\left(\frac{2\pi m_3}{\|l_3\|}x_3\right) dx_1 dx_2 dx_3 \\ = - \int_0^{\frac{\|l_1\|}{2}} \int_0^{\frac{\|l_2\|}{2}} \int_0^{\frac{\|l_3\|}{2}} g(u, v, w) \sin\left(\frac{2\pi m_1}{\|l_1\|}u\right) \cos\left(-\frac{2\pi m_2}{\|l_2\|}v\right) \cos\left(-\frac{2\pi m_3}{\|l_3\|}w\right) dudvdw + \\ \int_0^{\frac{\|l_1\|}{2}} \int_0^{\frac{\|l_2\|}{2}} \int_0^{\frac{\|l_3\|}{2}} g(x_1, x_2, x_3) \sin\left(\frac{2\pi m_1}{\|l_1\|}x_1\right) \cos\left(\frac{2\pi m_2}{\|l_2\|}x_2\right) \cos\left(\frac{2\pi m_3}{\|l_3\|}x_3\right) dx_1 dx_2 dx_3 \\ = 0$$

Ultimately, we get that $ib_m = ic_m = i\alpha_m = i\delta_m = 0$ and that Equation (44) becomes

$$g(x_1, x_2, x_3) = \sum_{m_1=0}^{\infty} \sum_{m_2=0}^{\infty} \sum_{m_3=0}^{\infty} [a_m \cos(u_1 x_1) \cos(u_2 x_2) \cos(u_3 x_3) + \\ d_m \sin(u_1 x_1) \sin(u_2 x_2) \cos(u_3 x_3) + \beta_m \sin(u_1 x_1) \cos(u_2 x_2) \sin(u_3 x_3) + \\ \gamma_m \cos(u_1 x_1) \sin(u_2 x_2) \sin(u_3 x_3)]$$

which can be transformed into a series of cosine terms using trigonometric identities

$$g(x_1, x_2, x_3) = \sum_{m_1=0}^{\infty} \sum_{m_2=0}^{\infty} \sum_{m_3=0}^{\infty} \{a_m [\cos(u_1 x_1 + u_2 x_2 + u_3 x_3) + \cos(u_1 x_1 + u_2 x_2 - u_3 x_3) + \\ \cos(u_1 x_1 - u_2 x_2 + u_3 x_3) + \cos(u_1 x_1 - u_2 x_2 - u_3 x_3)] + \\ d_m [-\cos(u_1 x_1 + u_2 x_2 + u_3 x_3) - \cos(u_1 x_1 + u_2 x_2 - u_3 x_3) + \\ \cos(u_1 x_1 - u_2 x_2 + u_3 x_3) + \cos(u_1 x_1 - u_2 x_2 - u_3 x_3)] + \\ \beta_m [-\cos(u_1 x_1 + u_2 x_2 + u_3 x_3) + \cos(u_1 x_1 + u_2 x_2 - u_3 x_3) \\ - \cos(u_1 x_1 - u_2 x_2 + u_3 x_3) + \cos(u_1 x_1 - u_2 x_2 - u_3 x_3)] + \\ \gamma_m [-\cos(u_1 x_1 + u_2 x_2 + u_3 x_3) + \cos(u_1 x_1 + u_2 x_2 - u_3 x_3) + \\ \cos(u_1 x_1 - u_2 x_2 + u_3 x_3) - \cos(u_1 x_1 - u_2 x_2 - u_3 x_3)]\} \quad (47)$$

and, finally, because of Equations 40,45,46,41,47

$$f(r) = \frac{4\pi}{V\|G_m\|^2} \sum_{G_m \neq 0} \exp\left(-\frac{\|G_m\|^2}{4\alpha^2}\right) \cos(G_m r) \quad (48)$$

□

Proof of Proposition 5 (See page 6)

Proposition 5. *The convergent form of its Coulomb energy potential is formed by the following equations:*

$$\begin{aligned}\Phi_{Coul}^S(r, L) &= k_e \sum_{i,j}^{N'} \sum_n q_i q_j \frac{\text{erfc}(\alpha \|r_{i,j,n}\|)}{2 \|r_{i,j,n}\|} \\ \Phi_{Coul}^L(r, L) &= k_e \sum_{i,j}^N \sum_{m \neq 0} q_i q_j \frac{2\pi \cdot \exp\left(-\frac{G_m^2}{4\alpha^2}\right) \cdot \cos(G_m \cdot r_{i,j})}{VG_m^2} \\ \Phi_{Coul}^{self}(r, L) &= -k_e \sum_{i=1}^N q_i^2 \frac{\alpha}{\sqrt{\pi}}\end{aligned}\tag{8}$$

so that

$$\Phi_{Coul} = \Phi_{Coul}^S + \Phi_{Coul}^L + \Phi_{Coul}^{self}\tag{9}$$

Proof. The proof of this Theorem follows from Proposition 1, Lemma 4 and the addition of one last summation term. Since we have added pair interactions to the summation of Equation (28) so that

$$\Phi_{Coul}^L(R, L) = \frac{k_e}{2} \sum_n \sum_{i=1}^N \sum_{j=1}^N \phi_j^L(r_i + L_n)$$

a self term Φ_{Coul}^{self} is subtracted from the final result and becomes the third summand of the energy potential in Ewald form. With the help of the formula in Equation (36) and the limit when r_i approaches r_j $\lim_{z \rightarrow 0} \text{erf}(z) = \frac{2}{\sqrt{\pi}}z$, we have the direct evaluation of Φ_{Coul}^{self} in real space

$$\Phi_{Coul}^{self} = k_e \frac{\alpha}{\sqrt{\pi}} \sum_{i=1}^N q_i^2\tag{49}$$

□

A.2 Proofs for the InflatedCellTruncation1 algorithm

Proof of Theorem 1 (See page 7)

Theorem 1. *Let \mathcal{C}_n be the parallelepiped of a unit cell and A a face of \mathcal{C}_n with v the height that corresponds to A . The vector t that translates the plane P of \mathcal{C}_n to a parallel plane P' tangent to (O, r_{off}) has length $\|t\| = r_{off} - \frac{v}{2}$ and is parallel to the normal $N_{P'}$ of plane P' .*

Proof. Let t be the vector that translates P to P' . We want P and P' to be parallel, so their distance is defined by t and, as a result, t is perpendicular to both P and P' , or, in other words,

$$t \parallel \vec{N}_{P'}\tag{50}$$

where $\vec{N}_{P'}$ is the normal vector of plane P' . We want P' tangent to sphere (O, r_{off}) and let p be the point of P' that touches (O, r_{off}) . The distance between the centre O and P' is given by the length of vector \vec{Op} , which is perpendicular to P' . Then

$$\vec{Op} \parallel \vec{N}_{P'}\tag{51}$$

$$\|\vec{Op}\| = r_{off}\tag{52}$$

Ultimately, from 50, 51

$$t \parallel \vec{Op} \parallel v\tag{53}$$

where v is the vector of height of \mathcal{C}_n that is perpendicular to P . It follows that, since O is the centre of gravity of the unit cell,

$$\vec{Op} = t - \frac{v}{2} \Rightarrow \|\vec{Op}\|v = \|t\|v - \frac{\|v\|}{2}v \Rightarrow r_{off} = \|t\| + \frac{\|v\|}{2}\tag{54}$$

where v is a unit vector.

□

Proof of Corollary 1 (See page 7)

Corollary 1. *The distance between P and P' can fit $\frac{\|t\|}{\|v\|} + 1/2$ many unit cell images.*

Proof. Let $\mathcal{C}_{(0,0,0)}$ be the central unit cell with lattice vectors l_1, l_2, l_3 and $\mathcal{C}_{a_1}, \mathcal{C}_{a_2}, \dots, \mathcal{C}_{a_m}$, $a_i \in \mathbb{N}^3$, $i \in [m]$ images of the unit cell surrounding $\mathcal{C}_{(0,0,0)}$. Let also ϵ_1 be a line parallel to l_1 that goes through the centre of gravity O of $\mathcal{C}_{(0,0,0)}$. Line ϵ_1 cuts the faces of $\mathcal{C}_{(0,0,0)}, \mathcal{C}_{a_1}, \mathcal{C}_{a_2}, \dots, \mathcal{C}_{a_m}$ at points p_0, p_1, \dots, p_m . Let ϵ_2 be the line in the direction of t as defined in Theorem 1 that goes through O of $\mathcal{C}_{(0,0,0)}$ and cuts adjacent images of the unit cell at points p'_0, p'_1, \dots, p'_k . Since the faces of the images of the unit cells cut by ϵ_1, ϵ_2 are parallel, we have from Thales' theorem that $m = k$ and $Op_0 : p_0p_1 : p_1p_2 : \dots : p_{m-1}p_m = Op'_0 : p'_0p'_1 : p'_1p'_2 : \dots : p'_{m-1}p'_m$. However, since we deal with images of the unit cell and ϵ_1 is parallel to l_1 , we have that

$$\frac{Op_0}{p_0p_1} = \frac{Op'_0}{p'_0p'_1} \quad (55)$$

and

$$\frac{p_{i-1}p_i}{p_i p_{i+1}} = 1 = \frac{p'_{i-1}p'_i}{p'_i p'_{i+1}}, \quad \forall i \in 1, \dots, m-1 \quad (56)$$

We know that, because O is the center of gravity

$$\frac{Op_0}{p_0p_1} = \frac{Op'_0}{p'_0p'_1} \Leftrightarrow \frac{\|l_1\|/2}{\|l_1\|} = \frac{\|v\|/2}{p'_0p'_1} \Leftrightarrow p'_0p'_1 = \|v\| \quad (57)$$

From 55 and 57 and Theorem 1 we conclude that we can fit $(\|t\| + \frac{\|v\|}{2})/\|v\| = \frac{\|t\|}{\|v\|} + 1/2$ many images between P and P' . \square

A.3 Proofs related to potential forces – differentiation

Proof of Proposition 7, the Coulomb first derivatives w.r.t. ion positions (See page 9)

Proposition 7. *The internal electrostatic forces of $(\mathcal{C}_n : L_n, R)$ can be written as:*

$$\begin{aligned} \mathcal{F}_{Coul} &= -\nabla_r \Phi_{Coul} \\ &= -\left(\frac{\partial \Phi_{Coul}}{\partial r_1}, \frac{\partial \Phi_{Coul}}{\partial r_2}, \dots, \frac{\partial \Phi_{Coul}}{\partial r_N}\right) \end{aligned} \quad (15)$$

where

$$\begin{aligned} \frac{\partial \Phi_{Coul}}{\partial r_t} &= \frac{k_e}{2} \sum_n \left[-\sum_{j=1}^{N'} q_t q_j \left(\frac{2\alpha}{\sqrt{\pi}} \exp(-\alpha^2 \|r_{t,j,n}\|^2) + \frac{\text{erfc}(\alpha r_{t,j,n})}{\|r_{t,j,n}\|} \right) \frac{r_{t,j,n}}{\|r_{t,j,n}\|^2} + \right. \\ &\quad \left. \sum_{i=1}^{N'} q_i q_t \left(\frac{2\alpha}{\sqrt{\pi}} \exp(-\alpha^2 \|r_{i,t,n}\|^2) + \frac{\text{erfc}(\alpha r_{i,t,n})}{\|r_{i,t,n}\|} \right) \frac{r_{i,t,n}}{\|r_{i,t,n}\|^2} \right] + \\ &\quad \frac{k_e}{2} \sum_{G_m \neq 0} \frac{2\pi k_e}{V \|G_m\|^2} \exp\left(-\frac{\|G_m\|^2}{4\alpha^2}\right) \left[-\sum_{j=1}^N q_t q_j \sin(G_m r_{t,j}) + \sum_{i=1}^N q_i q_t \sin(G_m r_{i,t}) \right] G_m, \quad t \in [N] \end{aligned} \quad (16)$$

Proof. Let $r_{i,j,n} = r_i + L_n - r_j$ be the separation vector in 3-dimensional space between a pair of ions i, j . The distance $\|r_{i,j,n}\|$ is a multivariate function $\mathbb{R}^3 \rightarrow \mathbb{R}$. Let us define the two following functions that take a vector $r_t = (r_{tx}, r_{ty}, r_{tz})$ as the free variable:

$$d_j(r_t) = \|r_t + L_n - r_j\|, \quad d_j : \mathbb{R}^3 \rightarrow \mathbb{R}$$

If we take the gradient of d with respect to the components of r_t , we have

$$\begin{aligned}
\nabla d_j(r_t) &= \left(\frac{\partial d_j}{\partial r_{tx}}, \frac{\partial d_j}{\partial r_{ty}}, \frac{\partial d_j}{\partial r_{tz}} \right)(r_t) \\
&= \left(\frac{r_{tx} + n_1 l_{1x} + n_2 l_{2x} + n_3 l_{3x} - r_{jx}}{\|r_t + L_n - r_j\|} \cdot \frac{\partial}{\partial r_{tx}}(r_{tx}\hat{x} + r_{ty}\hat{y} + r_{tz}\hat{z}), \right. \\
&\quad \frac{r_{ty} + n_1 l_{1y} + n_2 l_{2y} + n_3 l_{3y} - r_{jy}}{\|r_t + L_n - r_j\|} \cdot \frac{\partial}{\partial r_{ty}}(r_{tx}\hat{x} + r_{ty}\hat{y} + r_{tz}\hat{z}), \\
&\quad \left. \frac{r_{tz} + n_1 l_{1z} + n_2 l_{2z} + n_3 l_{3z} - r_{jz}}{\|r_t + L_n - r_j\|} \cdot \frac{\partial}{\partial r_{tz}}(r_{tx}\hat{x} + r_{ty}\hat{y} + r_{tz}\hat{z}) \right) \\
&= \frac{r_{t,j,n}}{\|r_{t,j,n}\|}
\end{aligned}$$

in which $\hat{x}, \hat{y}, \hat{z}$ are the Cartesian unit vectors. Accordingly, we have

$$d^i(r_t) = \|r_i + L_n - r_t\|, \quad d^i : \mathbb{R}^3 \rightarrow \mathbb{R}$$

with gradient

$$\begin{aligned}
\nabla d^i(r_t) &= \left(\frac{\partial d^i}{\partial r_{tx}}, \frac{\partial d^i}{\partial r_{ty}}, \frac{\partial d^i}{\partial r_{tz}} \right)(r_t) \\
&= \left(\frac{r_{ix} + n_1 l_{1x} + n_2 l_{2x} + n_3 l_{3x} - r_{tx}}{\|r_i + L_n - r_t\|} \cdot \frac{\partial}{\partial r_{tx}}(-r_{tx}\hat{x} - r_{ty}\hat{y} - r_{tz}\hat{z}), \right. \\
&\quad \frac{r_{iy} + n_1 l_{1y} + n_2 l_{2y} + n_3 l_{3y} - r_{ty}}{\|r_i + L_n - r_j\|} \cdot \frac{\partial}{\partial r_{ty}}(-r_{tx}\hat{x} - r_{ty}\hat{y} - r_{tz}\hat{z}), \\
&\quad \left. \frac{r_{iz} + n_1 l_{1z} + n_2 l_{2z} + n_3 l_{3z} - r_{tz}}{\|r_i + L_n - r_t\|} \cdot \frac{\partial}{\partial r_{tz}}(-r_{tx}\hat{x} - r_{ty}\hat{y} - r_{tz}\hat{z}) \right) \\
&= -\frac{r_{i,t,n}}{\|r_{i,j,n}\|}
\end{aligned}$$

Let us define $f_S(x) = \frac{k_e \operatorname{erfc}(\alpha x)}{2x}$, $f_S : \mathbb{R} \rightarrow \mathbb{R}$ and d_j, d^i as before. Then we have:

$$f'_S = -\frac{k_e}{2} \left(\frac{2\alpha}{\sqrt{\pi}} \exp(-\alpha^2 x^2) + \frac{\operatorname{erfc}(\alpha x)}{x} \right) \frac{1}{x} \quad (58)$$

so that

$$\Phi_{Coul}^S(R, L) = \sum_{i,j} \sum_n^{N'} q_i q_j f_S(\|r_{i,j,n}\|) \quad (59)$$

and then the forces are given by

$$\begin{aligned}
\mathcal{F}_{Coul}^S &= -\nabla_r \Phi_{Coul}^S(R, L) = -\left(\frac{\partial \Phi_{Coul}^S}{\partial r_1}, \frac{\partial \Phi_{Coul}^S}{\partial r_2}, \dots, \frac{\partial \Phi_{Coul}^S}{\partial r_N} \right), \\
\frac{\partial \Phi_{Coul}^S}{\partial r_t} &= \sum_{j=1}^{N'} \sum_n q_t q_j f'_S(r_{t,j,n}) \nabla d_j(r_t) + \sum_{i=1}^{N'} \sum_n q_i q_t f'_S(r_{i,t,n}) \nabla d^i(r_t), \quad t \in [N]
\end{aligned} \quad (60)$$

Similarly, let $f_L(x) = \sum_{G_m \neq 0} \frac{2\pi k_e}{V \|G_m\|^2} \exp\left(-\frac{\|G_m\|^2}{4\alpha^2}\right) \cos(G_m x)$, $f_L : \mathbb{R}^3 \rightarrow \mathbb{R}$ and

$$\nabla_x f_L = -\sum_{G_m \neq 0} \frac{2\pi k_e}{V \|G_m\|^2} \exp\left(-\frac{\|G_m\|^2}{4\alpha^2}\right) G_m \sin(G_m x) \quad (61)$$

Using f_L we get

$$\Phi_{Coul}^L(R, L) = \sum_{i,j}^N q_i q_j f_L(r_{i,j})$$

and

$$\begin{aligned}\mathcal{F}_{Coul}^L &= -\nabla_r \Phi_{Coul}^L(R, L) = -\left(\frac{\partial \Phi_{Coul}^L}{\partial r_1}, \frac{\partial \Phi_{Coul}^L}{\partial r_2}, \dots, \frac{\partial \Phi_{Coul}^L}{\partial r_N}\right), \\ \frac{\partial \Phi_{Coul}^L}{\partial r_t} &= \sum_{j=1}^N q_t q_j \nabla_r f_L(r_{t,j}) - \sum_{i=1}^N q_i q_t \nabla_r f_L(r_{i,t}), \quad t \in [N]\end{aligned}\quad (62)$$

where $r_{t,j} = r_t - r_j$ and vice versa. Ultimately

$$-\nabla_r \Phi_{Coul} = \mathcal{F}_{Coul} = \mathcal{F}_{Coul}^S + \mathcal{F}_{Coul}^L \quad (63)$$

□

Proof of Proposition 8, the Buckingham first derivatives w.r.t. ion positions (See page 10)

Proposition 8. *The internal Buckingham forces of $(C_n : L_n, R)$ can be written as:*

$$\begin{aligned}\mathcal{F}_{Buck} &= -\nabla_r \Phi_{Buck} \\ &= -\left(\frac{\partial \Phi_{Buck}}{\partial r_1}, \frac{\partial \Phi_{Buck}}{\partial r_2}, \dots, \frac{\partial \Phi_{Buck}}{\partial r_N}\right)\end{aligned}\quad (17)$$

where

$$\begin{aligned}\frac{\partial \Phi_{Buck}}{\partial r_t} &= \sum_n \left\{ \sum_{j=1}^{N'} \left[-\frac{A_{tj}}{\rho} \exp\left(-\frac{\|r_{t,j,n}\|}{\rho}\right) - C_{tj} \frac{\exp(-\alpha^2 \|r_{t,j,n}\|^2)}{\|r_{t,j,n}\|^5} \left(\frac{6}{\|r_{t,j,n}\|^2} + 6\alpha^2 + \alpha^6 r_{t,j,n}^4 + 3\alpha^4 \|r_{t,j,n}\|^2 \right) \right] + \right. \\ &\quad \left. \sum_{i=1}^{N'} \left[\frac{A_{it}}{\rho} \exp\left(-\frac{\|r_{i,t,n}\|}{\rho}\right) + C_{it} \frac{\exp(-\alpha^2 \|r_{i,t,n}\|^2)}{\|r_{i,t,n}\|^5} \left(\frac{6}{\|r_{i,t,n}\|^2} + 6\alpha^2 + \alpha^6 \|r_{i,t,n}\|^4 + 3\alpha^4 \|r_{i,t,n}\|^2 \right) \right] \right\} \frac{r_{i,t,n}}{\|r_{i,t,n}\|} - \\ &\quad \frac{\pi^{3/2}}{12V} \sum_{G_m \neq 0} \left\{ \sum_{j=1}^{N'} C_{tj} \left[\sqrt{\pi} \cdot \operatorname{erfc}\left(\frac{G_m}{2\alpha}\right) + \left(\frac{4\alpha^3}{k^3} - \frac{2\alpha}{G_m}\right) \exp\left(-\frac{G_m^2}{4\alpha^2}\right) \right] \cdot \sin(G_m r_{t,j,n}) + \right. \\ &\quad \left. \sum_{i=1}^{N'} C_{it} \left[\sqrt{\pi} \cdot \operatorname{erfc}\left(\frac{G_m}{2\alpha}\right) + \left(\frac{4\alpha^3}{k^3} - \frac{2\alpha}{G_m}\right) \exp\left(-\frac{G_m^2}{4\alpha^2}\right) \right] \cdot \sin(G_m r_{i,t,n}) \right\} G_m, \quad t \in [N]\end{aligned}\quad (18)$$

Proof. Let $g_{S1}(x) = \exp(-\frac{x}{\rho})$ and $g_{S2}(x) = -\frac{1}{x^6} \left(1 + \alpha^2 x^2 + \frac{\alpha^4 x^4}{2}\right) \exp(-\alpha^2 x^2)$, $g_S : \mathbb{R} \rightarrow \mathbb{R}$, $x = \|x\|$ so that

$$g'_{S1}(x) = -\frac{1}{\rho} \exp\left(-\frac{x}{\rho}\right), \quad g'_{S2}(x) = \frac{\exp(-\alpha^2 x^2)}{x^5} \left(\frac{6}{x^2} + 6\alpha^2 + \alpha^6 x^4 + 3\alpha^4 x^2\right) \quad (64)$$

then

$$\begin{aligned}\mathcal{F}_{Buck}^S &= -\nabla_r \Phi_{Buck}^S(R, L) = -\left(\frac{\partial \Phi_{Buck}^S}{\partial r_1}, \frac{\partial \Phi_{Buck}^S}{\partial r_2}, \dots, \frac{\partial \Phi_{Buck}^S}{\partial r_N}\right), \\ \frac{\partial \Phi_{Buck}^S}{\partial r_t} &= \sum_{j=1}^{N'} \sum_n [A_{tj} g'_{S1}(r_{t,j,n}) - C_{tj} g'_{S2}(r_{t,j,n})] \nabla d_j(r_t) + \\ &\quad \sum_{i=1}^{N'} \sum_n [A_{it} \nabla_r g_{S1}(r_{i,t,n}) - C_{it} \nabla_r g_{S2}(r_{i,t,n})] \nabla d^i(r_t), \quad t \in [N]\end{aligned}\quad (65)$$

and in the same fashion $g_L(x) = \frac{\pi^{3/2}}{12V} \sum_n \left[\sqrt{\pi} \cdot \operatorname{erfc}\left(\frac{G_m}{2\alpha}\right) + \left(\frac{4\alpha^3}{G_m^3} - \frac{2\alpha}{G_m}\right) \exp\left(-\frac{G_m^2}{4\alpha^2}\right) \right] \cdot \cos(G_m x) G_m^3$

$$\nabla_x g_L = -\frac{\pi^{3/2}}{12V} \sum_n \left[\sqrt{\pi} \cdot \operatorname{erfc}\left(\frac{G_m}{2\alpha}\right) + \left(\frac{4\alpha^3}{k^3} - \frac{2\alpha}{G_m}\right) \exp\left(-\frac{G_m^2}{4\alpha^2}\right) \right] \cdot G_m \sin(G_m x) \quad (66)$$

then

$$\begin{aligned}\mathcal{F}_{Buck}^L &= -\nabla_r \Phi_{Buck}^L(R, L) = -\left(\frac{\partial \Phi_{Buck}^L}{\partial r_1}, \frac{\partial \Phi_{Buck}^L}{\partial r_2}, \dots, \frac{\partial \Phi_{Buck}^L}{\partial r_N}\right), \\ \frac{\partial \Phi_{Buck}^L}{\partial r_t} &= \sum_{j=1}^{N'} C_{tj} \nabla_r g_L(r_{t,j}) - \sum_{i=1}^{N'} C_{it} \nabla_r g_L(r_{i,t}), \quad t \in [N]\end{aligned}\quad (67)$$

Thus

$$-\nabla_r \Phi_{Buck} = \mathcal{F}_{Buck} = \mathcal{F}_{Buck}^S + \mathcal{F}_{Buck}^L \quad (68)$$

□

Proof of Proposition 9, stress and strain (See page 11)

Proposition 9. *The forces that act on the volume of a unit cell \mathcal{C}_n and change the shape of the crystal lattice can be expressed with the symmetric stress tensor $\sigma = \{\sigma_{\lambda\mu}\}_{\lambda,\mu \in [3]}$ as a result of an existing strain $\epsilon = \{\epsilon_{\lambda\mu}\}_{\lambda,\mu \in [3]}$.*

Proof. Let us assume that at the start of the relaxation, the strain is zero. If we form a matrix $L_0 \in \mathbb{R}^{3 \times 3}$ using the lattice vectors L in the initial state, the transformation of the vectors with strains would be

$$L_1 = (I + \epsilon_1)^T L_0, \quad L, \epsilon_1 \in \mathbb{R}^{3 \times 3} \quad (69)$$

where $I \in \mathbb{R}^{3 \times 3}$ stands for the identity matrix. By continuously updating the lattice vectors' matrix as in Equation (69), we can retrieve a sequence $L_0, L_1, L_2, \dots, L_n$ such that L_n represents the lattice in equilibrium. This fractional change is called strain and involves two kinds of deformation; the normal strain ($\epsilon_{xx}, \epsilon_{yy}, \epsilon_{zz} \in \mathbb{R}$), that expresses changes to the length of the lattice vectors and shear strain ($\epsilon_{xy}, \epsilon_{yz}, \epsilon_{zx} \in \mathbb{R}$), which is the tangent of the angular change between two axes. We will now proceed to present the origins and physical interpretation of strain.

The deformation of the lattice represents motion of lattice points relative to each other. It is a linear transformation [38] of the lattice points and can be described by a displacement vector

$$u = u_x \cdot \hat{x} + u_y \cdot \hat{y} + u_z \cdot \hat{z}, \quad u \in \mathbb{R}^3, \quad u_x, u_y, u_z \in \mathbb{R} \quad (70)$$

where the components u_x, u_y, u_z of vector u are in reality continuous scalar functions of time $t \in \mathbb{R}^+$ and the position vector $x \in \mathbb{R}^3$ of a point, so that $u_x = u_x(x, t) : \mathbb{R}^2 \rightarrow \mathbb{R}$.

By exploiting the partial derivatives of the displacement functions u with respect to the position's x each component, we can derive the fractional change per direction along the Cartesian coordinate axes as follows

$$\epsilon_{xx} = \frac{\partial u_x}{\partial x_x}, \quad \epsilon_{yy} = \frac{\partial u_y}{\partial x_y}, \quad \epsilon_{zz} = \frac{\partial u_z}{\partial x_z} \quad (71)$$

$$\epsilon_{xy} = \frac{1}{2} \left(\frac{\partial u_y}{\partial x_x} + \frac{\partial u_x}{\partial x_y} \right) = \epsilon_{yx}, \quad \epsilon_{yz} = \frac{1}{2} \left(\frac{\partial u_z}{\partial x_y} + \frac{\partial u_y}{\partial x_z} \right) = \epsilon_{zy}, \quad \epsilon_{zx} = \frac{1}{2} \left(\frac{\partial u_z}{\partial x_x} + \frac{\partial u_x}{\partial x_z} \right) = \epsilon_{xz} \quad (72)$$

Then, the second rank symmetrical tensor of strain at iteration i is

$$\epsilon_i = \begin{bmatrix} \epsilon_{xxi} & \epsilon_{xyi} & \epsilon_{xzi} \\ \epsilon_{xyi} & \epsilon_{yyi} & \epsilon_{yzi} \\ \epsilon_{xzi} & \epsilon_{yzi} & \epsilon_{zzi} \end{bmatrix} \quad (73)$$

Since the strains are used as the external coordinates of the unit cell and are directly related to the lattice vectors, we can differentiate the energy function Φ with respect to the strains. Under symmetrical, infinitesimal strain ϵ , the derivative of the energy potential function with respect to strains expresses stress σ

$$\sigma_{\alpha\beta} = \frac{1}{V} \frac{\partial \Phi}{\partial \epsilon_{\alpha\beta}}, \quad \forall \alpha, \beta \in \{x, y, z\}$$

whereby very small, compared to the dimensions of the unit cell with volume V , changes to strain are measured. Stress is a symmetrical tensor comprising the components $\sigma_{\alpha\beta} \in \mathbb{R}$, $\forall \alpha, \beta \in \{x, y, z\}$ which are divided into normal and shear stresses as in the case of strains. Next, we will explain the tensor's physical interpretation that also accounts for its symmetry and properties.

Let us consider point $O \in \mathbb{R}^3$ in the interior of the crystal. When the lattice is deformed, forces start to act along the volume of the crystal per unit area, such that, internal forces are transmitted across a plane that passes through O and separates the crystal into two halves. The cohesive forces crossing the plane with normal $n \in \mathbb{R}^3$ can be described by a force vector $f \in \mathbb{R}^3$ acting at point O , which belongs to a small area $A \in \mathbb{R}$ of the plane, as follows

$$T^{(n)} = \lim_{\Delta A \rightarrow 0} \frac{f}{\Delta A}, \quad T^{(n)} \in \mathbb{R}^3, \quad f = (f_x, f_y, f_z) \in \mathbb{R}^3 \quad (74)$$

called stress vector. The stress vector has an arbitrary direction compared to the normal vector n . In order to be able to better investigate the phenomenon, we assume that the stress vector is

acting on planes whose normal vectors are parallel to the Cartesian coordinate axes. After such an assumption, we can analyse the force vector F into three components, one normal to each plane and two components parallel to the plane. For example, if we declare ΔA the piece of surface with normal vector n oriented parallel to the x Cartesian coordinate axis and passing through O , then we can express f as $f = f_x \cdot \hat{x} + f_y \cdot \hat{y} + f_z \cdot \hat{z}$, where $\hat{x}, \hat{y}, \hat{z}$ the unit vectors parallel to the Cartesian coordinate axes. The limits with respect to the confinement of ΔA express the average force exerted on the point O of the face with area ΔA and normal vector parallel to the x axis. These are the components of the stress vector $\overset{(n)}{T}$ acting on the corresponding plane. It becomes apparent that each stress component is associated with two directions, the direction of n and the direction of the component of f , and are respectively referred to by two subscripts. Hence, for a face with area ΔA and normal vector parallel to x axis the stress components are

$$\begin{aligned}\sigma_{xx} &= \lim_{\Delta A \rightarrow 0} \frac{f_x}{\Delta A} \\ \sigma_{xy} &= \lim_{\Delta A \rightarrow 0} \frac{f_y}{\Delta A} \\ \sigma_{xz} &= \lim_{\Delta A \rightarrow 0} \frac{f_z}{\Delta A}\end{aligned}$$

Consequently, by considering each plane whose normal vector direction is parallel to the Cartesian axes and passes through point O , we get three faces $\Delta A_x, \Delta A_y, \Delta A_z$ and nine stress components

$$\begin{aligned}\sigma_{xx} &= \lim_{\Delta A_x \rightarrow 0} \frac{f_x}{\Delta A_x} & \sigma_{xy} &= \lim_{\Delta A_x \rightarrow 0} \frac{f_y}{\Delta A_x} & \sigma_{xz} &= \lim_{\Delta A_x \rightarrow 0} \frac{f_z}{\Delta A_x} \\ \sigma_{yx} &= \lim_{\Delta A_y \rightarrow 0} \frac{f_x}{\Delta A_y} & \sigma_{yy} &= \lim_{\Delta A_y \rightarrow 0} \frac{f_y}{\Delta A_y} & \sigma_{yz} &= \lim_{\Delta A_y \rightarrow 0} \frac{f_z}{\Delta A_y} \\ \sigma_{zx} &= \lim_{\Delta A_z \rightarrow 0} \frac{f_x}{\Delta A_z} & \sigma_{zy} &= \lim_{\Delta A_z \rightarrow 0} \frac{f_y}{\Delta A_z} & \sigma_{zz} &= \lim_{\Delta A_z \rightarrow 0} \frac{f_z}{\Delta A_z}\end{aligned}$$

The stress components whose direction is parallel to the planes are called shear stresses, and the components normal to the planes are called normal stresses. We can express all of the stress components as in

$$\sigma_{\lambda\mu} = \lim_{\Delta A_\lambda \rightarrow 0} \frac{f_\mu}{\Delta A_\lambda}, \quad \lambda, \mu \in \{x, y, z\} \quad (75)$$

Furthermore, we impose equilibrium conditions such that the unit cell does not perform rigid-body movements and rotations. As explained in [11], this results in the shear stresses to be equal $\sigma_{\lambda\mu} = \sigma_{\mu\lambda}$, $\lambda \neq \mu$. Similarly to the case of strains, the stresses are represented by a second rank symmetrical tensor

$$\sigma = \begin{bmatrix} \sigma_{xx} & \sigma_{xy} & \sigma_{xz} \\ \sigma_{yx} & \sigma_{yy} & \sigma_{yz} \\ \sigma_{zx} & \sigma_{zy} & \sigma_{zz} \end{bmatrix}, \quad \sigma_{\lambda\mu} \in \mathbb{R} \quad \forall \lambda, \mu \in \{x, y, z\}$$

which, because of the equal components, it comes to six independent components

$$\sigma = \begin{pmatrix} \sigma_{xx} \\ \sigma_{yy} \\ \sigma_{zz} \\ \sigma_{yz} \\ \sigma_{xz} \\ \sigma_{xy} \end{pmatrix}, \quad \sigma_{\lambda\mu} \in \mathbb{R} \quad \forall \lambda, \mu \in \{x, y, z\} \quad (76)$$

which are used to update strain tensor ϵ_i as in Equation (71)

$$\epsilon_{i+1} = \begin{bmatrix} 1 + (\epsilon_{xxi} + a\sigma_{xxi}) & \frac{1}{2}(\epsilon_{xyi} + a\sigma_{xyi}) & \frac{1}{2}(\epsilon_{xzi} + a\sigma_{xzi}) \\ \frac{1}{2}(\epsilon_{xyi} + a\sigma_{xyi}) & 1 + (\epsilon_{yyi} + a\sigma_{yyi}) & \frac{1}{2}(\epsilon_{yzi} + a\sigma_{yzi}) \\ \frac{1}{2}(\epsilon_{xzi} + a\sigma_{xzi}) & \frac{1}{2}(\epsilon_{yzi} + a\sigma_{yzi}) & 1 + (\epsilon_{yzi} + a\sigma_{yzi}) \end{bmatrix}, \quad a \in \mathbb{R} \quad (77)$$

□

Proof of Lemma 5.2, the derivatives w.r.t. lattice strain (See page 11)

The parameters affected by stress are R, L_n, G_m , hence each stress component $\sigma_{\lambda\mu}$ is calculated as

$$\sigma_{\lambda\mu} = \frac{1}{V} \left(\sum_n \sum_{i=1}^N \frac{\partial \Phi}{\partial r_{i\lambda}} r_{i\mu} + \sum_n \frac{\partial \Phi}{\partial L_{n\lambda}} L_{n\mu} + \sum_m \frac{\partial \Phi}{\partial G_{m\mu}} G_{m\lambda} + \frac{\partial \Phi}{\partial V} \delta_{\lambda\mu} V \right) \quad (20)$$

Proof. Because of the chain rule, we can obtain each stress component as a sum of the derivatives of Φ with respect to every parameter, multiplied by the derivatives of the parameters with respect to strains. More precisely

$$\begin{aligned} \frac{\partial r_{t\psi}}{\partial \epsilon_{\lambda\mu}} &= \delta_{\psi\lambda} r_{t\mu}, & \frac{\partial l_{t\psi}}{\partial \epsilon_{\lambda\mu}} &= \delta_{\psi\lambda} l_{t\mu}, & \frac{\partial k_{t\psi}}{\partial \epsilon_{\lambda\mu}} &= -\delta_{\psi\mu} k_{t\lambda} \\ \frac{\partial L_{n\psi}}{\partial \epsilon_{\lambda\mu}} &= \delta_{\psi\lambda} L_{n\mu}, & \frac{\partial G_{m\psi}}{\partial \epsilon_{\lambda\mu}} &= -\delta_{\psi\mu} G_{m\lambda}, & \frac{\partial V}{\partial \epsilon_{\lambda\mu}} &= \delta_{\lambda\mu} V \end{aligned} \quad (78)$$

In the above latin letters as subscripts denote a part of the corresponding vector's name, e.g. for r_1 we have $t = 1$, and ψ, λ, μ refer to the Cartesian coordinates of the vector with subscript t , or to the components of the strain tensor ϵ ; δ is the Kronecker delta. We note that, while the component λ of the real cell lattice vector $l_t(0)$ after distortion $l_t(\epsilon)$ becomes

$$l_{t\lambda}(\epsilon) = \sum_{\beta}^3 (\delta_{\lambda\beta} + \epsilon_{\lambda\beta}) l_{t\beta}(0)$$

the components of reciprocal vectors transform in the following way

$$k_{t\lambda}(\epsilon) = \sum_{\beta}^3 (\delta_{\beta\lambda} - \epsilon_{\beta\lambda}) k_{t\beta}(0)$$

It is important here to highlight that, since we are changing the lattice cell parameters, the unit cell volume is also affected. Thus derivatives of the volume must also be defined. What is more, Equation (10) suggests that the α parameter is a function of the volume. We have that

$$\frac{\partial \alpha}{\partial \epsilon_{\lambda\mu}} = \frac{\partial \alpha}{\partial V} \frac{\partial V}{\partial \epsilon_{\lambda\mu}} = a'(V) \delta_{\lambda\mu} V \quad (79)$$

We hereafter refer to $a'(V)$ as a' . □